

EVALUATION OF EFFECT OF FILLET ROLLING PROCESS ON THE FATIGUE
PERFORMANCE OF A DIESEL ENGINE CRANKSHAFT

A THESIS SUBMITTED TO
THE GRADUATE SCHOOL OF NATURAL AND APPLIED SCIENCES
OF
MIDDLE EAST TECHNICAL UNIVERSITY

BY

GÜL ÇEVİK

IN PARTIAL FULFILLMENT OF THE REQUIREMENTS
FOR
THE DEGREE OF DOCTOR OF PHILOSOPHY
IN
METALLURGICAL AND MATERIALS ENGINEERING

SEPTEMBER 2012

Approval of the Thesis:

**EVALUATION OF EFFECT OF FILLET ROLLING PROCESS ON
THE FATIGUE PERFORMANCE OF A DIESEL ENGINE
CRANKSHAFT**

Submitted by **GÜL ÇEVİK** in partial fulfillment of the requirements for the degree of **Doctor of Philosophy in Metallurgical and Materials Engineering, Middle East Technical University** by,

Prof. Dr. Canan Özgen _____
Dean, Graduate School of **Natural and Applied Sciences**

Prof. Dr. Cemil Hakan Gür _____
Head of Department, **Metallurgical and Materials Engineering**

Prof. Dr. Rıza Gürbüz _____
Supervisor, **Metallurgical and Materials Engineering Dept., METU**

Examining Committee Members:

Prof.Dr. Bilgehan Ögel _____
Metallurgical and Materials Engineering Dept., METU

Prof.Dr. Rıza Gürbüz _____
Metallurgical and Materials Engineering Dept., METU

Assist. Prof. Dr. Kazım Tur _____
Metallurgical and Materials Engineering Dept., Atılım University

Prof. Dr. Cemil Hakan Gür _____
Metallurgical and Materials Engineering Dept., METU

Prof. Dr. Ali Kalkanlı _____
Metallurgical and Materials Engineering Dept., METU

Date: 17/09/2012

I hereby declare that all information in this document has been obtained and presented in accordance with academic rules and ethical conduct. I also declare that, as required by these rules and conduct, I have fully cited and referenced all material and results that are not original to this work.

Name, Last name: Gül Çevik

Signature :

ABSTRACT

EVALUATION OF EFFECT OF FILLET ROLLING PROCESS ON THE FATIGUE PERFORMANCE OF A DIESEL ENGINE CRANKSHAFT

Çevik, Gül

Ph.D., Department of Metallurgical and Materials Engineering

Supervisor: Prof. Dr. Rıza Gürbüz

September 2012, 187 Pages

In this study, effect of fillet rolling process on fatigue performance of a diesel engine crankshaft was investigated. Crankshafts from two different materials, were studied; ductile cast iron EN-GJS 800-2 and micro-alloyed steel 38MnVS6. Resonance bending fatigue tests were conducted with crankshaft samples. Test plan according to staircase test methodology was used. Statistical analyses were carried out with the test data by Maximum Likelihood Estimation method in order to calculate the fatigue limits and construct the S-N curves based on Random Fatigue Limit (RFL) and Modified Basquin models. Fatigue limit calculations were also conducted by Dixon-Mood method and by Maximum Likelihood Estimation methodology for Normal and Weibull distributions. Fillet rolling process was simulated by computer based analysis in order to calculate the compressive residual stress profile at the fillet region to shed more light on the mechanisms and effect of fillet rolling. Fatigue performances of crankshafts from two types of materials were evaluated both at unrolled and fillet rolled states. Effect of fillet rolling load on fatigue

performance was also evaluated with steel crankshafts. It was found that ductile cast iron showed better performance under bending fatigue tests than the steel crankshaft both at the fillet rolled and unrolled conditions. On the other hand, fillet rolling process was found to be more effective on steel crankshaft than ductile cast iron crankshaft in terms of fatigue performance improvement. It was also seen that fatigue limit increases with the fillet rolling load up to a limit where surface quality is deteriorated. Residual stress analysis showed that a higher magnitude of residual stress can develop on steel crankshaft fillet region whereas the effective depth of the residual stress is higher on ductile cast iron crankshaft with the same rolling condition. Residual stress analysis of steel crankshafts rolled at different rolling conditions show that, peak residual stress increase with the increasing rolling load is not significantly high and main effect of increased rolling load is the increased effective depth of residual stresses. The MLE methodology used in statistical analysis of the test data was found to be effective for life regression and fatigue strength distributions analysis. RFL model has provided better life regression analysis and fatigue limit calculations than Modified Basquin model. Dixon-Mood method was found to be overestimating the fatigue limit.

Keywords: Fatigue, residual stress, statistical analysis, crankshaft, fillet rolling.

ÖZ

DİZEL MOTOR KRANK MİLLERİNE UYGULANAN EZME İŞLEMİNİN YORULMA PERFORMANSINA ETKİSİNİN İNCELENMESİ

Çevik, Gül

Doktora, Metalurji ve Malzeme Mühendisliği Bölümü

Tez Yöneticisi: Prof. Dr. Rıza Gürbüz

Eylül 2012, 187 Sayfa

Bu çalışmada dizel motor krank millerine uygulanan ezme işleminin yorulma performansına etkisi incelenmiştir. Bu çalışmada sfero dökme demir EN-GJS 800-2 ve mikro alaşımlı çelik 38MnVS6 olmak üzere iki farklı krank mili malzemesi çalışılmıştır. Krank millerinden alınan örneklerle rezonans eğme yorulma testleri yapılmıştır. Test planları basamaklı test metoduna göre oluşturulmuştur. Elde edilen test verileri yorulma mukavemetini hesaplamak ve Gerilim – Döngü sayısı grafikleri çizmek amacıyla Maksimum Olabilirlik Tahmini (MLE) yöntemine dayanan Random Yorulma Limiti ve Modified Basquin modelleri ile istatistik olarak değerlendirilmiştir. Yorulma limiti hesapları Dixon-Mood ve MLE yöntemi ile Normal ve Weibull dağılımlarına göre tekrarlanmıştır. Ezme işlemi mekanizmasına ve etkisine ışık tutması amacı ile, işlem bilgisayar ortamında simüle edilerek ezme uygulanan bölgede işlem sonrası oluşan kalıntı gerilim dağılımı hesaplanmıştır. Krank mili yorulma performansları her iki malzeme için ezme işlemi öncesi ve sonrasında yapılan yorulma testleri ile elde edilmiştir. Ayrıca farklı ezme kuvveti

kullanılan elik krank milleri ile yapılan testlerle ezme kuvvetinin etkisi deęerlendirilmiřtir. Yapılan testlerde, eęme yorulma kořulları altında, hem ezme iřlemi ncesinde hem de sonrasında sfero dkme demir krank millinin mikro alařımlı elik krank miline gre daha iyi yorulma performansı gsterdięi bilgisine ulařılmıřtır. te yandan, ezme iřleminin elik krank milinde yorulma performansını iyileřtirme anlamında daha etkili olduęu grlmřtir. Buna ek olarak, krank mili yorulma mukavemetinin artan ezme kuvveti ile birlikte yzey kalitesinin bozulmaya bařladıęı kuvvete kadar arttıęı gzlemlenmiřtir. Kalıntı gerilim analizleri, aynı kořullarda ezme iřlemi uygulanmıř elik krank millerinde daha yksek deęerlerde kalıntı gerilim deęerleri elde edilebileceęini, te yandan, dkme demir krank millerinde kalıntı gerilimlerin etkili derinlięinin daha yksek olduęunu gstermiřtir. Farklı ezme kuvvetleri kullanılarak iřlem uygulanan elik krank millerinde yapılan kalıntı gerilim analizleri, maksimum kalıntı gerilim deęerinin artan ykle birlikte nemli lde artmadıęını, fakat artan ezme kuvvetinin ana etkisinin etkili kalıntı gerilim derinlięini arttırması olduęunu gstermiřtir. Test verilerinin istatistik analizlerinde kullanılan MLE metodunun yorulma mr eęrilerinin elde edilmesinde ve yorulma mukavemeti daęılım analizlerinde etkili bir yntem olduęu sonucuna varılmıřtır. RFL modelinin Modified Basquin modeline gre yorulma mr eęrilerinin elde edilmesi ve yorulma limiti hesaplanmasında daha etkili olduęu grlmřtir. Dixon-Mood ynteminin ise yorulma limitini yksek deęerlerde tahmin ettięi sonucuna varılmıřtır.

Keywords: Yorulma, kalıntı gerilim, istatistiksel analiz, krank mili, ezme iřlemi.

*To the memory of my beloved grandfather
Mustafa...*

ACKNOWLEDGEMENTS

I would like to express my deepest gratitudes to Prof.Dr. Rıza Gürbüz for his supervision, excellent guidance and kindness throughout this journey.

I am grateful and indebted to Assist. Prof. Dr. Kazım Tur and Prof.Dr. Cemil Hakan Gür for their precious supports and advices during the study.

I would like to express my sincere thanks to Ergün Güraslan who sparked the initial lights of this study with his insightful vision. I am grateful to Ömer Rüştü Ergen who is “the” engineer model for me; to Dr.Ali Aslan Ebrinç for his kindness, encouragements and precious advices; to Cem Özen who was always very kind and always made me feel confident on my way; to Alper Akpınar and Özay Polat for their supports and understandings.

Very special thanks and gratitudes to Carlos C. Engler-Pinto Jr. and Cemal Gözen for their invaluable contributions to this study; and to the technical staff of Ford Otosan İnönü Engine Plant and Engine Test Center for their supports.

I am forever grateful to my family for their endless love and supports throughout my life. Special thanks to Elif Altuntaş, Gürsen Altın, Burçak Bora, Dr.Zeynep Büküm, Dr.Mine Camcı, Cenk Dinç, Erhan Doğruyol, Nurduran Duman, Tolga Duran, Selen Güner, Serdar Güryuva, Tahsin Hacıbekir, Dr.Göksu Kaya, Ezgi Kotan, Gökten Kurnaz, Dr. Gülgün Kuru, Sevgi Maç, Prof.Dr.Ata Mugan, Kaan Özdemir, Yahya Sahip, Assist.Prof.Dr.Caner Şimşir, Dr.Evren Tan, Biray Tataroğlu, Zafer Tuncalı, Hakan Uygun and Assist. Prof. Dr. Çekdar Vakıfahmetoğlu, for their friendships, supports and encouragements when they were most required.

TABLE OF CONTENTS

ABSTRACT.....	iv
ÖZ	vi
DEDICATION.....	viii
ACKNOWLEDGEMENTS.....	ix
TABLE OF CONTENTS	x
LIST OF FIGURES.....	xiv
LIST OF TABLES	xxiii
CHAPTERS	
1. INTRODUCTION	1
2. THEORY	5
2.1 Fatigue	5
2.1.1 Cyclic Stresses	6
2.1.2 The S-N Curve	7
2.1.3 Fatigue Crack Initiation and Propagation.....	9
2.1.4 Fracture Mechanics of Fatigue	14
2.1.4.1 Fatigue Crack Thresholds.....	15
2.1.4.2 Fatigue Crack Growth Rate and Crack Propagation Laws	16
2.1.5 Stress Fluctuation, Cumulative Damage and Safe-Life Design.....	18
2.1.6 Effect of Mean Stress on Fatigue Life	20
2.1.7 Surface Effects and Fatigue.....	22
2.1.7.1 Design Factors	22
2.1.7.2 Surface Treatments.....	23
2.1.7.3 Surface Residual Stresses	25

2.1.7.3.1 Mechanical Methods for Residual Stress	
Introduction.....	25
2.3 Statistical Considerations in Stress Based Fatigue Limit	
Studies.....	26
2.2.1 Definitions and Quantification of Data Scatter	27
2.2.2 Probability Distributions	28
2.2.2.1 Normal and Log-Normal Distributions	29
2.2.2.2 Weibull Distributions	30
2.2.3 Probabilistic Approach to Stress-Based Fatigue	
Analysis	32
2.2.3.1 Regression Analysis of the Fatigue Data.....	35
2.2.3.2 Advanced Fatigue Test Techniques and Statistical	
Analysis	38
2.2.3.2.1 Stair-Case Testing Method and Dixon-Mood	
Analysis.....	39
2.2.3.2.2 Random Fatigue Limit Model.....	41
2.3 State of the Art.....	44
2.3.1 Internal Combustion Engine Crankshafts.....	44
2.3.1.1 Function of Crankshafts in Internal Combustion	
Engines	44
2.3.1.2 Forces Acting on the Crankshaft.....	45
2.3.1.3 Crankshaft Materials	46
2.3.1.3.1 Forged Steel	47
2.3.1.3.2 Cast Iron.....	49
2.3.1.4 Surface Treatment of Crankshafts.....	51
2.3.1.4.1 Induction Hardening	52
2.3.1.4.2 Nitriding.....	54
2.3.1.4.3 Fillet Rolling	54
2.3.2 Fillet Rolling Process and Fatigue Strength	
Improvement	56
3. EXPERIMENTAL	58
3.1 Main Components of the Crankshaft	58

3.2 Material Characterization	59
3.2.1 Chemical Composition	59
3.2.2 Mechanical Properties	60
3.2.3 Microstructure.....	66
3.3 Surface Treatment of Crankshafts	68
3.3.1 Fillet Rolling Process and Test Matrix.....	69
3.3.2 Induction Hardening Process.....	73
3.3.3 Characterization of the Test Specimens	74
3.3.3.1 Undercut Microstructure.....	74
3.3.3.2 Undercut Depth and Radius	78
3.3.3.3 Undercut Hardness Profile.....	80
3.4 Resonant Bending Fatigue Tests.....	81
3.4.1 Resonant Bending Fatigue Test Data	84
3.4.2 Statistical Analyses of the Fatigue Test Results and Fatigue Limit Calculations	95
3.4.2.1 Fatigue Limit Calculations by Dixon-Mood Method...	96
3.4.2.2 Maximum Likelihood Method Calculations and Life Regressions	100
3.5 Fracture Characteristics	119
4. FINITE ELEMENT ANALYSIS	129
4.1 Residual Stress Calculations.....	129
4.1.1 Finite Element Model.....	129
4.1.2 Boundary Conditions and Analysis Steps	132
4.1.3 Residual Stress Calculation Results	134
4.2 Bending Test Stress Calculations	142
5. DISCUSSION	147
5.1 Methodology and Results.....	147
5.1.1 Resonance Bending Fatigue Tests	147
5.1.2 Staircase Test Methodology	150
5.1.3 Fractographic Analyses	151
5.1.4 Test Stress Calculations.....	152
5.1.5 Residual Stress Calculations by Finite Element Method	153

5.1.6 Statistical Analyses	159
5.1.6.1 Curve Fit Methods.....	159
5.1.6.2 Fatigue Limit Calculations.....	160
5.2 Discussion of the Effect of Fillet Rolling Process on Fatigue Performance	162
5.2.1 Comparison of Fatigue Performances of Ductile Cast Iron and Steel Crankshafts.....	162
5.2.2 Effect of Fillet Rolling Load on Fatigue Behavior of Steel Crankshafts.....	166
5.3 Comparison of Deformation Characteristics of EN-GJS 800-2 and MnVS6 Materials under Fillet Rolling	169
5.4 Effect of Rolling Load on Deformation Characteristics of 38MnVS6 Steel.....	170
5.5 Discussions on the Mechanisms of Fatigue Strength Improvement by Fillet Rolling Process	174
6. CONCLUSIONS	177
REFERENCES.....	180
VITAE	187

LIST OF FIGURES

FIGURES

Figure 2.1 Nomenclature to describe parameters in cyclic loading.....	6
Figure 2.2 Wohler's S-N curves for Krupp axle steel.....	8
Figure 2.3 Crack initiation propagation stages on S-N curve.....	9
Figure 2.4 Schematic representation showing stages I and II of fatigue crack propagation in polycrystalline metals.....	11
Figure 2.5 Fatigue crack propagation mechanism by repetitive crack tip plastic blunting and sharpening	12
Figure 2.6 Fracture surface of a rotating steel shaft that experienced fatigue failure	13
Figure 2.7 Transmission electron fractograph showing fatigue striations in aluminum	14
Figure 2.8 Schematic illustrations of different regimes of stable fatigue crack propagation	15
Figure 2.9 Fatigue crack growth rate diagram.....	18
Figure 2.10 Component cycle life.....	19
Figure 2.11 Representative plots of data showing the effect of stress amplitude and mean stress on fatigue life	21
Figure 2.12 Demonstration of how design can reduce stress amplification	23
Figure 2.13 Effects of surface finish on the fatigue limit of steel.....	24
Figure 2.14 Introduction of compressive residual stresses at the fillet radius by localized plastic deformation.....	26
Figure 2.15 Plots of normal distribution.....	30
Figure 2.16 Two-parameter Weibull distribution for different values of shape parameters	32

Figure 2.17 Conceptual S-N curves for specified P values	33
Figure 2.19. P-S-N surface showing P-N trace.....	34
Figure 2.20 Likelihood functions for the staircase test	36
Figure 2.21 Likelihood function definition for life-regression models for failures (NF) and run-outs (NR)	38
Figure 2.22 Illustration of the staircase test method	40
Figure 2.23 Fatigue life and fatigue strength distributions.....	42
Figure 2.24 Probabilistic S-N curves based on random fatigue limit modeling of nickel super-alloy data.....	43
Figure 2.25 (a) Schematic view of an engine illustrating the crankshaft rotation and piston motion (b) Schematic view of a crankshaft showing the main parts.....	45
Figure 2.26 Forces acting on crankshaft versus crank angular position	46
Figure 2.27 Forming steps of a four-cylinder automobile crankshaft.....	48
Figure 2.28 Layout of a forging line for crankshaft manufacturing	49
Figure 2.29 Shell mold with crankshaft	51
Figure 2.30. Characteristics of deep rolling.....	55
Figure 3.1 Schematic representation of the crankshaft and its main Features.....	58
Figure 3.2 Tension test specimen location	60
Figure 3.3 True stress-strain curve of EN GJS 800-2 ductile cast iron.....	62
Figure 3.4 True stress-strain curve of 38MnVS6 steel.....	62
Figure 3.5 Hardness profile of ductile cast iron crankshaft with respect to the measurement areas.....	64
Figure 3.6 Hardness profile of forged steel crankshaft with respect to the measurement areas.....	65
Figure 3.7 Hardness frequency distribution diagram of cast iron Crankshaft.....	65
Figure 3.8 Hardness frequency distribution diagram of forged steel Crankshaft.....	66
Figure 3.9 Microstructure showing the graphite nodules in pearlite matrix for EN-GJS 800-2 crankshaft material.....	67

Figure 3.10 Microstructure showing graphite nodules in pearlite matrix.....	67
Figure 3.11 Microstructure of 38MnVS6 steel.....	68
Figure 3.12 Schematic views of the undercut region and rolling operation.....	70
Figure 3.13 Crankshaft pin journal cross-section	71
Figure 3.14 Pin journal rolling process cycle	71
Figure 3.15 Main Journal rolling process cycle.....	72
Figure 3.16 Induction hardened area and the undercut region of the steel crankshaft.....	73
Figure 3.17 Microstructural view from the fillet region of EN GJS-800-2 crankshaft at unrolled condition, 100X	75
Figure 3.18 Microstructural view from the fillet region of EN GJS-800-2 crankshaft rolled at 15kN, 100X.....	75
Figure 3.19 Microstructural view from the fillet region of 38MnVS6 crankshaft at unrolled condition, 100X.....	76
Figure 3.20 Microstructural view from the fillet region of 38MnVS6 crankshaft rolled at 12.5kN, 100X	76
Figure 3.21 Microstructural view from the fillet region of 38MnVS6 crankshaft rolled at 15kN, 100X.....	77
Figure 3.22 Microstructural view from the fillet region of 38MnVS6 crankshaft rolled at 20kN, 100X.....	77
Figure 3.23 Microstructural view from the fillet region of 38MnVS6 crankshaft rolled at 24kN, 100X.....	78
Figure 3.24 Undercut profile of the steel crank at unrolled condition and the measurement locations	79
Figure 3.25 Schematic and actual views of the test set-up.....	83
Figure 3.26 S-N curve for EN-GJS 800-2 at unrolled condition.....	92
Figure 3.27 S-N curve for EN-GJS 800-2 rolled at 15kN fillet rolling load	92
Figure 3.28 S-N curve for 38MnVS6 at unrolled condition.....	93

Figure 3.29 S-N curve for 38MnVS6 rolled at 12.5kN fillet rolling load	93
Figure 3.30 S-N curve for 38MnVS6 rolled at 15kN fillet rolling load	94
Figure 3.31 S-N curve for 38MnVS6 rolled at 20kN fillet rolling load	94
Figure 3.32 S-N curve for 38MnVS6 rolled at 12.5kN fillet rolling load	95
Figure 3.33 Failure run-out history for EN GJS 800-2 at unrolled condition	96
Figure 3.34 Failure run-out history for EN GJS 800-2 rolled at 15kN fillet rolling load.....	97
Figure 3.35 Failure run-out history for 38MnVS6 at unrolled condition	97
Figure 3.36 Failure run-out history for 38MnVS6rolled at 12.5kN fillet rolling load.....	98
Figure 3.37 Failure run-out history for 38MnVS6rolled at 15kN fillet rolling load.....	98
Figure 3.38 Failure run-out history for 38MnVS6rolled at 20kN fillet rolling load.....	99
Figure 3.39 Failure run-out history for 38MnVS6rolled at 24kN fillet rolling load.....	99
Figure 3.40 Basquin curve fit for EN GJS 800-2 at unrolled condition.....	102
Figure 3.41 RFL curve fit for EN GJS 800-2 at unrolled condition	102
Figure 3.42 Probability density functions for EN GJS 800-2 at unrolled condition	103
Figure 3.43 Cumulative distribution functions for EN GJS 800-2 at unrolled condition	103
Figure 3.44 Basquin curve fit for EN GJS 800-2 rolled at 15kN rolling load	104
Figure 3.45 RFL curve fit for EN GJS 800-2 rolled at 15kN rolling load	104

Figure 3.46 Probability density functions for EN GJS 800-2 rolled at 15kN rolling load	105
Figure 3.47 Cumulative distribution functions for EN GJS 800-2 rolled at 15kN rolling load	105
Figure 3.48 Basquin curve fit for 38MnVS6 at unrolled condition.....	106
Figure 3.49 RFL curve fit for 38MnVS6 at unrolled condition.....	106
Figure 3.50 Probability density functions for 38MnVS6 at unrolled condition.....	107
Figure 3.51 Cumulative distribution functions for 38MnVS6 at unrolled condition	107
Figure 3.52 Basquin curve fit for 38MnVS6 rolled at 12.5kN rolling load	108
Figure 3.53 RFL curve fit for 38MnVS6 rolled at 12.5kN rolling load.....	108
Figure 3.54 Probability density functions for 38MnVS6 rolled at 12.5kN rolling load	109
Figure 3.55 Cumulative distribution functions for 38MnVS6 rolled at 12.5kN rolling load	109
Figure 3.56 Basquin curve fit for 38MnVS6 rolled at 15kN rolling load	110
Figure 3.57 RFL curve fit for 38MnVS6 rolled at 15kN rolling load.....	110
Figure 3.58 Probability density functions for 38MnVS6 rolled at 15kN rolling load	111
Figure 3.59 Cumulative distribution functions for 38MnVS6 rolled at 15kN rolling load	111
Figure 3.60 Basquin curve fit for 38MnVS6 rolled at 20kN rolling load	112
Figure 3.61 RFL curve fit for 38MnVS6 rolled at 20kN rolling load.....	112
Figure 3.62 Probability density functions for 38MnVS6 rolled at 20kN rolling load	113
Figure 3.63 Cumulative distribution functions for 38MnVS6 rolled at 20kN rolling load	113

Figure 3.64 Basquin curve fit for 38MnVS6 rolled at 24kN rolling load	114
Figure 3.65 RFL curve fit for 38MnVS6 rolled at 24kN rolling load.....	114
Figure 3.66 Probability density functions for 38MnVS6 rolled at 24kN rolling load	115
Figure 3.67 Cumulative distribution functions for 38MnVS6 rolled at 24kN rolling load	115
Figure 3.68 A schematic representation crack propagation direction along the crankshaft cross-section	119
Figure 3.69 Crack path on failure region on an EN-GJS 800-2 crankshaft sample rolled at 15kN.....	120
Figure 3.70 Crack surface from a fully fractured test specimen from EN-GJS 800-2 crankshaft rolled at 15kN.....	120
Figure 3.71 Crankshaft section showing the undercut region and induction hardened region	121
Figure 3.72 Crack along the section magnified by liquid penetrant	122
Figure 3.73 Primary and a secondary crack on a 38MnVS6 crankshaft sample rolled at 12.5kN.....	122
Figure 3.74 Fractograph showing the crack initiation region, X30 (EN-GJS 800-2 crankshaft rolled at 15kN)	123
Figure 3.75 Fractograph showing the crack initiation region, X150 (EN-GJS 800-2 crankshaft rolled at 15kN)	124
Figure 3.76 Fractograph showing the crack initiation region, X800 (EN-GJS 800-2 crankshaft rolled at 15kN)	124
Figure 3.77 Graphite nodules in pearlite matrix, X1000 (EN-GJS 800-2 crankshaft rolled at 15kN)	125
Figure 3.78 Graphite nodule in pearlite matrix, X1800 (EN-GJS 800-2 crankshaft rolled at 15kN)	125
Figure 3.79 Multiple crack initiation sites at the undercut region, X12 (38MnVS6 crankshaft rolled at 12.5kN)	126
Figure 3.80 Fractograph showing the two crack initiation sites, X1400 (38MnVS6 crankshaft rolled at 12.5kN).....	127

Figure 3.81 Fatigue striations in the crack propagation zone, X2200 (38MnVS6 crankshaft rolled at 12.5kN)	127
Figure 3.82 Cleavage planes from final fracture region, X850 (38MnVS6 crankshaft rolled at 12.5kN)	128
Figure 3.83 River patterns from the final fracture region, X1900 (38MnVS6 crankshaft rolled at 12.5kN)	128
Figure 4.1 Model for rolling process; crankshaft section and the roller	130
Figure 4.2 View from the fillet region and the roller	131
Figure 4.3 More detailed view of the roller and the fillet region at the contact area showing the varying element sizes	131
Figure 4.4 The roller and the local axis	132
Figure 4.5 Crankshaft reference points for defining the boundary conditions	133
Figure 4.6 Crankshaft section and the end planes from side view	134
Figure 4.7 Stress contour along the rolling path	135
Figure 4.8 Residual stress reading direction	135
Figure 4.9 Stress contour on the crankshaft cross-section under rolling load	136
Figure 4.10 Stress contour on the crankshaft cross-section after load removal	136
Figure 4.11 Stress profiles for EN GJS 800-2 crankshaft rolled at 15kN, under load and after load removal	137
Figure 4.12 Stress profiles for 38MnVS6 crankshaft rolled at 12.5kN, under load and after load removal	138
Figure 4.13 Stress profiles for 38MnVS6 crankshaft rolled at 15kN, under load and after load removal	138
Figure 4.14 Stress profiles for 38MnVS6 crankshaft rolled at 20kN, under load and after load removal	139
Figure 4.15 Stress profiles for 38MnVS6 crankshaft rolled at 24kN, under load and after load removal	139
Figure 4.16 Residual stress profile for EN GJS 800-2 crankshaft rolled at 15kN	140

Figure 4.17 Residual stress profile for 38MnVS6 crankshaft rolled at 12.5kN	140
Figure 4.18 Residual stress profile for 38MnVS6 crankshaft rolled at 15kN	141
Figure 4.19 Residual stress profile for 38MnVS6 crankshaft rolled at 20kN	141
Figure 4.20 Residual stress profile for 38MnVS6 crankshaft rolled at 24kN	142
Figure 4.21 Crankshaft dimensions related to stress concentration factor at the fillet region	144
Figure 4.22 CAE model for the Resonance Bending Test	145
Figure 4.23 Representative stress contour at the fillet region	146
Figure 5.1 Frequency change with number of cycles throughout testing of un-rolled EN-GJS 800-2 crankshaft tested under 8.25kN load amplitude	149
Figure 5.2 Load amplitude versus number of cycles throughout testing of un-rolled EN-GJS 800-2 crankshaft tested under 8.25kN load amplitude.....	149
Figure 5.3 Mean load versus number of cycles throughout testing of un-rolled EN-GJS 800-2 crankshaft tested under 8.25kN load amplitude.....	150
Figure 5.4 Comparison of residual stress profiles of EN-GJS 800-2 and 38MnVS6 crankshafts fillet rolled at 15kN	154
Figure 5.5 Comparison of residual stress profiles of 38MnVS6 crankshafts fillet rolled under different loads.....	155
Figure 5.6 Polynomial fit residual stress profiles of 38MnVS6 crankshafts at different rolling load conditions	155
Figure 5.7 Loading-unloading simulation of rolling process on true stress-strain curve for EN-GJS 800-2 crankshaft	158
Figure 5.8 Loading-unloading simulation of rolling process on true stress-strain curve for 38MnVS6 crankshaft	158
Figure 5.9 S-N curves of EN-GJS 800-2 and 38MnVS6 crankshafts at unrolled condition	163

Figure 5.10 S-N curves of EN-GJS 800-2 and 38MnVS6 crankshafts fillet rolled under 15kN rolling load	165
Figure 5.11 S-N curves of EN-GJS 800-2 crankshaft at unrolled condition and fillet rolled under 15kN rolling load	165
Figure 5.12 S-N curves 38MnVS6 steel crankshaft at unrolled condition and fillet rolled under 15kN rolling load.....	166
Figure 5.13 S-N curves of 38MnVS6 crankshafts at unrolled condition and fillet rolled under different rolling loads.....	167
Figure 5.14 S-N curves of 38MnVS6 crankshafts fillet rolled under different rolling loads	168
Figure 5.15 Fatigue strength versus rolling load for 38MnVS6 crankshafts	169
Figure 5.16 Undercut depth versus rolling load for 38MnVS6 crankshafts	171
Figure 5.17 Undercut radius versus rolling load for 38MnVS6 crankshafts	172
Figure 5.18 Undercut hardness versus rolling load for 38MnVS6 crankshafts	172
Figure 5.19 Fillet surface qualities of 38MnVS6 crankshafts at 24 and 20kN rolling conditions.....	173

LIST OF TABLES

TABLES

Table 2.1 Surface treatments for crankshafts	52
Table 3.1 Chemical Composition of EN GJS 800-2 ductile cast iron	59
Table 3.2 Chemical Composition of 38MnVS6 Forged Steel.....	60
Table 3.3 Mechanical properties of EN GJS 800-2 ductile cast iron and 38MnVS6 forged steel	61
Table 3.4 Strength coefficient and strain hardening exponent values for EN GJS 800-2 ductile cast iron and 38MnVS6 forged steel	63
Table 3.5 Hardness profile of ductile cast iron crankshaft.....	64
Table 3.6 Hardness profile of steel crankshaft	64
Table 3.7 Crankshaft design conditions	72
Table 3.8 Undercut depth and radius measurements at different rolling load conditions for EN-GJS 800-2 crankshafts	79
Table 3.9 Undercut depth and radius measurements at different rolling load conditions for 38MnVS6 crankshafts	80
Table 3.10 Increase in undercut depth and radius at different rolling conditions for cast iron and steel crankshafts	80
Table 3.11 Undercut hardness profiles at different rolling conditions for EN-GJS 800-2 crankshafts	81
Table 3.12 Undercut hardness profiles at different rolling conditions for 38MnVS6 crankshafts.....	81
Table 3.13 Fatigue test data for EN-GJS 800-2 at unrolled condition.....	85
Table 3.14 Fatigue test data for EN-GJS 800-2 rolled at 15kN fillet rolling load.....	86
Table 3.15 Fatigue test data for 38MnVS6 at unrolled condition.....	87
Table 3.16 Fatigue test data for 38MnVS6 rolled at 12.5kN fillet rolling Load.....	88

Table 3.17 Fatigue test data for 38MnVS6 rolled at 15kN fillet rolling	
Load.....	89
Table 3.18 Fatigue test data for 38MnVS6 rolled at 20kN fillet rolling	
Load.....	90
Table 3.19 Fatigue test data for 38MnVS6 rolled at 24kN fillet rolling	
Load.....	91
Table 3.20 Dixon-Mood calculation results	100
Table 3.21 Summary of MLE results for EN GJS 800-2 at unrolled condition	116
Table 3.22 Summary of MLE results for EN GJS 800-2 rolled at 15kN rolling load.....	116
Table 3.23 Summary of MLE results for 38MnVS6 at unrolled condition	116
Table 3.24 Summary of MLE results for 38MnVS6 rolled at 12.5kN rolling load.....	117
Table 3.25 Summary of MLE results for 38MnVS6 rolled at 15kN rolling load.....	117
Table 3.25 Summary of MLE results for 38MnVS6 rolled at 20kN rolling load.....	117
Table 3.26 Summary of MLE results for 38MnVS6 rolled at 20kN rolling load.....	118
Table 3.28 Definitions of Modified Basquin and RFL model parameters.....	118
Table 3.29 Modified Basquin and RFL model parameter values	118
Table 5.1 Summary of residual stress analysis	154
Table 5.2 Summary of fatigue strength data of 38MnVS6 crankshafts at unrolled condition and fillet rolled under different rolling loads.....	168

CHAPTER 1

INTRODUCTION

Crankshaft of an internal combustion engine is mainly subjected to bending and torsional stresses. Explosion and inertia forces create cycling bending stresses on the crankshaft. Transmission of the engine torque and torsional vibrations create torsional stresses; and their variations with time create cyclic stresses on the crankshaft during its service life. This explains why most common crankshaft failure type is fatigue. Thus, one of the main design parameters of a crankshaft during design stage is to withstand these cycling bending and torsional stresses. Crankshaft is one of the most critical parts of an engine since any failure on crankshaft may result in catastrophic failure of the engine. This fact has formed basis of the motivation of the studies aiming the fatigue performance optimization of the crankshafts both in automotive industry and in academic areas.

Fatigue failures on crankshafts are usually observed at fillet regions where a stress concentration is eventually present, due to the crankshaft geometry at this region. Other critical regions for crack initiation are the pin surface and oil hole ends on the crankshaft surface.

Since the fatigue failures almost always occur by crack initiation and propagation at the fillet region under bending, a typical fillet rolling process is being used for many years to improve the fatigue lifetime of crankshafts. By fillet rolling process compressive residual stresses are introduced near the fillet region. Developed compressive stresses increase the fatigue life by compensating the tensile stress components created during working conditions.

In order to obtain a suitable geometry for the roller to fit onto, an undercut having a radius of curvature is formed at this region for local mechanical loading, which is called the undercut region.

Studies on the fillet rolling process and corresponding effect on the fatigue performance of a crankshaft are in the scope various studies aiming different aspect of the phenomena.

From the testing point of view, in order to understand the nature of fatigue and effect of process and design parameters on the crankshaft performance, there is a need to map the fatigue performance of the crankshafts experimentally with the aim of addressing to in-service performance. Other aspects of experimental studies are to explore the empirical relationship of different failure criteria – specifically, surface crack initiation, resonant shifts, and two-piece failures – with the bending fatigue limit sections.

From the analytical point of view, there is a need to determine an engineering practice for residual stress simulation and fatigue limit determination based on residual stress development.

Although numerous experimental, theoretical and analytical studies were conducted on fillet rolling and crankshaft fatigue performance, there is still a large need for new researches in this area to obtain the effects of process parameters on fatigue performance of the crankshafts as well as predicting the in-service fatigue performance by analytical techniques. In addition, studies aiming to understand and evaluate the mechanisms of fatigue strength improvement by fillet rolling are also required.

Another important fact in fatigue analysis of engineering components is the research need for the development of best-practice methods to evaluate the stress versus number of cycles curves and the fatigue limit.

Main objective of this work is to evaluate the effect of fillet rolling process on fatigue strength of a five-cylinder crankshaft used in diesel engine applications. Experimental, analytical and statistical methods were utilized for this purpose.

In experimental part, crankshafts from two different materials were subjected to resonant bending fatigue tests in order to evaluate the stress versus number of cycles behavior. Staircase testing methodology was applied for bending fatigue tests. Crankshaft materials used were EN GJS 800-2 grade ductile cast iron and 38MnVS6 micro-alloyed steel, which are widely used in diesel engine crankshaft applications. Both material type of crankshafts with machined undercuts were firstly subjected to resonant bending fatigue tests without any fillet rolling applications. The same experimental studies were then conducted with crankshafts, which were fillet rolled at 15kN. In addition, bending fatigue tests were conducted with steel crankshafts rolled at four different rolling loads in order to evaluate the effect of fillet rolling load on fatigue performance.

The experimental data obtained were analyzed statistically both in aspects of fatigue limit determination and S-N curve evaluation. In order to evaluate the best-fit S-N curves, two different regression models were studied, a Modified Basquin Model and Random Fatigue Limit Model which are based on Maximum Likelihood methodology. For determination of fatigue limits for each design condition, the same models were utilized in addition to application of Dixon-Mood and Maximum Likelihood Methods by assuming Normal and Weibull type of distributions of the test data.

In addition to fatigue performance analysis, degrees of plastic deformation at the undercut region were also evaluated and compared for different design conditions to shed light on the effects of fillet rolling process.

The Computer Aided Analysis part of this study includes the calculation of residual stresses by Finite Element Method. For this purpose, rolling process was simulated by the use of a three dimensional explicit dynamic model with

the use of commercial software ABAQUS. Residual stresses for each rolling condition studied in the experimental part were calculated.

The obtained test data and developed methodology within the frame this study to estimate the nature and effect of fillet rolling process on fatigue performance are strongly predicted to shed light on crankshaft fatigue improvement studies, by supplying a know-how on the fillet rolling process. The obtained and presented know-how is believed to assist design optimization studies of crankshafts, avoiding overdesign, accompanied by cost and time saving.

CHAPTER 2

THEORY

2.1 Fatigue

Engineering structures are designed to withstand a variety of in-service loading and environmental conditions specific to their application purposes. Materials, manufacturing processes and strengthening methods are selected and designed for the component to be resistant to a variety of damage mechanisms to include yielding, creep deformation, fatigue crack growth, fretting fatigue, and oxidation.

Fatigue is defined as a form of failure, which occurs structures subjected to dynamic and fluctuating stresses. Under these conditions, failure may occur at stress levels lower than the yield strength of the material. Fatigue type of failure is brittle like in nature even in normally ductile metals. The fatigue process occurs by crack initiation and propagation mechanisms and ordinarily the fracture surface is perpendicular to the direction of applied tensile stress [1].

Since many components are subjected to cyclic stress and strain, there is no doubt that fatigue is one of the major failure mechanisms in engineering components. Thus, fatigue is a primary and critical criterion in the testing, analysis, and design of engineering materials for structural components. Fatigue has been known for more than 150 years, and for more than 100 years, engineering practices has been utilized to characterize the fatigue resistance of materials against cyclic loading [2].

Fatigue studies are based on three main approaches. The traditional approach is based on alternating and mean stresses to define the fatigue resistance of materials or components under the applied loading cycles. This approach is called as stress-based approach and covers the effects of stress raisers such as grooves, holes and notches. The second approach is the strain-based approach, which deals with the analysis of the localized plastic deformation at the area of interest. The third approach is the fatigue analysis based on fracture mechanics which deals with the crack initiation and propagation mechanisms [3].

2.1.1 Stress Cycles

Standard definitions regarding key stress variables of cyclic stresses are shown in Figure 2.1 on a regular sinusoidal form of stress cycles [1];

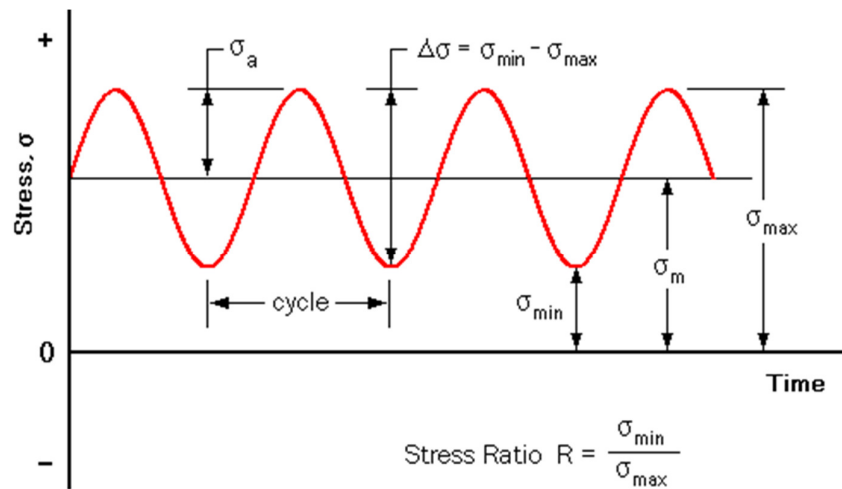


Figure 2.1 Nomenclature to describe parameters in cyclic loading [1].

Stress range is the difference between maximum and minimum stress and defined by the equation;

$$\Delta\sigma = \sigma_{\max} - \sigma_{\min} \quad (2.1)$$

Stress amplitude is one-half of stress range and defined as;

$$\Delta\sigma = \frac{\sigma_{\max} - \sigma_{\min}}{2} \quad (2.2)$$

The stress amplitude alternates about a mean stress, which is defined as the average of the maximum and minimum stresses in the cycle as;

$$\Delta\sigma = \frac{\sigma_{\max} + \sigma_{\min}}{2} \quad (2.3)$$

Stress ratio, R, is the ratio of maximum and minimum stress values and defined as;

$$\Delta\sigma = \frac{\sigma_{\max}}{\sigma_{\min}} \quad (2.4)$$

2.1.2 The S-N Curve

Wöhler was one of the earliest investigators who studied on the stress-controlled cyclic loading effects on fatigue life [4]. He studied railroad wheel axles that suffered from a series of failures. Outcomes of this study built up the basis of stress-number of cycles to failure (S-N diagram) (Figure 2.2) [5].

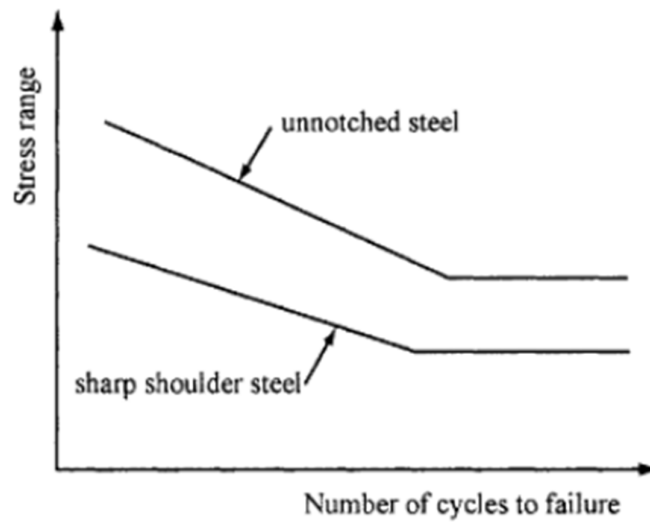


Figure 2.2 Wohler's S-N curves for Krupp axle steel [5].

The S-N curve interprets that fatigue life of the axle increases with decreasing stress level until an infinite life is reached below a certain stress level, which is called endurance limit or fatigue limit or fatigue strength. Wöhler's approach has been used widely in fatigue strength studies for stress-life studies and has also lead to the development of strain-life curves with the usage of same principles.

This study has led to revelation of another important fact that fatigue life reduces drastically by the presence of a notch. These observations have led investigators to review fatigue as a three-stage process involving initiation, propagation and final failure stages (Figure 2.3) [3].

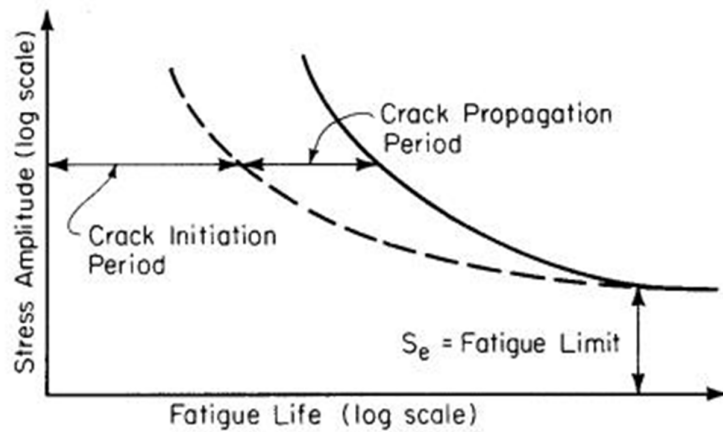


Figure 2.3 Fatigue life depends on relative extent of initiation and propagation stages [3].

2.1.3 Fatigue Crack Initiation and Propagation

The process of fatigue failure is characterized by three steps [1];

- (1) Crack initiation, wherein a small crack forms at some point of high stress concentration;
- (2) Crack propagation, during which this crack advances incrementally with each stress cycle; and
- (3) Final failure, which occurs very rapidly once the advancing crack has reached a critical size.

The fatigue life N_f , the total number of cycles to failure, can be taken as the sum of the number of cycles for crack initiation N_i and crack propagation N_p [1]:

$$N_f = N_i + N_p \quad (2.5)$$

Contribution of the final failure step to the total fatigue life is not included to the total life since it occurs rapidly. Relative proportions to the total life of N_i and N_p depend on the particular material and test conditions. At low stress levels (i.e., for high cycle fatigue), a large fraction of the fatigue life is utilized in crack initiation. With increasing stress level, N_i decreases and the cracks form more rapidly. Thus, for low-cycle fatigue (high stress levels), the propagation step predominates (i.e., $N_p > N_i$) [1].

Most usually, fatigue cracks initiate or in other words nucleate on the surface of a component where a stress concentration is present. Crack nucleation sites include surface scratches, sharp fillets, keyways, threads, dents, and the like. In addition to these, cyclic loading can itself produce microscopic surface discontinuities resulting from dislocation slip steps which may also act as stress raisers, and therefore as crack initiation sites [1].

A nucleated stable crack initially propagates very slowly along crystallographic planes of high shear stress (in polycrystalline metals); this stage is termed as *stage I crack propagation* (Figure 2.4). This stage may form a large or small fraction of the total fatigue life depending on stress level and the nature of the test specimen. High stresses and the presence of notches result in a short stage I propagation. During this stage, cracks normally extend through only several grains in polycrystalline metals. The fatigue surface that is formed during stage I propagation has a flat and featureless appearance [1].

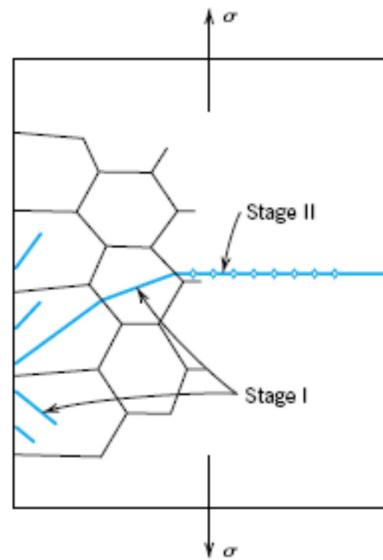


Figure 2.4 Schematic representation showing stages I and II of fatigue crack propagation in polycrystalline metals [1].

In the *stage II crack propagation*, the crack extension rate increases dramatically. In addition, there is also a change in propagation direction to a roughly perpendicular direction to the applied tensile stress in stage II (Figure 2.4). As illustrated in Figure 2.5, crack growth proceeds by repetitive plastic blunting and sharpening process at the crack tip during this stage. At the beginning of the stress cycle (zero or maximum compressive load), the crack tip has a form of a sharp double-notch (Figure 2.5.a). As the tensile stress is applied (Figure 2.5.b), localized deformation occurs at each of these tip notches along slip planes, oriented at 45° angles relative to the plane of the crack. With increasing crack length, the crack tip advances by continued shear deformation and the assumption of a blunted configuration (Figure 2.5.c). During compression, the directions of shear deformation at the crack tip are reversed (Figure 2.5.d) until, at the culmination of the cycle, a new sharp double-notch tip has formed (Figure 2.5.e) [1].

This process is repeated with each loading cycle until a critical crack dimension is achieved which leads the final failure step and catastrophic failure ensues [1].

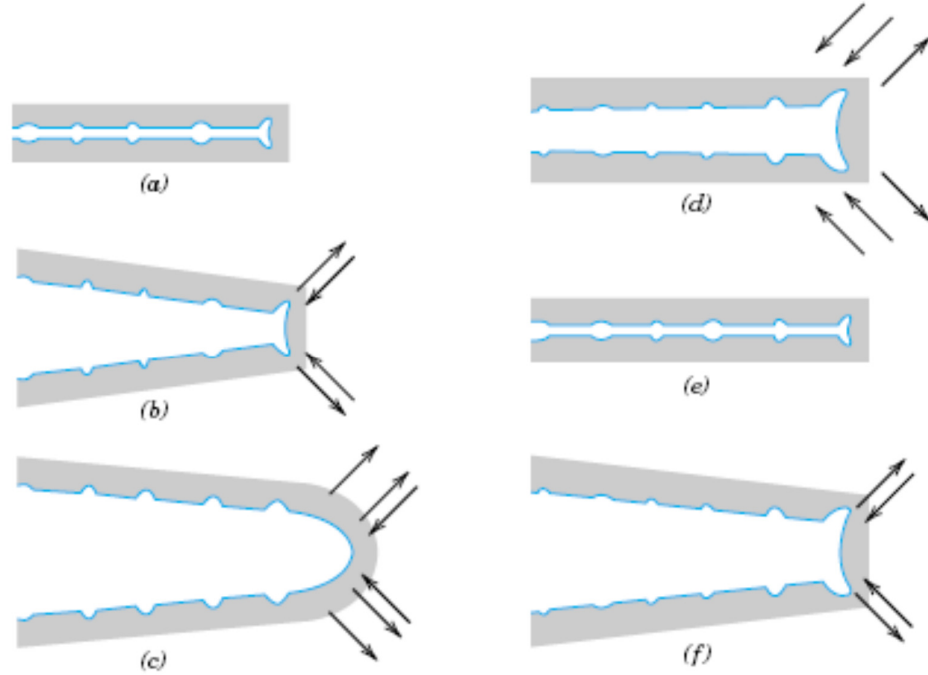


Figure 2.5 Fatigue crack propagation mechanism (stage II) by repetitive crack tip plastic blunting and sharpening: (a) zero or maximum compressive load, (b) small tensile load, (c) maximum tensile load, (d) small compressive load, (e) zero or maximum compressive load, (f) small tensile load. The loading axis is vertical [1].

The fracture surface that formed during stage II propagation can be characterized by two types of markings which are termed as beach-marks and striations. Both of these features indicate the position of the crack tip at some point in time and appear as concentric ridges that expand away from crack

initiation sites, frequently in a circular or semicircular pattern. Beach-marks are of macroscopic dimensions, and may be observed with an unaided eye (Figure 2.6). On the other hand, fatigue striations are microscopic in size and subject to observation with the electron microscope either with TEM or SEM (Figure 2.7) [1].

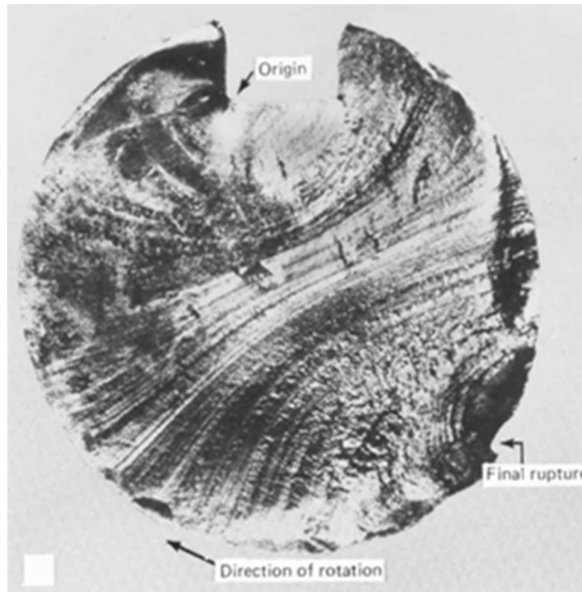


Figure 2.6 Fracture surface of a rotating steel shaft that experienced fatigue failure. Beach-mark ridges are visible in the photograph [6].



Figure 2.7 Transmission electron fractograph showing fatigue striations in aluminum. Magnification unknown [7].

2.1.4 Fracture Mechanics of Fatigue

S-N and ϵ -N curve approach is usually appropriate for situations where a component or structure can be considered a continuum (i.e., those meeting the “no cracks” assumption). In the presence of a crack, stress field at the crack tip should be defined in terms of stress intensity in linear elastic fracture mechanics. It recognizes the singularity of stress at the tip and provides a tractable controlling quantity and measurable material property. Linear elastic fracture mechanics relates the magnitude and distribution of stress at the crack tip to the nominal stress applied; to the size, shape and orientation of the crack; and the crack growth and fracture resistance of the material. The linear elastic fracture mechanics procedure is based on the analysis of stress-field equations, which show that the elastic stress field can be described by a single parameter, K ; the stress-intensity factor. For fatigue type of loading, the stress-intensity factor range parameter, ΔK is used. The use of the stress intensity range as a controlling quantity for crack propagation under cyclic loading enables

engineering analysis of the fatigue process in fracture mechanics point of view. [2].

2.1.4.1 Fatigue Crack Thresholds

The minimum value of stress intensity range, required for fatigue crack to start propagating by cyclic loading, is defined as the fatigue crack threshold. Below this value, no crack propagation occurs. Fatigue crack threshold is a function of a number of variables, including the material, the test conditions, the R -ratio, and the environment. ASTM E 647 defines the fatigue crack growth threshold, ΔK_{th} , as that asymptotic value of ΔK at which da/dN approaches zero [2].

For most materials, an operational definition of ΔK_{th} is given as that ΔK which corresponds to a fatigue crack growth rate of 10^{-10} m/cycle. Figure 2.8 depicts the form of the da/dN versus ΔK plot, where a is the crack length, N is the number of cycles, and ΔK is the range of the stress-intensity factor in a loading cycle. The curve shown is bounded by two limits, where the upper limit is the fracture toughness of the material and the lower limit is the threshold stress intensity range [2].

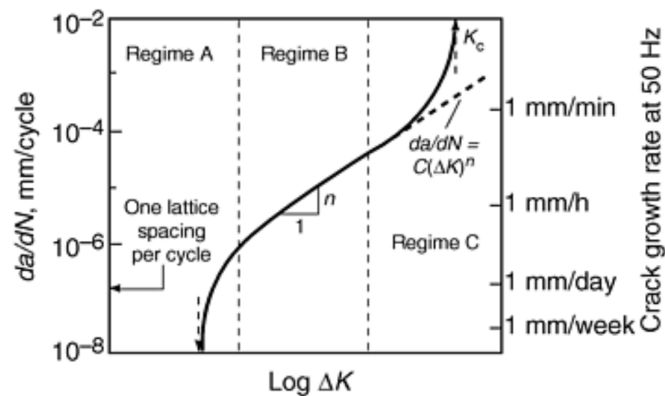


Figure 2.8 Schematic illustrations of different regimes of stable fatigue crack propagation [8].

2.1.4.2 Fatigue Crack Growth Rate and Crack Propagation Laws

The fatigue crack growth rate can be defined as the crack extension, Δa , within a number of cycles, ΔN , and expressed as the ratio $\Delta a / \Delta N$. This crack growth rate can also be written as da/dN which describes the slope of crack growth curve (a vs. N curve) [2].

When a component or a specimen containing a crack is subjected to cyclic loading, the crack length (a) increases with the number of fatigue cycles, N, if the load amplitude (ΔP), loading ratio (R) and the frequency of the cyclic loading (f) are kept constant. The crack growth rate, da/dN increases as the crack length increases during the cyclic loading. In addition to these, da/dN will also be higher at higher load amplitudes. The following expression is derived to describe this combined effect [2].

$$\left[\frac{da}{dN} \right]_{R,f} = f(\Delta P, a) \quad (2.6)$$

where the function “f” is dependent on the geometry of the specimen, the crack length, the loading configuration and the cyclic load range. This relation is simplified by the use of the stress intensity factor range parameter, ΔK , which is a function of the magnitude of the load range, ΔP , as well as the crack length and the geometry [2].

ΔK can be described as;

$$\Delta K = K_{\max} - K_{\min} \quad (2.7)$$

$$\Delta K = Y\sigma_{\max}\sqrt{\pi a} - Y\sigma_{\min}\sqrt{\pi a} = Y\Delta\sigma\sqrt{\pi a} \quad (2.8)$$

where Y is the geometric factor [1].

When the minimum stress is compressive or zero σ_{\min} is taken as zero in this equation [1].

Stage II crack propagation rate dependency to stress, strain, crack length and geometry has been the subject of a number of studies in order to implement a fail-safe design philosophy with the aim of determining the safe load and crack length which will preclude failure in a conservatively estimated service life [9, 10, 11, 12 and 13]. Among these, the relationship of crack growth rate and stress intensity factor range defined by Paris and Erdoğan [11] has been widely accepted as a crack propagation rule to describe the stage II crack propagation region. The equation suggested by this work is [11]

$$\frac{da}{dN} = C(\Delta K)^n \quad (2.9)$$

where C and n are experimentally determined material constants; which can be obtained from the intercept and slope, respectively, of the linear crack growth rate curve on a logarithmic scale [2]. Figure 2.9 describes the fatigue crack growth rate diagram with the demonstrated main regions and features.

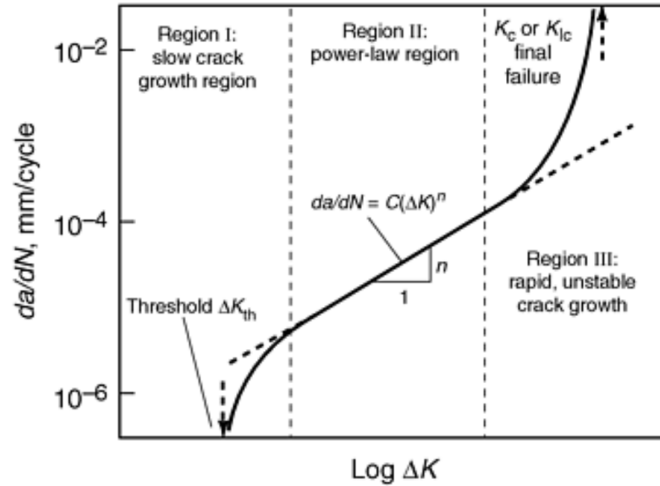


Figure 2.9 Fatigue crack growth rate diagram [2].

2.1.5 Stress Fluctuation, Cumulative Damage and Safe-Life Design

Discussions in the previous section are valid for constant amplitude, constant frequency loading conditions. However, real service conditions are more complicated where structures are subjected to alternating ranges of load fluctuations, mean levels and frequencies. In these conditions, in order to predict the life of the component based on constant amplitude loading, a number of cumulative damage theories were proposed. Palmgren [14] and Miner [15] equation is often used to describe the relative effect of stress levels and amount of damage introduced on a component. Cumulative damage approach assumes that the amount of damage on a component can be calculated as fractions of total life induced by different stress levels depending on the S-N diagram data as described in Figure 2.10 where $n_1/N_1 + n_2/N_2 + n_3/N_3 = 1$, as an example [3].

In a more general form;

$$\sum_{i=1}^k \frac{n_i}{N_i} = 1 \quad (2.10)$$

where

k : number of stress levels in the block loading spectrum

σ_i : i th stress level

n_i : number of cycles applied at σ_i

N_i : fatigue life at σ_i

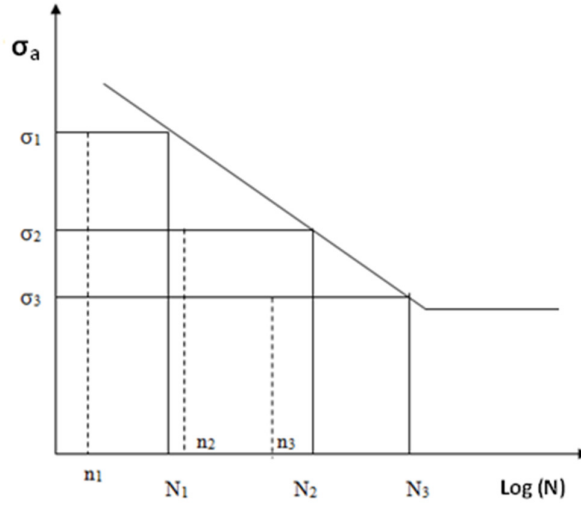


Figure 2.10 Component cycle life determined from $\sum_{i=1}^k \frac{n_i}{N_i} = 1$ assuming that damage at σ_i is a linear function of n_i (re-illustrated from [3]).

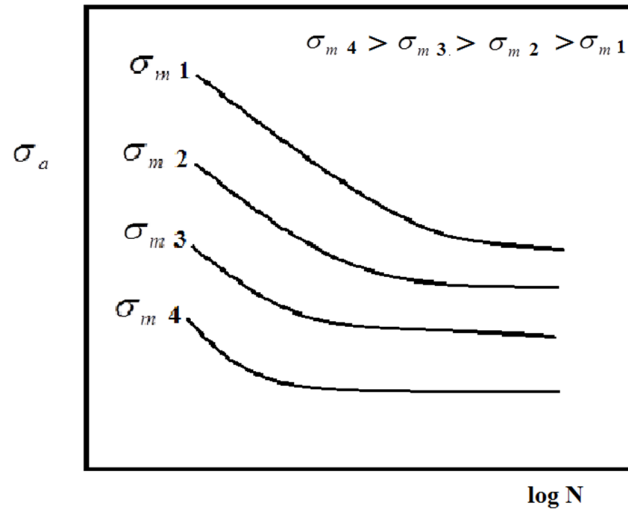
By combining the equation determined by Palmgren and Miner with S-N curve, total or residual service life-time of a structural component, experiencing multiple load sequences, can be estimated [3].

Above described methods are used in Safe-Life design, where components are removed from service before total life-time is completed to avoid failure. This criterion uses the S-N curve approach. Usually a safety factor is introduced, value of which depends on how much critical the part and service conditions is [3].

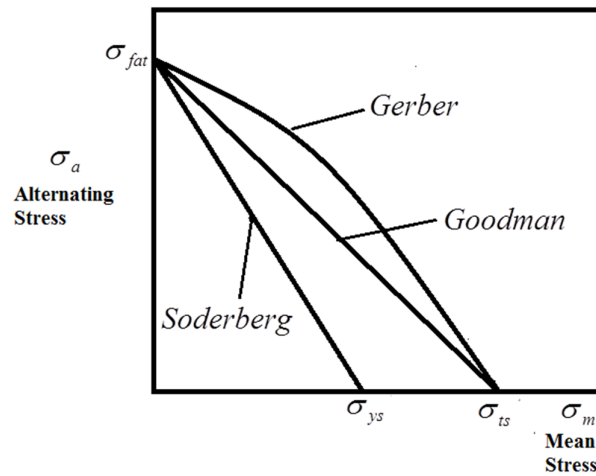
On the other hand, Fail-Safe design criterion depends on that cracks can develop in components and the crack can be detected before the component fails [3]. Approach based on the Fail-Safe design and studying the fracture mechanics concepts is called Damage Tolerant Design.

2.1.6 Effect of Mean Stress on Fatigue Life

Mean stress represents an important variable in the evaluation of a material's fatigue response and is a necessary for fatigue life data as a function of two stress variables. Figure 2.11 shows S-N curves at different mean stress values of the same material for a constant stress amplitude level. Depending on this fact, different researchers developed empirical relations, which are described by the equations 2.11, 2.12 and 2.13 [3];



(a)



(b)

Figure 2.11 Representative plots of data showing the effect of stress amplitude and mean stress on fatigue life. (a) Typical S-N diagrams with different mean stress levels (b) Goodman [16], Gerber [17] and Soderberg[18] diagrams showing combined effect of alternating and mean stress on fatigue endurance (re-illustrated from [3]).

$$\text{Goodman Relation : } \sigma_a = \sigma_{fat} \left(1 - \frac{\sigma_m}{\sigma_{ts}}\right) \quad (2.11)$$

$$\text{Gerber Relation : } \sigma_a = \sigma_{fat} \left(1 - \left(\frac{\sigma_m}{\sigma_{ts}}\right)^2\right) \quad (2.12)$$

$$\text{Soderberg Relation : } \sigma_a = \sigma_{fat} \left(1 - \frac{\sigma_m}{\sigma_{ys}}\right) \quad (2.13)$$

Above relations illustrate the effect of stress amplitude and mean stress on fatigue endurance. Experiences have shown that most data lie between the Gerber and Goodman diagrams; the latter represents more conservative design criteria for mean stress effects [3].

2.1.7 Surface Effects and Fatigue

Since most of the fatigue cracks initiate from the surface of a component, fatigue life is highly sensitive to surface condition and configuration. Surface effects can be classified mainly as design factors and surface treatments [1].

2.1.7.1 Design Factors

Presence of notches or geometrical discontinuities, such as grooves, holes, keyways, threads, etc. can act as stress raisers and so as potential fatigue crack initiation sites. Severity of stress concentration depends on the sharpness and configuration of the geometrical stress raiser with respect to the load. Improvement against fatigue can be obtained by avoiding these structural irregularities or by design modifications. These modifications may include reducing the sharpness of the notches such as introducing rounded fillets with larger radius of curvatures. Figure 2.12 shows an example of introduction of rounded fillets on a rotating shaft to decrease stress concentration [1].

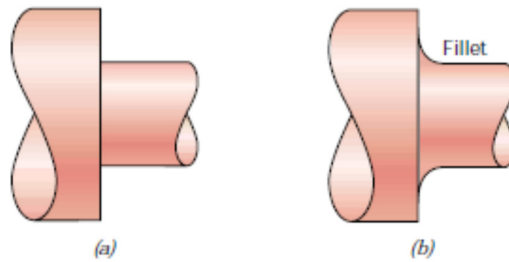


Figure 2.12 Demonstration of how design can reduce stress amplification. (a) Poor design: sharp corner. (b) Good design: fatigue lifetime improved by incorporating rounded fillet into a rotating shaft at the point where there is a change in diameter [1].

2.1.7.2 Surface Treatments

Small scratches and grooves are inevitably introduced into the work piece surface by the tool action during machining operations, which in turn advances the fatigue crack initiation process. It has been observed that improving the surface finish by polishing will enhance fatigue life significantly [1].

Surface effects on fatigue limit are caused by the differences in surface roughness, microstructure, chemical composition and residual stresses. Since surface conditions are usually effective in crack nucleation stage, surface effects are usually pronounced in high cycle fatigue phenomena where a greater or valuable percentage of cycles is usually involved with crack nucleation [19].

Figure 2.13 shows the effects of surface finish on the fatigue limit of steel; which proposes surface factors associated with decrease in fatigue limit for various tensile strength of steels [20].

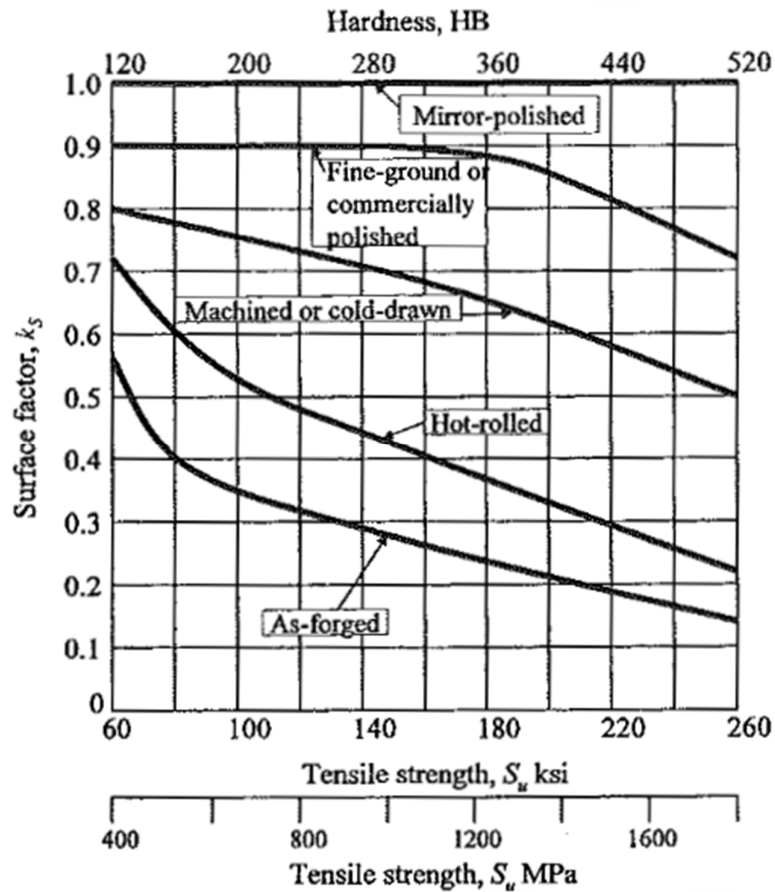


Figure 2.13 Effects of surface finish on the fatigue limit of steel [20].

Methods, which are based on increasing the surface hardness, are largely used as fatigue improvement methods. Case hardening is one of these methods by which a carburizing or nitriding process is applied whereby a component is exposed to a carbonaceous or nitrogenous atmosphere at an elevated temperature. A carbon- or nitrogen-rich outer surface layer, which is called “case” is introduced by atomic diffusion from the gaseous phase. The improvement of fatigue performance by surface hardening methods depend on the fact that crack initiation and propagation stages are retarded with the increased hardness as well as the residual stresses developed on the surface [1].

2.1.7.3 Surface Residual Stresses

Introduction of residual stresses is one of the most effective methods which include mechanical or thermal processes for residual stress production.

Residual stresses are the remaining stresses after an operation is applied on an engineering structure and are also called self-equilibrating stresses because they are in equilibrium within a part, without any external load. When the residual stresses present are in tensile form, they decrease the fatigue life of a component and thus should be avoided. On the other hand, compressive residual stresses improve the strength of the material against fatigue; by compensating the tensile stresses to an extent depending on the magnitude (of residual stresses) [19].

Methods for inducing residual stresses can be divided into four main categories as mechanical methods, thermal methods, plating and machining.

2.1.7.3.1 Mechanical Methods for Residual Stress Introduction

Residual stress introduction by mechanical means on a component rely on the application of external loads that produce localized inelastic deformation. Upon removal of external loading, elastic spring-back occurs that produces both tensile and compressive residual stresses for equilibrium. Fact of forming mechanical type of residual stresses is that is a surface or part yield in tension, during loading; after unloading, the residual surface stress will be in compression, which is desirable. On the other hand, if a surface yields in compression upon loading; after unloading, residual stress will be in tension, which is undesirable [19].

The most widely used mechanical methods for production of beneficial compressive residual stresses are shot peening and surface rolling. Both

methods use local plastic deformation, first of which is by the pressure of the impact of small balls and the second is by the pressure of narrow rollers [19].

Surface rolling is widely used in the production of threads since it is an economical method as a forming operation of bolts and screws in addition to improved fatigue performance obtained by the formation of residual stresses [19]. A 50 percent higher fatigue strength for rolled threads were reported to be obtained by Heywood [21] when compared to cut or ground threads made of high strength steel. Rolling is also a widely used method to produce desired compressive residual stresses in fillets for components such as crankshafts, axles, gear teeth, turbine blades, and between shank and head of bolts [19]. Fillet rolling process is illustrated on Figure 2.14.

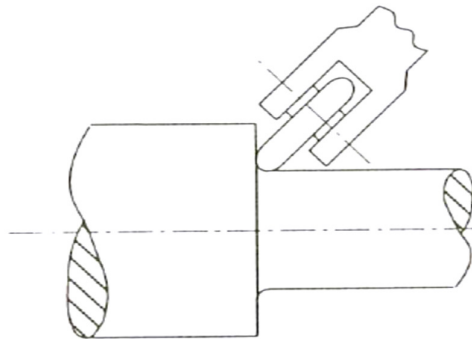


Figure 2.14 Introduction of compressive residual stresses at the fillet radius by localized plastic deformation [19].

2.2 Statistical Considerations in Stress Based Fatigue Limit Studies

Since a variety of factors affect the fatigue life as summarized in the previous section, scatter in data is inevitable in fatigue life testing and evaluation studies. Although some of the factors such as variations arising from test

equipment in addition to specimen alignment, type and mode of loading, frequency and surface preparation of test samples can be controlled; local metallurgical factors can result in considerable amounts of data scatter. Since especially crack initiation is a microstructural phenomenon, variations in local metallurgical factors such as microstructural features and hardness variations will be effective in fatigue life data [19].

This fact lead to the usage of statistical analysis of the fatigue data in order to reliably estimate the fatigue behavior of materials and engineering components and to predict service performance for a given margin of safety. Statistical analysis can also be used for design of experiments such that confounding of sources of variability is avoided and the number tests for a given reliability and confidence level can be determined [19].

2.2.1 Definitions and Quantification of Data Scatter

In statistical analysis of fatigue, the fatigue limit which has a statistical variation is the “stochastic variable” x . The characteristics of such a variable for a population are obtained from a number of small part of the population, called a “sample”. The mean or average for a sample size n is then defined by the equation [19];

$$\bar{x} = \frac{1}{n} \sum_{i=1}^n x_i \quad (2.14)$$

The mean value gives a measure of the average value of the variable, x within the measured values of the defined samples. Another measure of the central value is the median, which is the middle value in an ordered array of the variable x in the sample [15]. The third parameter to define the distribution of the variable of interest is the mode value which describes the most frequent value of the variable, x .

The measure of the magnitude of the variation is defined by standard deviation. Standard deviation is formulated as;

$$S = \sqrt{\frac{1}{n-1} \sum_{i=1}^n (x_i - \bar{x})^2} \quad (2.15)$$

where \bar{x} is the mean value of x [19].

The dimensionless value, coefficient of the variation, is defined by the normalization of S with the mean value as [19];

$$C = \frac{S}{\bar{x}} \quad (2.16)$$

The smaller the standard deviation or the coefficient of variation; the closer the data within the sample range [19].

2.2.2 Probability Distributions

The probability function, $f(x)$ quantatively describes the variation of variable x within the defined range of samples. This function evaluates the probability of the any defined value of x within the range. This function is also called the “probability density function” or the “frequency function”. The probability that the variable x is less than or equal to a particular value in its range of values is given by the “cumulative probability distribution function”. This function usually has a sigmoidal shape. The baseline statistical distributions used in fatigue and durability are the normal, log-normal, and Weibull distributions [19].

2.2.2.1 Normal and Log-Normal Distributions

If variations of the variable x are symmetric with respect to the mean, the distribution is defined as normal. The probability density function $f(x)$ for normal distribution or Gaussian distribution is expressed as [19];

$$f(x) = \frac{1}{S\sqrt{2\pi}} e^{-\frac{1}{2}\left(\frac{x-\bar{x}}{s}\right)^2} \quad (2.17)$$

The normal distribution is defined in terms of the mean value, \bar{x} and standard deviation, S and has a bell shaped curve. A distribution of a set of data are assumed to be normal when the 68,3 % of the data lies within the range $\pm S$ of the mean, 95.5% of the data within mean $\pm 2S$ and 99.7% within mean $\pm 3S$ [19].

The cumulative frequency function for normal distribution is defined as;

$$F(x) = \int f(x) d(x) \quad (2.18)$$

The probability density function and cumulative distribution function are demonstrated on Figure 2.15.a and 2.15.b respectively.

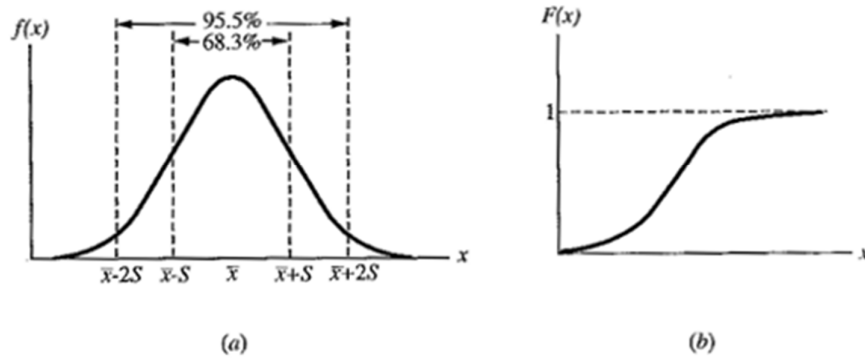


Figure 2.15 Plots of normal distribution (a) Probability density function, (b) Cumulative distribution function [15].

2.2.2.2 Weibull Distributions

Weibull [22] has developed his engineering approach and applied to the fatigue test result analysis [23]. Weibull has developed two- and three-parameter distribution functions, which are often used in preference to the log-normal distribution to analyze probability aspects of fatigue results. The two-parameter Weibull distribution approach assumes that the minimum life, N_{f0} , of a population is zero, while the three-parameter function defines a finite value of minimum life greater than zero [19]. The three-parameter Weibull model is;

$$F(N_f) = 1 - e^{-\left(\frac{N_f - N_{f0}}{\theta - N_{f0}}\right)^b} \quad (2.19)$$

where

$F(N_f)$ = fraction failed in time or cycles, N_f ,

N_{f0} = minimum time or cycles to failure

θ = characteristic life (time or cycles when 63.2% have failed)

b = Weibull slope or shape parameter

In two-parameter function $N_{f0} = 0$ hence

$$F(N_f) = 1 - e^{-\left(\frac{N_f}{\theta}\right)^b} \quad (2.20)$$

The two-parameter approach is widely preferred to be used in fatigue limit analysis when compared to three parameter approach.

It should be noted that fatigue life is preferred as the main consideration in fatigue analysis according to Weibull's approach in most cases whereas fatigue strength is the subject of calculation for the usage of Gaussian's approach. When the fatigue strength is to be studied according to Weibull distribution analysis, the N values in the above equations should be substituted with fatigue strength [19].

The slope, b, describes a measure of the shape of the distribution. Figure 2.16 shows a two-parameter Weibull distribution for different values of b [19].

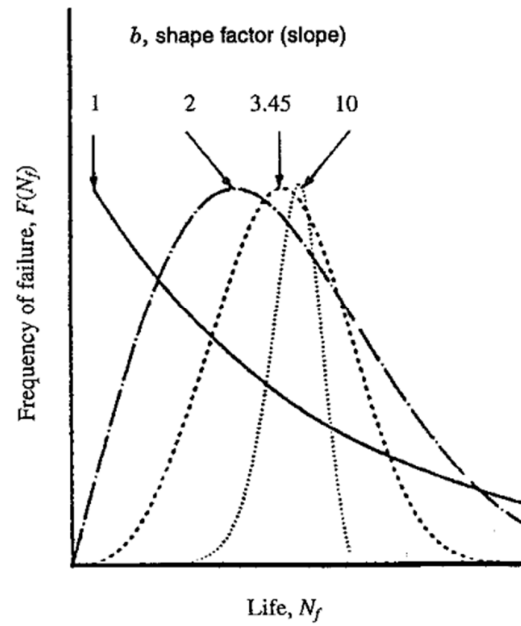


Figure 2.16 Two-parameter Weibull distribution for different values of shape parameters [24].

Weibull distribution approaches to Gaussian distribution when b is between 3.3 and 3.5. The Weibull distribution function is exponential when $b=1$ [19].

2.2.3 Probabilistic Approach to Stress-Based Fatigue Analysis

In stress-based statistical fatigue analysis with S-N curves three fundamental variables are considered; (1) S ; the load level, generally a stress or strain index such as stress amplitude or Smith-Watson-Topper parameter (independent variable), (2) N ; the number test cycles to failure (dependent variable), (3) P ; proportion of failures under the specified number of cycles of run-out (dependent variable) [25, 26].

By the use of these three parameters, P-S-N surface can be constructed by adding the third axis P on the S-N curve as demonstrated on Figure 2.17. The P

axis represents the percentage of specimens which fail at a given stress value and number of cycles. From the P-S-N surface, S-N curve can be traced by fixing a specific value of P, and a family of S-N curves can be drawn for different values of P as shown on Figure 2.18. The centerline of this curve describes the S-N curve with 50% probability with $P=0,5$; which means that 50% of the samples will fail above this curve and 50% below it. With the same logic; the S-N curve with $P=0,3$ can be drawn also which describes the S-N curve above which 30% of the samples will fail and 70% below so long as multiple tests are run at each stress level [25].

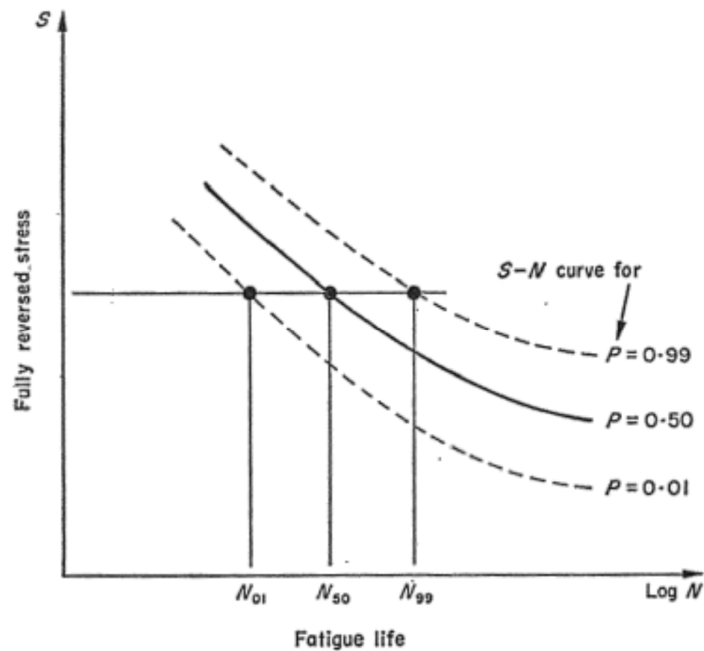


Figure 2.17 Conceptual S-N curves for specified P values [26].

Similarly, a P-S curve can be traced from the P-S-N surface by fixing a value of N (Figure 2.18) or a P-N curve by fixing a value of S (Figure 2.19). The P-S curve is a significant feature in fatigue strength testing as it relates the

proportion of failed specimens to the load level for a specified number of cycles [25].

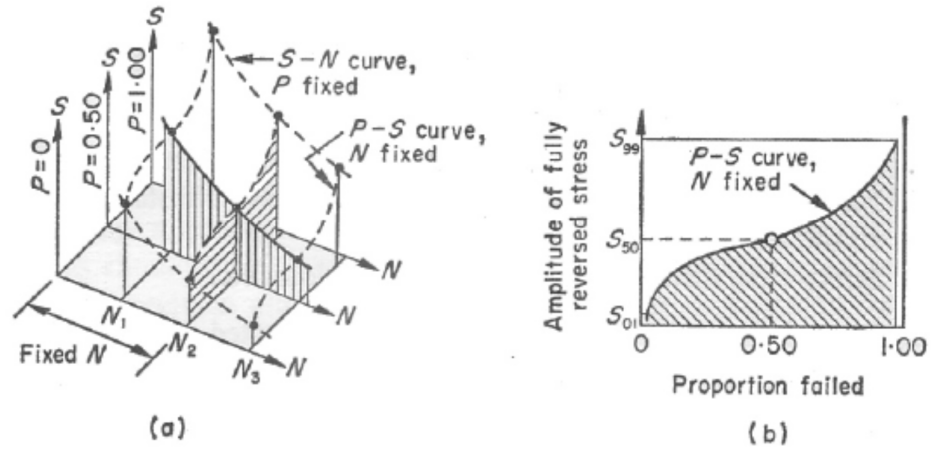


Figure 2.18. P-S-N surface showing P-S trace [26].

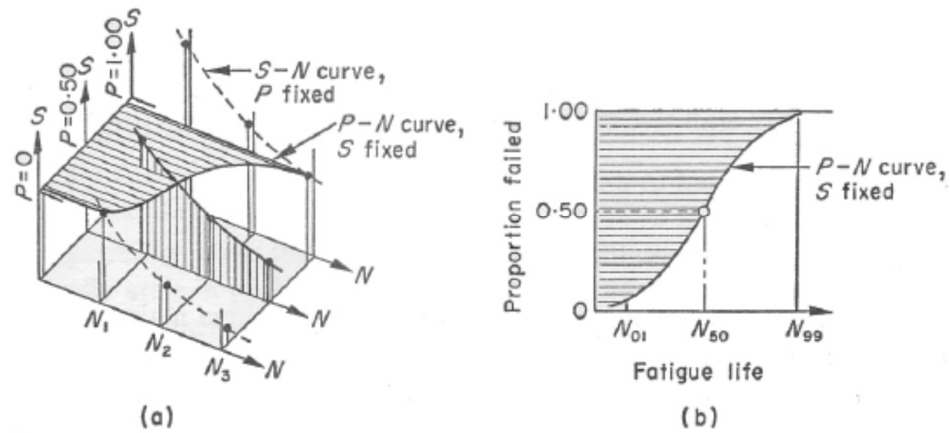


Figure 2.19. P-S-N surface showing P-N trace [26].

2.2.3.1 Regression Analysis of the Fatigue Data

In order to construct a best-fit S-N curve of the obtained fatigue data, regression analysis is needed to be applied. Linear regression with least squares fit is a common used method for fatigue data analysis by the use of which the square of the deviations of the data points from the straight line are minimized [19].

The equation for linear fit for fatigue data can be expressed as;

$$y = a + bx \quad (2.21)$$

where x is the independent variable, y is the dependent variable, a is the y intercept and b is the slope. This type of linear regressions are widely used in fatigue data analysis for the regression of S-N, ϵ -N and da/dN - ΔK curves [19].

For example Basquin's equation

$$S_a = A(N_f)^B \quad (2.22)$$

can be re-expressed for linear regression in logarithmic form as [19],

$$\log N_f = a + b(\log S_a) \quad (2.23)$$

When the data is plotted on a semi-logarithmic scale as S-log(N) curve, linear regression can be applied by least squares method. On the other hand, least squares method is limited in capability of predicting the fatigue limit since it does not treat the run-out data separately and ignores the curvature of the transition of S-N curve around the fatigue limit. From this fact, need for better practices which consider and evaluates the run-out data separately has arisen.

The maximum likelihood method is a widely preferred method in life regression analysis of the fatigue data, which enables censoring the run-out data and application of a conditional probability including both the probability density function and survival function. Maximum likelihood estimation is based on the approach that the best parameter value is the one that makes the observed data most likely. According to this approach, the likelihood is defined to be equal to the probability of the data given (27, 28, 29). In addition, the probability distribution function (PDF) is defined uniquely for each data, whereas least squares approach assumes a normal distribution of data.

To define the likelihood; say a specimen is tested at a stress amplitude of S_a until 10^7 as the pass/fail limit. If the specimen does not fail, according to the defined limit, then fatigue strength of the specimen is higher than S_a . So, for a given PDF, the likelihood of this test is equal to the area on the right side of S_a , as defined on Figure 2.20.a. With the same approach, if the specimen fails, the fatigue strength should be lower than S_a and the likelihood is equal to the area on the left side, as defined on Figure 2.20.b [29].

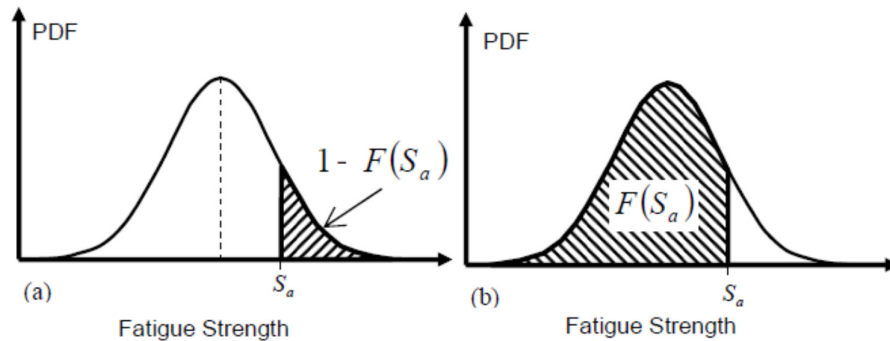


Figure 2.20 Likelihood functions for the staircase test: (a) if the specimen does not fail after the pre-determined number of cycles, and (b) if the specimen fails [29].

To define the fatigue strength variation, maximum likelihood can be defined in terms of cumulative density function $F(S_a^i\{p\})$ as,

$$L = \prod_{i=1}^n F(S_a^i\{p\}) \cdot \prod_{j=1}^m [1 - F(S_a^j\{p\})] \quad (2.24)$$

where n is the number of failed specimens, m is the number of run-outs and $\{p\}$ defines the type of distribution, i.e., normal, log-normal or Weibull [29].

For a given stress amplitude S_a , the likelihood for life-regression models can be described as follows

$$L = \prod_{i=1}^n f(N_F^i\{p\}) \cdot \prod_{j=1}^m [1 - F(N_R^j\{p\})] \quad (2.25)$$

where $f(N_F^i\{p\})$ is the probability density function and $F(N_R^j\{p\})$ is the cumulative density function [29].

The likelihood function can be defined on S-N curve as described in Figure 2.21 for the basis of life regression analysis by MLE method [29].

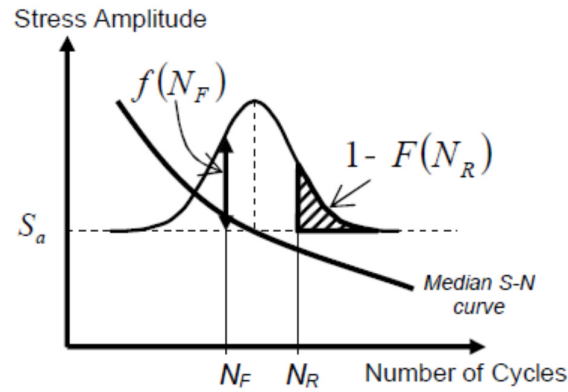


Figure 2.21 Likelihood function definition for life-regression models for failures (N_F) and run-outs (N_R) [29].

2.2.3.2 Advanced Fatigue Test Techniques and Statistical Analysis

Conventional fatigue tests for obtaining S-N curves depends on the objective of determination of number of cycles for failure for a defined range of stress amplitudes. This requires a series of replication tests at defined stress levels, typically a minimum number of 10, to obtain the S-N curve. By conducting a series of tests at defined stress values, a series of S-N curves could be obtained for different probability levels with a range of fatigue life for each stress level [2, 25]. This enables to describe the range in fatigue life using a probability distribution, such as the log-normal distribution used by Sinclair and Dolan [30]. This distribution could then be used to estimate the mean and standard deviation for fatigue life for any stress level within the range of the data [25]. Since the design lives of many engineering components are defined as 10^6 to 10^8 , obtaining the S-N curves require a large number of tests duration of which are measured in terms of years.

In addition to the long durations of tests, another drawback of the conventional fatigue testing is the statistical determination of the transition region prior to

fatigue limit and determination of the fatigue strength is difficult to assess; since statistical analysis by least squares method does not treat the transition region data and the run-out data separately; resulting in difficulty to define a best-fit S-N curve and determine the fatigue limit precisely.

Limitations of conventional fatigue testing and data analysis by least squares method lead to search for better practices for accelerated fatigue testing and statistical analysis of the test data. For this purpose, a large number of studies were conducted to find the best test and analysis practices for fatigue of engineering components [26-42].

As described in the previous section, MLE is an advantageous method to statistically analyze the fatigue data since it treats each data separately defining the likelihoods and gives opportunity to run out data censoring. A large number of researchers used MLE as the method of life regression. Among these, Dixon and Mood [35] described a statistical analysis procedure for the derivation of fatigue limit obtained by staircase testing based on MLE for the assumption of normal distribution of test data. Pascual and Meeker [40] has proposed the Random Fatigue Limit (RFL) modeling which is based on MLE and on the assumption that each specimen has its own fatigue limit based on local microstructural features.

The Stair-Case Test Methodology, Dixon-Mood Analysis and Random Fatigue Limit Model, which are used in the frame of this research study, are described in the following sections in detail.

2.2.3.2.1 Stair-Case Testing Method and Dixon-Mood Analysis

Based on staircase testing method, proposed by Ransom and Mehl [43], the first specimen is tested at a predefined stress amplitude level based on experience. If the specimen fails, stress amplitude level is decreased one step for the next test. If the specimen does not fail, a one step higher stress

amplitude is used for the following test. This procedure is repeated until a valuable number of data is obtained to construct the S-N curve and endurance limit analysis. Figure 2.22 shows an illustration of staircase test history from the work by Little [26].

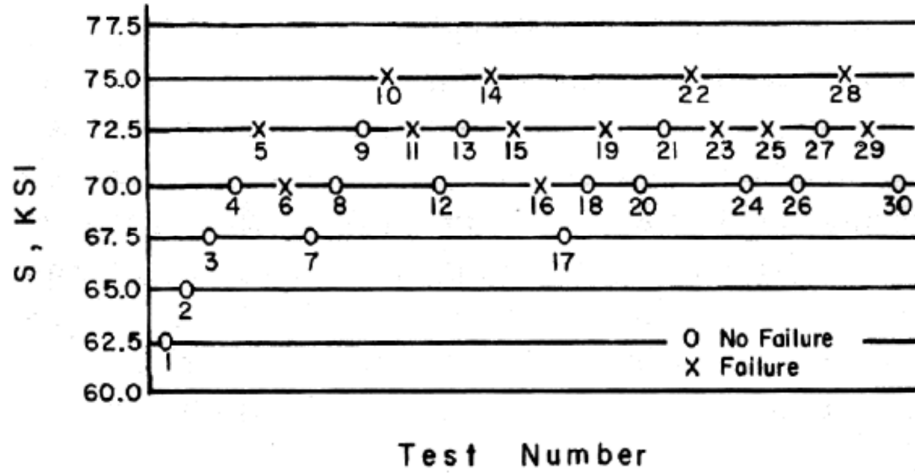


Figure 2.22 Illustration of the staircase test method [26].

Associated with staircase testing, Dixon-Mood [35] analysis is a widely used statistical method to calculate the endurance limit and standard deviation.

Dixon-Mood method based on MLE assumes a normal distribution of fatigue limit to calculate the mean (μ) and standard deviation (σ). The equally spaced stress (S) levels are sorted and numbered starting from the lowest stress level, S_0 . Number for S_0 is denoted by $i=0$. Stress increment or stress step is denoted by S_d . The number of less frequent event at a stress level is defined by n_i . For statistical analysis, three parameters, A, B and C, are calculated where;

$$A = \sum_{i=0}^{i_{max}} n_i \quad (2.26)$$

$$B = \sum_{i=0}^{i_{max}} i x n_i \quad (2.27)$$

$$C = \sum_{i=0}^{i_{max}} i^2 x n_i \quad (2.28)$$

Mean fatigue limit is calculated by the equation;

$$\mu = S_0 + S_d x \left(\frac{B}{A} \pm 0.5 \right) \quad (2.29)$$

If the more frequent event is failure, the plus sign is used in the above equation and if the more frequent event is survival the negative sign is used.

Standard deviation is calculated by the below formula

$$\sigma = 1.62 x S_d x \left(\frac{A x C - B^2}{A^2} + 0.029 \right) \text{ if } \frac{A x C - B^2}{A^2} \geq 0.3 \quad (2.30)$$

or

$$\sigma = 0.53 x S_d \text{ if } \frac{A x C - B^2}{A^2} < 0.3 \quad (2.31)$$

Standard deviation equations are based on the assumption that stress increment value is on the order of 0.5σ to 2.0σ .

2.2.3.2.2 Random Fatigue Limit Model

The Random Fatigue Limit (RFL) model was proposed by Pascual and Meeker [40]. This proposal is based on the assumption that each specimen has its own fatigue limit and similarly each specimen has its own fatigue life at a stress amplitude above the endurance limit, thus, a fatigue strength distribution exists for each defined number of cycles or a finite life distribution at each stress

level. Depending on this assumption, the RFL method explicitly includes this probabilistic distribution to S-N curves incorporating with MLE.

Figure 2.23 describes the two types of distributions that random fatigue limit model is based on an S-N curve [40]. The horizontal distribution defines the distribution of fatigue life at a specified stress amplitude and the vertical describes fatigue limit at a specified fatigue life.

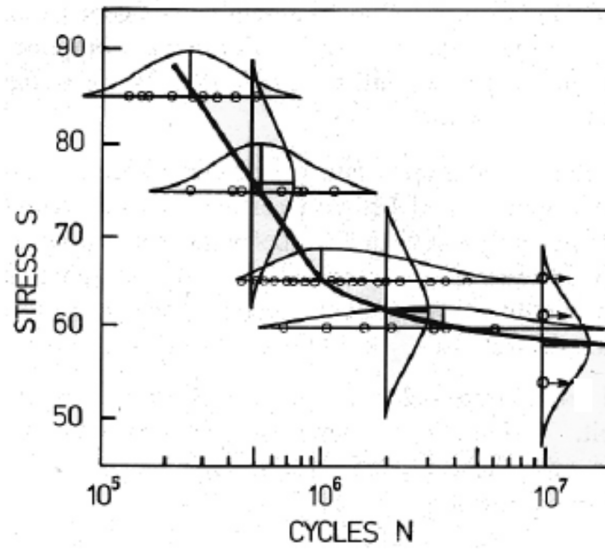


Figure 2.23 Fatigue life and fatigue strength distributions (from Nelson [28]).

The RFL model can be described for a defined stress amplitude level S_a and corresponding fatigue life N_f as

$$\log N_f = \beta_0 + \beta_1 (\log(S_a - \gamma) + \xi) , \quad S_a > \zeta \quad (2.32)$$

where β_0 and β_1 are fatigue curve coefficients, γ is the fatigue limit of the specimen and ζ is the error term [40].

Random fatigue limit method is widely accepted as a procedure with the utilization of manageable mathematical formulation for a better modeling of the S-N curve characteristics. This method accounts for the increase in standard deviation of fatigue life at lower stress levels in addition to the curvature and flattening of the S-N curve in the high cycle fatigue regime. Figure 2.24 describes this flattening effect on the probabilistic S-N curve [25].

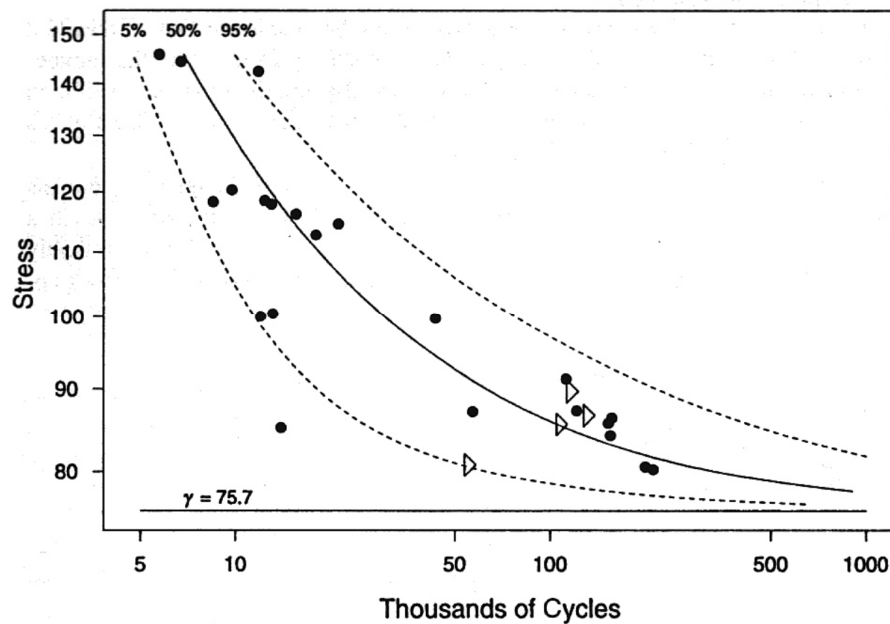


Figure 2.24 Probabilistic *S-N* curves based on random fatigue limit modeling of nickel super-alloy data [44].

In addition to describing a better S-N curve fitting of the data, random fatigue limit approach also provides a better estimate of fatigue limit than conventional S-N analysis; since random fatigue limit method treats fatigue limit as a property specific to each specimen rather than overall property whereas conventional analysis assumes a single-valued constant fatigue limit for all

specimens and thus result in an estimate of fatigue limit below the lowest stress tested, thus producing an unrealistically low value [25].

2.3 State of the Art

2.3.1 Internal Combustion Engine Crankshafts

2.3.1.1 Function of Crankshafts in Internal Combustion Engines

Crankshaft is one of the main components of an internal combustion engine. A crankshaft converts the reciprocating displacement of the piston into regular rotational motion. Crankshaft is composed of main and pin journals linked by webs. Main journals support the crankshaft in the engine block whereas pin journals support the connecting rods. They are located on the crankshaft at cylinder spacing and at half stroke by the webs [45]. Figure 2.25.a represents schematically the piston motion and the crankshaft rotation. Figure 2.25.b describes the main components of a crankshaft.

Diameter, length and fillet radius are the dimensions, which define the main and pin journals. Another function of the journals is the longitudinal guidance. One of the main journals has thrust walls, which locate the crankshaft in the engine block and all pin journals usually have side walls for guiding connecting rods [45].

Webs are usually oval in shape, described by height and width. Counterweights may also be associated with to balance the crankshaft and to reduce its bending distortion. For lubrication purposes, oil holes are drilled into the journals. Oil is usually routed through the web from mains to pins [45].

Front and rear ends forms links of the crankshaft to other parts of the engine. The front end usually supports the gear for the timing mechanism, pulley and vibration damper and the rear end is the link between the crankshaft and the

flywheel. The main dimensions of the crankshaft are calculated depending on the characteristics of the engine and its components during design stage [45].

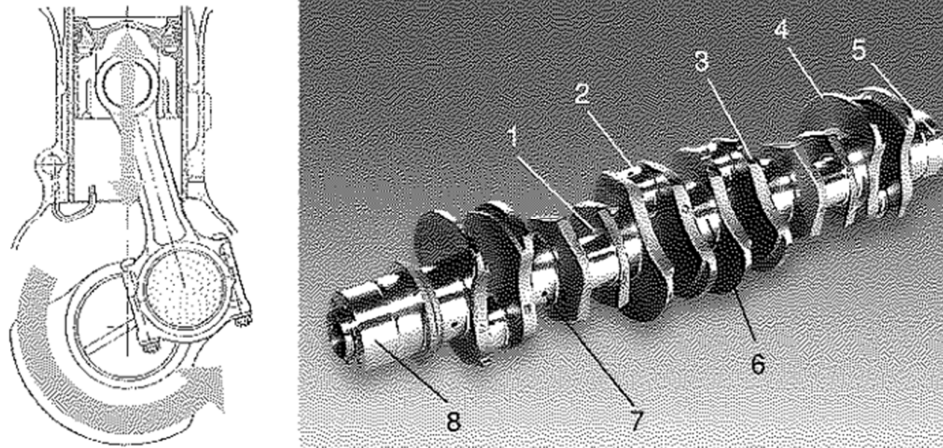


Figure 2.25 (a) Schematic view of an engine illustrating the crankshaft rotation and piston motion (b) Schematic view of a crankshaft showing the main parts; 1-Side walls, 2-Pin journal, 3-Web, 4-Counterweight, 5- Rear end, 6- Main journal, 7- Oil hole, 8-Front end [45].

2.3.1.2 Forces Acting on the Crankshaft

In order to evaluate the forces acting on the crankshaft, the cranktrain system must be considered. Cranktrain system consists of piston, connecting rod and crankshaft. The forces acting on the pin journals are as follows [45];

- (i) Inertia forces due to rotating masses, caused by rotational motion: pin, web, connecting rod big end
- (ii) Inertia forces due to reciprocating masses, caused by translation motion: piston, connecting rod small end
- (iii) Explosion forces due to gas explosion

Figure 2.26 illustrates the forces acting on a crankshaft with crankshaft angle.

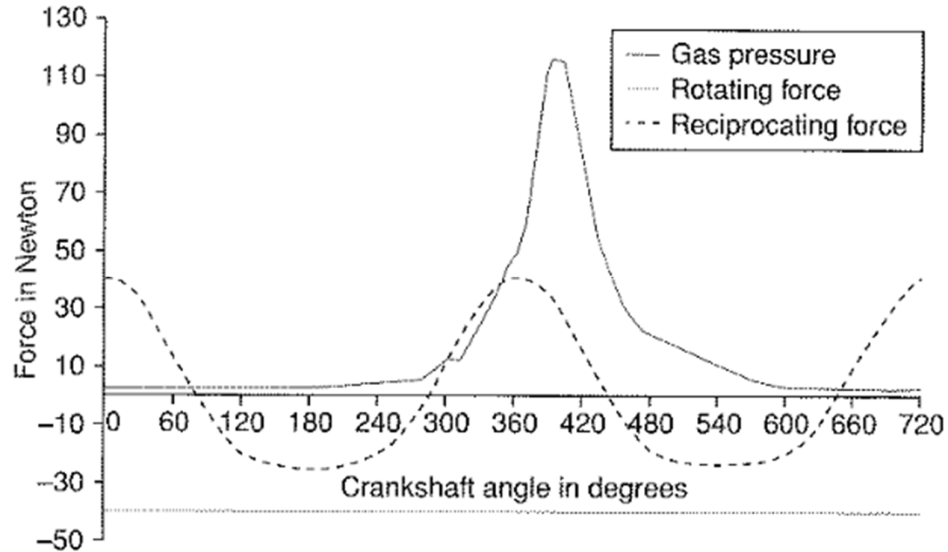


Figure 2.26 Forces acting on crankshaft versus crank angular position [31].

A crankshaft is mainly subjected to bending and torsional stresses. Explosion and inertia forces create cycling bending stresses on the crankshaft. Transmission of the engine torque and torsional vibrations create torsional stresses and their variation with time create cyclic stresses on the crankshaft during its service life. The combination of bending and torsional stresses and their variation with time create fatigue stresses acting on the crankshaft throughout its service life. Thus, crankshaft durability against bending and torsional cyclic loads with required fatigue resistance forms the basis of crankshaft design objectives [45].

2.3.1.3 Crankshaft Materials

Forged steel and cast iron are the two major materials mainly used in crankshaft production due to the high strength, high toughness and

hardenability opportunities they provide. Austempered nodular cast iron has also application in crankshaft manufacturing which is limited due to post-process requirements [45,46, 47].

2.3.1.3.1 Forged Steel

Micro-alloyed steels are widely used in crankshaft applications such as 38MnS6 or 38MnVS6. Unalloyed steels such as SAE1046 or SAE1548 are also used in crankshaft production. For more severe loading conditions, alloyed steels with heat treatment are preferred. Steels, containing Chromium, Molybdenum and Nickel as the major alloying elements, such as 42CrMo4 or 34CrNiMo6 can be shown as examples whose tensile strengths vary between 800 to 1200MPa [45].

Crankshaft manufacturing by forging is conducted by closed die hot forging process with or without subsequent heat treatment depending on the application requirements and material used. Forging process is applied in terms of 5 main steps with the order; rolling, preforming, finishing, clipping and calibration. Process begins with a steel billet produced by continuous casting process. At each step, different corresponding forging dies are used. Figure 2.27 shows the steps and dies of a four-cylinder automobile crankshaft [45].

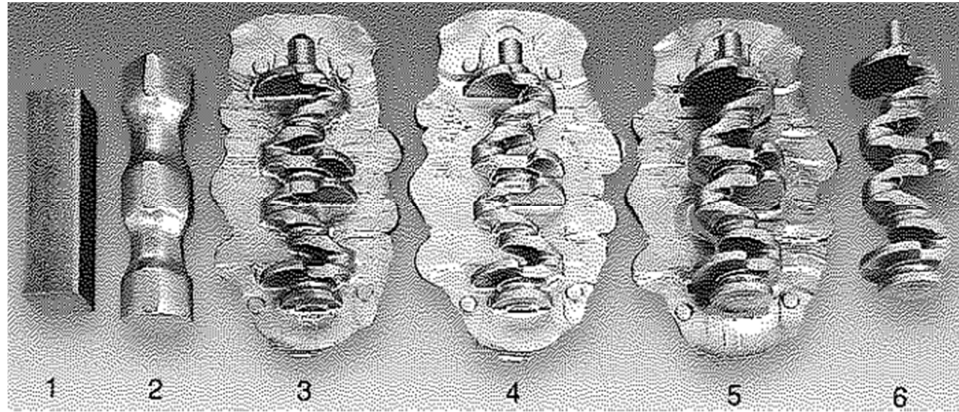


Figure 2.27 Forming steps of a four-cylinder automobile crankshaft; 1-Billet, 2- Rolling, 3-Preforming, 4-Finishing, 5-Clipping, 6-Calibration [45].

Five and six cylinder crankshafts, whose pin positions are not at 0° and 180° , but at a pitch of, for example, 120° , require an additional step in processing. These type of crankshafts are forged in the same way with four cylinder crankshafts and then turned through 60° (for six cylinder crankshafts) at the main journals. This process is called twisting [45].

Depending on the final material requirements heat treatment process, which is quenching and tempering, is selectively applied after forging process. Recent developments in micro-alloy steel industry have led to the use of crankshafts which do not require heat treatment. Controlled cooling is applied to these types of products after forging process [45].

Figure 2.28 shows schematically the layout of forging line for crankshaft manufacturing.

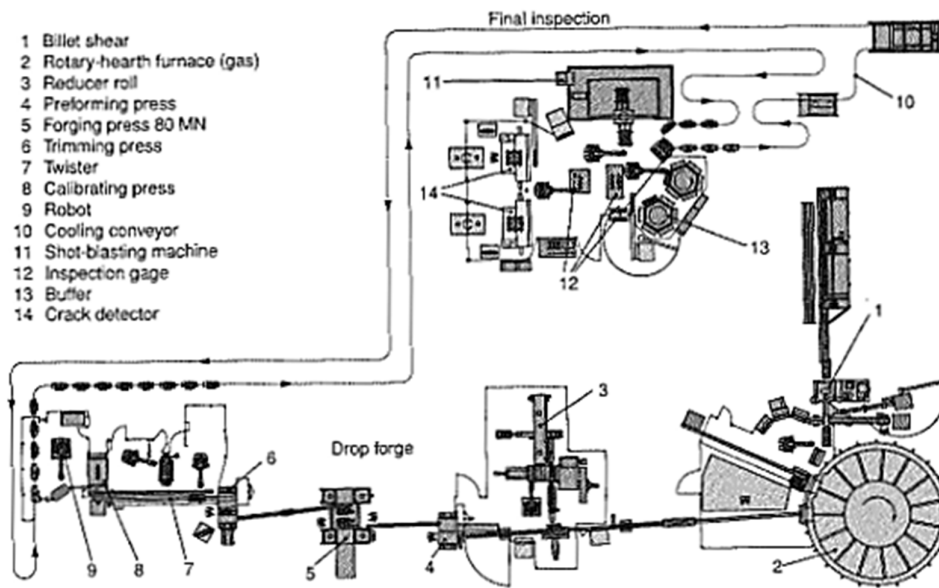


Figure 2.28 Layout of a forging line for crankshaft manufacturing [45].

2.3.1.3.2 Cast Iron

Nodular cast iron is commonly used for crankshaft production due to its higher strength compared to gray iron. Nodular irons used for crankshafts have higher tensile strength and fatigue resistance and superior bearing qualities than the cast irons containing graphite in flake form. They include the following grades: 600/3, 650/2, 700/2, and 800/2. Nodular cast iron used in crankshaft applications can have tensile strengths up to 750 to 850MPa. Compared to steel, cast iron has a lower Elastic Modulus (i.e. steel: 210Gpa and cast iron: 160-180GPa), which means a lower stiffness leading to higher vibration and noise [45, 46].

Casting is the most economical manufacturing technique in crankshaft manufacturing whereas forging is used when the expected loads on the crankshaft require a higher strength material. Green sand casting or shell mould

casting are common methods used in crankshaft manufacturing. Since the cast iron type used in crankshaft is nodular (or spheroidal) cast iron, casting process requires magnesium treatment. So casting process of crankshafts can be divided into four stages; (i) Metal melting, (ii) Magnesium treatment, (iii) Molding, (iv) Finishing [45].

Shell molding process is increasingly being used in crankshaft industry since castings with near-net shape with a fine surface finish can be produced by this method. In shell molding process, a refractory medium, usually silica sand coated with a resin system, is formed around a heated pattern. Resin changes form from thermoplastic to thermosetting condition by the effect of temperature which ensures that shape is formed and retained without distortion. The thermosetting nature of the resin is the basis of the shell molding process [45].

In shell molding process, two iron patterns each with the profile of half of the crankshaft are heated to a temperature range of 230 to 280°C and then the pattern plate is rotated 180°C to locate with the investment box containing the resin-coated sand. The pattern plate and the investment box are closed and the forming assembly is inverted to allow the sand to be in contact with the pattern for certain period of time. After this investment process, closed assembly is returned to upright position so that the excess sand drops free of the pattern leaving the shell mold on the pattern. The pattern and the shell are then placed into an oven for curing operation. Followingly, the hardened shell is removed from the pattern. The two halves of the shell are then combined by the use of suitable adhesive to form a mold. Figure 2.29 shows a picture of one half of a shell mold with a cast crankshaft inside [45].

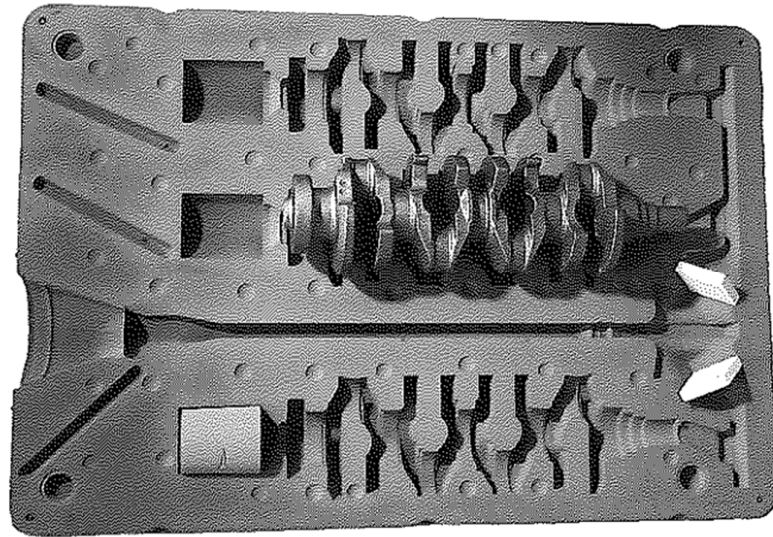


Figure 2.29 Shell mold with crankshaft [45].

After combining, the mold is placed in a box and surrounded with a support medium of iron or steel backing. The backing supports the mold during metal casting to overcome the ferrostatic pressure and supplies high cooling rates [45].

Shell molding process is unique due to its ability to produce castings with fine surface finish, near-net shape and with dimensional tolerances better than most other molding processes [45].

2.3.1.4 Surface Treatment of Crankshafts

In order to improve the crankshaft fatigue resistance to bending and torsional loads and to improve the journal wear resistance, surface treatment is applied to the crankshafts. Surface treatments are usually applied on only fillets and journals with the aim of supplying improved fatigue strength with lower steel costs and industrial conditions for production [45].

Production costs and feasibility due to the geometry of the crankshaft are the main factors in selection of the proper surface treatment in order to achieve an equivalent fatigue resistance. Table 1 summarizes the surface treatments applied to crankshafts, application regions and purpose of applications [45].

Table 2.1 Surface treatments for crankshafts [31].

Purpose of application	Region of Application	Effect	Process
Wear Resistance	Parts in contact (journals, rear end, diameter, collars)	Increase surface hardness	-Nitriding -Induction hardening
Fatigue Resistance in Bending	Pin fillets Main Fillets	Introduce hardness and compressive residual stresses on surface	-Nitriding -Fillet rolling - Induction hardening
Fatigue Resistance in Torsion	Crank Skin	Increase material tensile strength Increase surface hardness on skin	-Use of higher strength steel -Nitriding

2.3.1.4.1 Induction Hardening

Induction hardening is one of the most widely used operations with two main objectives [45];

- (i) Increase wear resistance through the hardening of the bearing journals surface.
- (ii) Improve the fatigue strength, by inducing of residual compressive stresses, especially in the main and pin fillets.

In both cases, objective is to provide a hard martensitic layer on a localized area of the workpiece. Induction hardening is conducted by a three-step process; heating, quenching and tempering [45].

By induction heating the part, temperature is increased above austenitization temperature. During this process, an alternating current is applied to a coil surrounding the workpiece. A time-variable magnetic field with the same frequency as the current in the coil is created and this field induces eddy currents on the part in opposite direction to the coil current. Due to the Joule effect, these currents produce heat in the workpiece and in the coil [45].

Current density decreases from the surface towards the center resulting in a non-uniform temperature profile. Most of the heat is generated in a surface layer called penetration depth. This phenomenon, known as skin effect, allows heating to the desired case depth [45].

During quenching stage, by rapid cooling of the austenized structure, a martensitic layer is obtained. This phase transformation is characterized by a volume expansion, which results in the production of the desired compressive stresses [45].

Quenching process is applied by immersion of the crankshaft in the cooling medium or by spray cooling. Most appropriate media are polymer solutions. Spray quenching is more effective when compared to immersion technique. Flow rate, polymer concentration and temperature are the most important control parameters in quenching [45].

Since martensite is a hard and brittle structure, a tempering process is required subsequently. Reheating the workpiece for tempering is used to reduce the hardness to the required level. It also helps to release some of the residual stresses in order to limit distortion in the subsequent grinding operations. It is usually performed in a furnace in 180 to 300°C temperature range. However since the generating residual compressive stresses is the main purpose of induction hardening, tempering is always a compromise [45].

2.3.1.4.2 Nitriding

Nitriding methods are used in order to improve both wear and fatigue behavior. Nitriding is usually performed on the finished crankshafts by gas, plasma or bath methods. However, due to the process difficulties and cost, this process is used on small volumes only [45].

2.3.1.4.3 Fillet Rolling

Fillet rolling or deep rolling is a method to improve component fatigue strength by generating compressive residual stress layers in the fillets to a depth up to 5mm by the application of local plastic deformation. These compressive stresses oppose tensile stresses which the crankshaft is subjected to during engine operation. As a result, fatigue resistance is increased and notch effect is reduced. Rolling is applied for both cast iron and forged steel crankshafts [45, 48].

Fillet rolling can alternatively be used as an alternative process to fillet induction hardening usage of which is not suitable in some cases such as truck and other larger crankshafts [45].

Usually, undercuts are machined during the rough operation stage, in order to fit the rollers appropriately to the fillet region. During rolling, rolling pressure

is hydraulically applied to the work rollers (Figure 2.30). Increase in roller load from clamping load to full load occurs gradually during two or three crank revolutions. During one revolution, load can be increased in the overlap area and decreased at the pin top area in order to control distortions. Rolling load is selected depending on the material, size of the crankshaft and undercut and strength requirement [45].

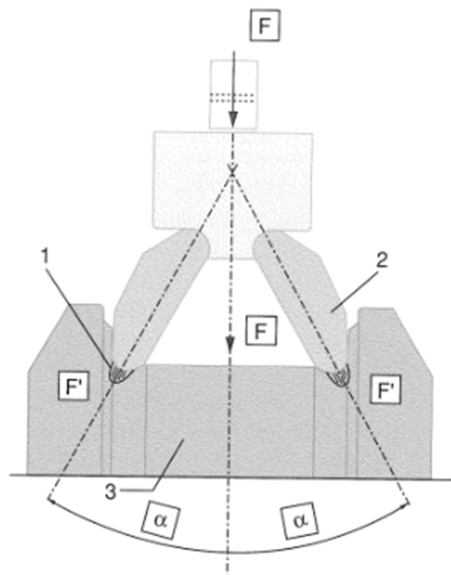


Figure 2.30. Characteristics of deep rolling: 1) Compressive stress in fillet, 2) Rollers 3) Workpiece [45].

After rolling process, a roll-straightening is usually applied in order to minimize the crankshaft run-out by selective introduction of compressive stresses in a predetermined rolling segment. Fatigue strength at the fillet region is not affected by this process [45].

2.3.2 Fillet Rolling Process and Fatigue Strength Improvement

Since crankshaft durability optimization is a significant subject in engine engineering, a number of studies has been conducted based on experimental or analytical approach which deal with testing and evaluation of fatigue performance of crankshafts and fillet rolling process.

The degree of improvement in fatigue strength by fillet rolling depends on process parameters, geometric parameters, and material properties. Process parameters include rolling load, rolling angle, rolling operation loading cycle, etc., while geometric parameters cover crankshaft dimensions, fillet radius and roller geometry [49]. A correlation of rolling load, surface hardness and residual stress distribution with bending moment was proposed by Ko et.al. [50] developed by crankshaft rig test results. Optimum conditions for rolling load, fillet geometry and material were identified by this work. In order to enable an optimization of safety factors, experimental data can be used as input data for CAE analysis. A crankshaft fatigue optimization study was conducted by Cevik et al [51] by bending fatigue testing of steel crankshafts. Effects of material, rolling load, web thickness and undercut radius were analyzed. In-service dynamic simulations were conducted to determine the loads on the fillet region and to calculate the safety factors at these critical regions. In a study by Regul'skii et al [52], fatigue tests of non-hardened crankshafts with fillet and hardened and non-hardened crankshafts without a fillet were conducted. By analyzing of the test results, a procedure of fatigue testing was proposed to obtain the in-service fracture patterns of motorcycle crankshafts.

Component scale testing of the crankshafts to determine the stress versus numbers of cycles (S-N) curves has also been subject of many studies. The possibility of the damage formation on the test rig in case of two-piece failure of the crankshaft has been the starting point of the studies concerning proposal of failure criteria of laboratory tests. Resonance shift failure criterion is one of the widely used methods which is based on the resonance shifts induced by

crack formation and subsequent stiffness drop in resonant bending fatigue rig tests. Feng and Li [53] developed an electrodynamic test machine and an automotive component testing procedure; and proposed the relationship between crack formation, stiffness and resonance shift. Watmough and Malatesa [54] quantified the relationship between crack length and resonance shift. Yu et al [55] developed a finite element procedure to analyze the empirical relationship they proposed. Many researches were conducted on surface failure criterion which is based on the crack initiation. This criterion states that any crack that can be identified visually is accepted as failure [54, 56]. Chien et al [57] worked on the crack arrest phenomenon on the subsurface due to compressive residual stresses by finite element mapping of stress intensity factors against the fillet depth. Following this, Spiteri et al [58] conducted an experimental work to qualify and validate the crack arrest theory proposed by Chien et al [57].

Finite element calculations of residual stresses induced by fillet rolling process has also been subject of a number of researches. Chien et al [58] evaluated the effect of residual stresses at fillet region on fatigue performance of a cast iron crankshaft section under bending by a two dimensional finite element analysis based on nonlinear hardening rule of ABAQUS. Choi and Pan [59] studied on the same subject where analysis was based on the anisotropic hardening rule of Choi and Pan described in a previous work [60]. Çevik et al [61] have calculated the residual stresses induced by fillet rolling of a ductile cast iron crankshaft by Finite Element Method and superposed the calculated values with the dynamic loads on the engine to find out the improvement due to rolling process.

Although, fillet rolling and its effect on fatigue performance of crankshafts has been subject of a number of studies in literature, still there is a significant need for new researches in this area to evaluate the effects of process parameters on fatigue performance of the crankshafts as well as to predicting the in-service fatigue performance by finite element techniques.

CHAPTER 3

EXPERIMENTAL

Experimental part of the study covers the material characterization and bending fatigue tests of the crankshafts from two different materials and fillet rolled at different loads. The subject of this study is a five-cylinder diesel engine crankshaft designed and used for light commercial vehicle applications.

3.1 Main Components of the Crankshaft

Main components of the five cylinder crankshaft used in this study are summarized in Figure 3.1 with the aim of being used as a guide for the features mentioned within the frame of this chapter.

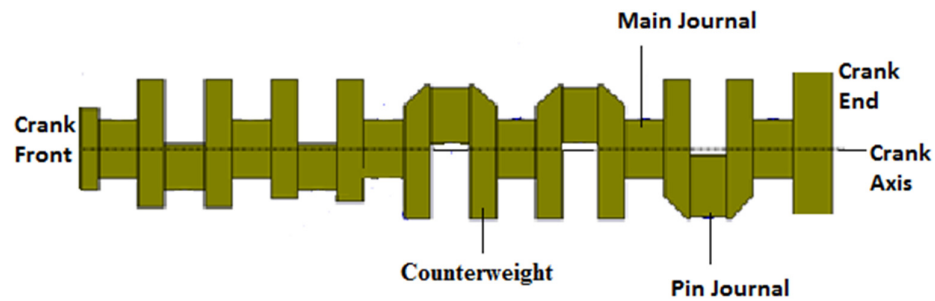


Figure 3.1 Schematic representation of the crankshaft and its main features.

3.2 Material Characterization

3.2.1 Chemical Composition

In this work, crankshafts from two different materials were studied; a ductile cast iron and micro-alloyed forged steel.

Ductile cast iron is grade EN GJS 800-2 [62]. Material is used in as cast condition without any sub-subsequent heat treatment process. Shell casting method was used to produce the crankshafts from this material. Elemental analyses were carried out with the specimens from the ductile cast iron crankshafts and chemical composition is shown on Table 3.1. Results are average of three measurements from different batches of crankshafts.

Table 3.1 Chemical Composition of EN GJS 800-2 ductile cast iron.

Material	Chemical Composition, wt%										
	C	Si	Mn	P	S	Cr	Mg	Al	Cu	Ni	Fe
GJS 800-2	3.89	2.20	0.58	0.01	0.01	0.04	0.03	0.01	0.96	0.04	Rest

Forged steel is a micro-alloyed type and of 38MnVS6 grade. Crankshafts from this material were controllly cooled down after forging process and no sub-subsequent heat treatment is applied after cooling. Spectrometric analysis were carried out with the specimens from the steel crankshafts and chemical composition is shown on Table 3.2. Results are average of three measurements from different batches of crankshafts.

Table 3.2 Chemical Composition of 38MnVS6 Forged Steel.

Material	Chemical Composition, wt%												
	C	Si	Mn	V	P	S	Cr	Mo	Ni	Cu	N	Al	Fe
38MnVS6	0.38	0.56	1.42	0.10	0.01	0.01	0.14	0.02	0.09	0.16	0.01	0.01	Rest

3.2.2 Mechanical Properties

Tensile test specimens from both ductile cast iron and forged crankshafts were prepared from crankshaft end journals and tested by a hydraulic type tensile test machine with a load cell capacity of 400kN. Tensile test specimens were cut from the crankshaft end region. Figure 3.2 shows the test specimen location schematically. Test results were evaluated according to ASTM-E8 [63]. 0.2% off-set yield strength (YS), ultimate tensile strength (UTS) and ductility ($\Delta L\%$) values demonstrated on Table 3.3 are the average of data from testing of 5 specimens, cut from 5 different crankshafts.

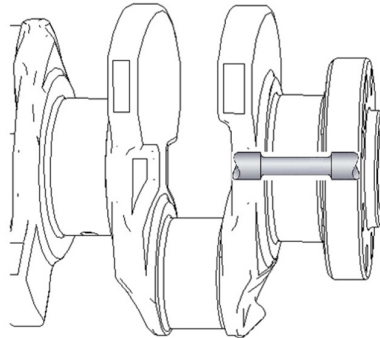


Figure 3.2 Tension test specimen location.

Table 3.3 Mechanical properties of EN GJS 800-2 ductile cast iron and 38MnVS6 forged steel.

Material	Mechanical Properties		
	YS (MPa)	UTS (MPa)	ΔL (%)
GJS 800-2	557	878	3.18
38MnVS6	642	943	11.96

True stress-strain data were also calculated by using the test data and represented on Figures 3.3 and 3.4 for cast iron and steel crankshafts respectively.

Equations 3.1 and 3.2 were used to calculate the true stress-strain data which are valid from the yield point to necking point [1].

$$\sigma_T = \sigma(1 + \epsilon) \quad (3.1)$$

$$\epsilon_T = \sigma(1 + \epsilon) \quad (3.2)$$

where σ_T is true stress, ϵ_T is true strain, σ is engineering stress and ϵ is the engineering strain.

From the onset of necking, true stress and strain values were calculated by using the instantaneously measured length and diameter values during the tests; according to equations 3.3 and 3.4 [1].

$$\sigma_T = \frac{F}{A_i} \quad (3.3)$$

$$\epsilon_T = \ln \frac{l_i}{l_0} \quad (3.4)$$

where F is load on the specimen, A_i is instantaneous cross-sectional area, l_i is instantaneous length, and l_0 is initial gage length.

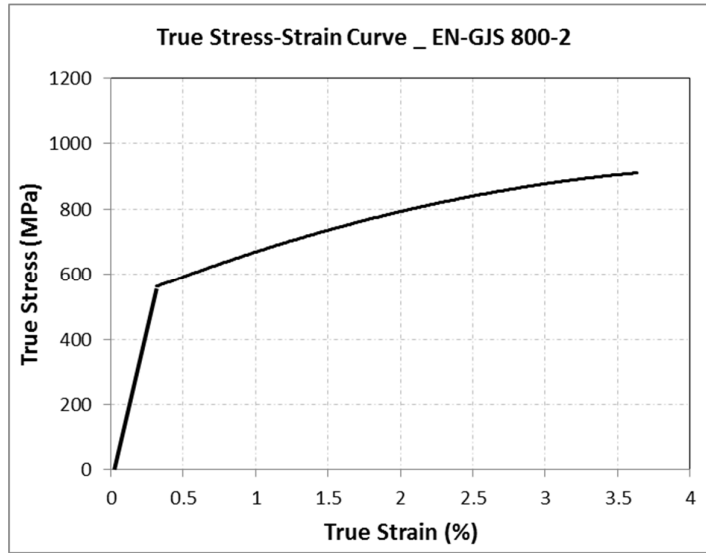


Figure 3.3 True stress-strain curve of EN GJS 800-2 ductile cast iron.

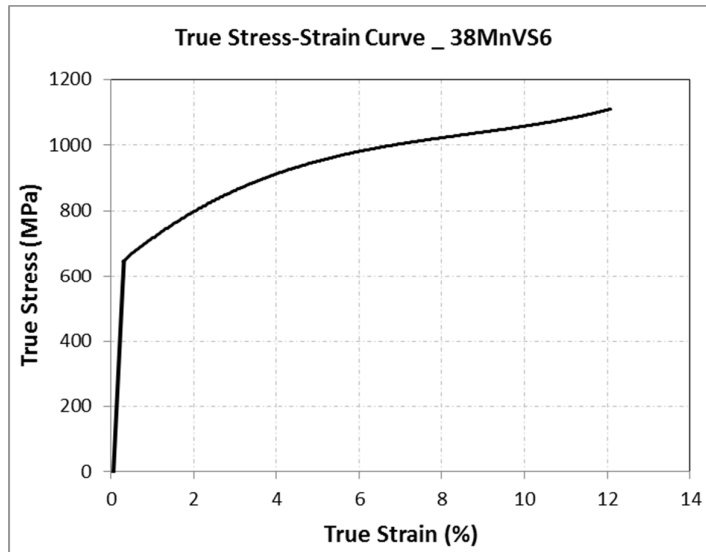


Figure 3.4 True stress-strain curve of 38MnVS6 steel.

Beyond necking point, true stress and strain are related to each other by [1]

$$\sigma_T = K\epsilon_T^n \quad (3.5)$$

where K defines the strength coefficient and n is the strain hardening exponent. The calculated values of K and n for EN-GJS 800-2 and 38MnVS6 from the test data are shown on Table 3.4.

Table 3.4 Strength coefficient and strain hardening exponent values for EN GJS 800-2 ductile cast iron and 38MnVS6 forged steel.

Material	K	n
GJS 800-2	1964	0.27
38MnVS6	1847	0.21

Brinell Hardness tests were carried out with 2.5mm diameter Brinell indenter with a force of 187.5 kgf according to ASTM-E10 [64]. Total 48 hardness measurements for ductile cast iron and 46 for forged steel were conducted through main and pin journal cross-sections, on crankshaft surface and through counterweight cross-sections. Tables 3.5 and 3.6 show statistical summary of the hardness measurements.

Figures 3.5 and 3.6 graphically summarize the hardness profiles for each of the measurement areas for cast iron and steel crankshafts respectively.

Figures 3.7 and 3.8 represent the frequency distribution of the hardness data from crankshafts.

Table 3.5 Hardness profile of ductile cast iron crankshaft.

Material	Hardness			
	Mean (HB)	Mode (HB)	Median (HB)	Standard Deviation (HB)
GJS 800-2	294.5	294	294	7.5

Table 3.6 Hardness profile of steel crankshaft.

Material	Hardness			
	Mean (HB)	Mode (HB)	Median (HB)	Standard Deviation (HB)
38MnVS6	270.9	271	271	7.3

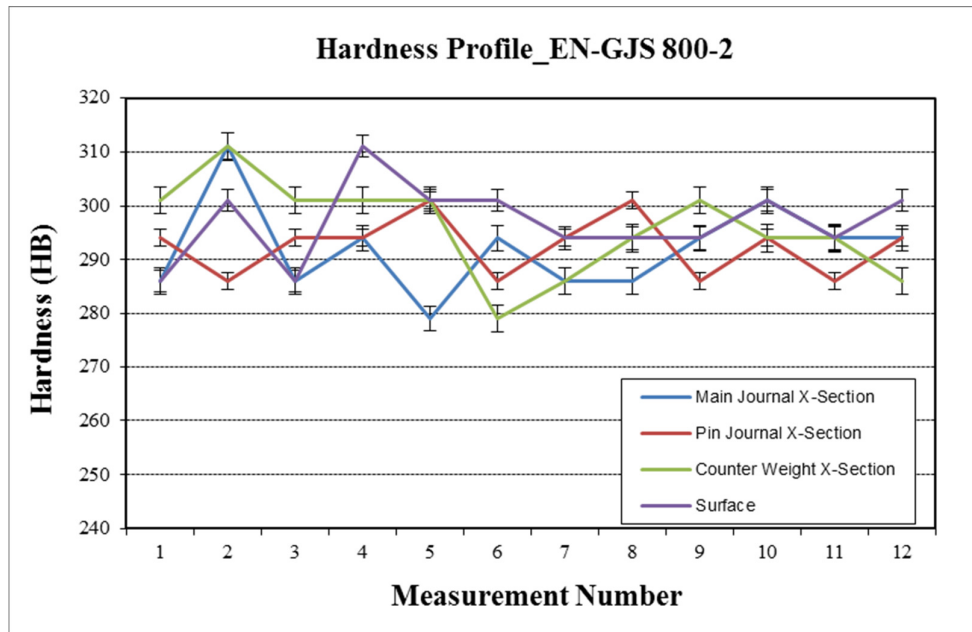


Figure 3.5 Hardness profile of ductile cast iron crankshaft with respect to the measurement areas.

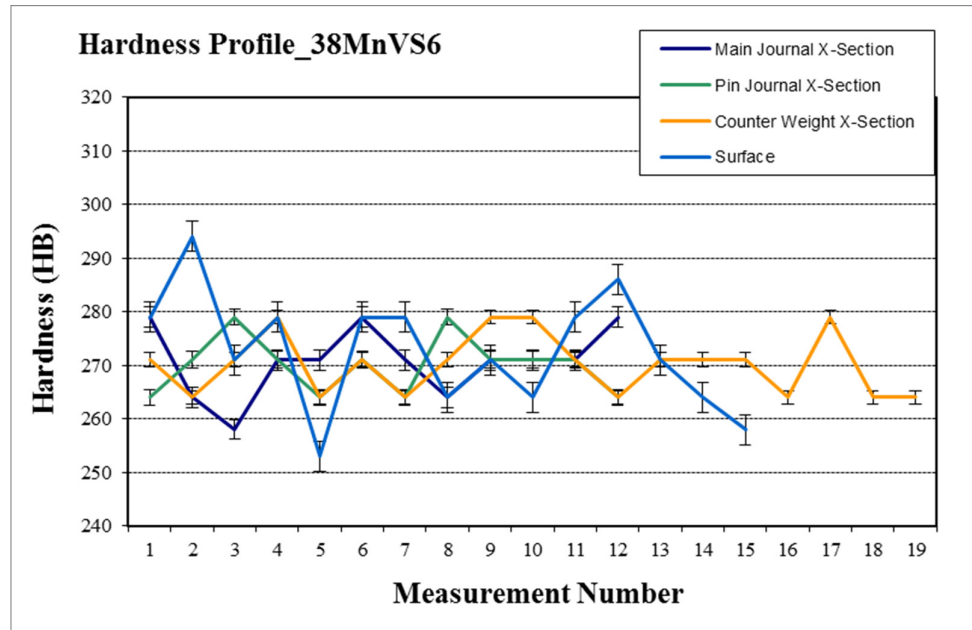


Figure 3.6 Hardness profile of forged steel crankshaft with respect to the measurement areas.

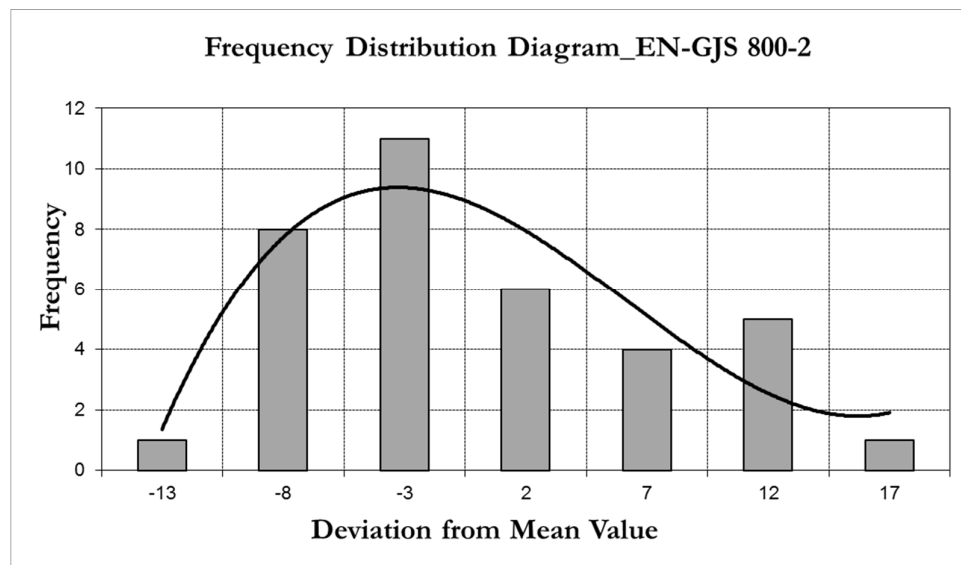


Figure 3.7 Hardness frequency distribution diagram of cast iron crankshaft.

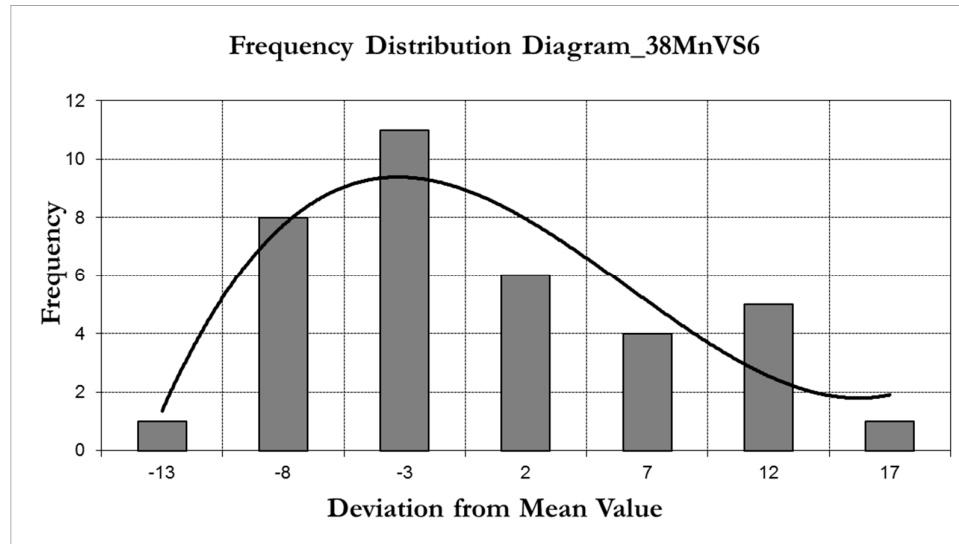


Figure 3.8 Hardness frequency distribution diagram of forged steel crankshaft.

3.2.3 Microstructure

Microstructural characterizations of two types of materials were conducted by optical microscopy. Samples were taken from the pin journals of the crankshafts.

Figure 3.9 shows the microstructure of the EN-GJS 800-2 material, representing the graphite nodules distributed in a pearlite matrix. Figure 3.10 shows a more magnified view of the microstructure.

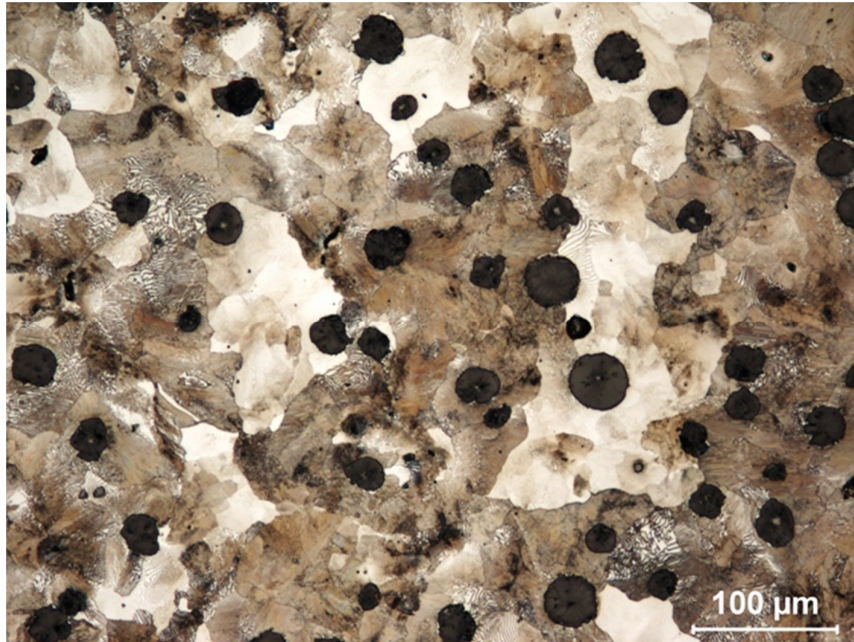


Figure 3.9 Microstructure showing the graphite nodules in pearlite matrix for EN-GJS 800-2 crankshaft material.

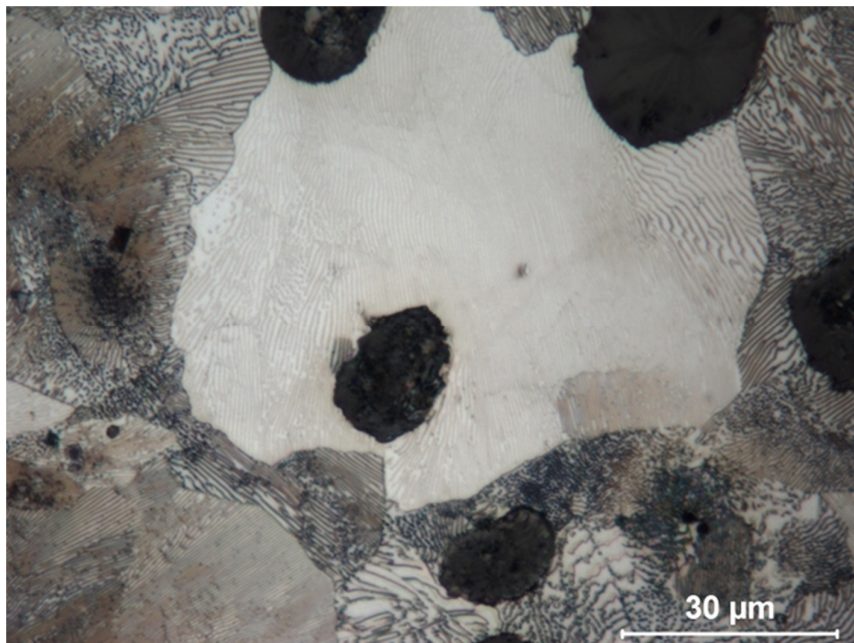


Figure 3.10 Microstructure showing graphite nodules in pearlite matrix.

Figure 3.11 shows the microstructure of the 38MnVS6 steel. Microstructure is mainly composed of pearlite matrix with evenly distributed ferrite grains.

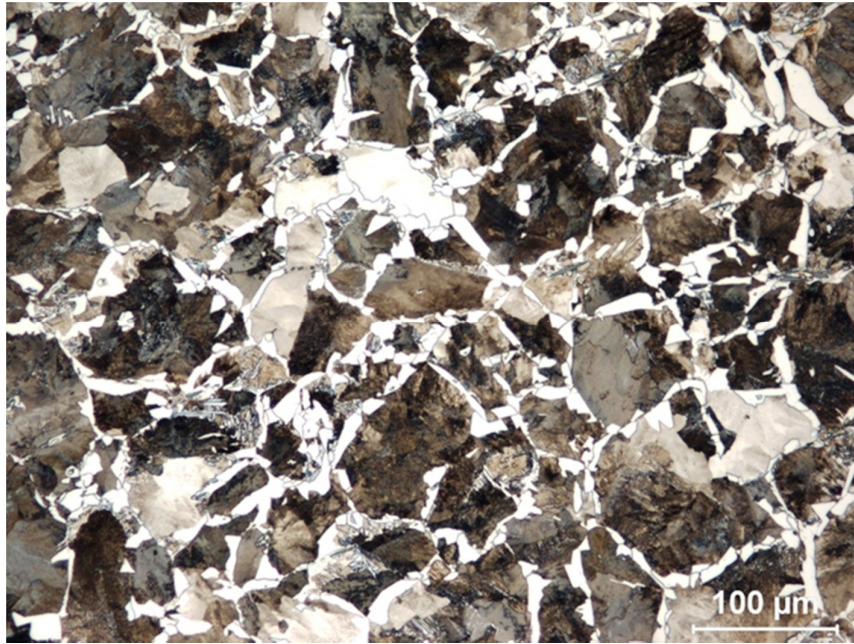


Figure 3.11 Microstructure of 38MnVS6 steel.

3.3 Surface Treatment of Crankshafts

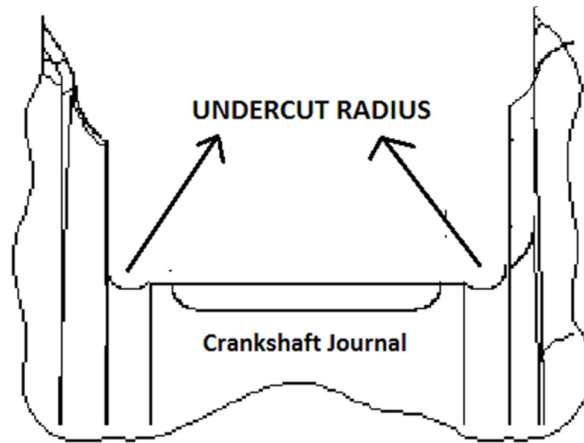
In the frame of crankshaft processing cycles, crankshaft fillet regions are subjected to local hardening process to improve against fatigue damage.

Additionally, induction hardening is applied on the journals of the steel crankshafts.

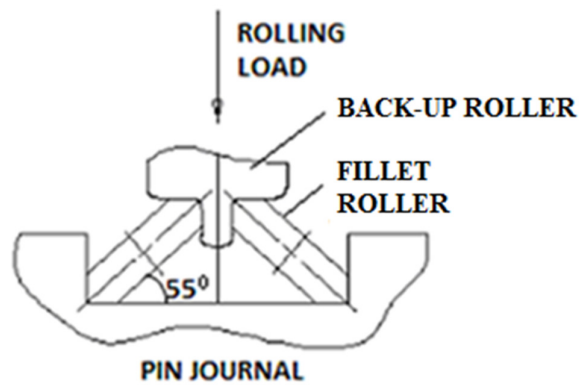
Details of the processes applied on the crankshafts used in this study are described in the following section.

3.3.1 Fillet Rolling Process and Test Matrix

Crankshafts at two types of design conditions were tested in the frame of this work; fillet rolled and non-fillet rolled. During rough operation, an undercut is machined at the journal-cheek corners, which is a common procedure of developing a radius of curvature at these corners to create an area that the roller can fit into. The undercut radius applied in this study is 1.55mm with a machining tolerance of $\pm 0.05\text{mm}$. After machining, fillet rolling is applied to this undercut region hydraulically by the use of a rigid rolling apparatus. Rolling apparatus is composed of a back-up roller associated with two fillet rollers that deform both corners of the crankshaft journal simultaneously during rolling operation. Fillet rollers apply to the crankshaft journal at an angle 55° to crank axis. Figure 3.12 demonstrates the fillet rolled undercut region and rolling operation schematically.



(a) Undercut region



(b) Crankshaft rolling operation

Figure 3.12 Schematic views of the undercut region and rolling operation.

Rolling operation is conducted with a predetermined magnitude of load at a frequency of 80 rpm with 12 crank revolutions on area Y. One-half of the magnitude of load, applied on area Y, is used on area X of pin journals as demonstrated on Figure 3.13. The fillet rollers used in this study are of disc shape with a diameter of 15mm and a thickness of 5mm; and have a 1.45mm radius of curvature at the rolling contact area.

The rolling load values used within the frame of this study describe the magnitudes of loads on the back-up rollers.

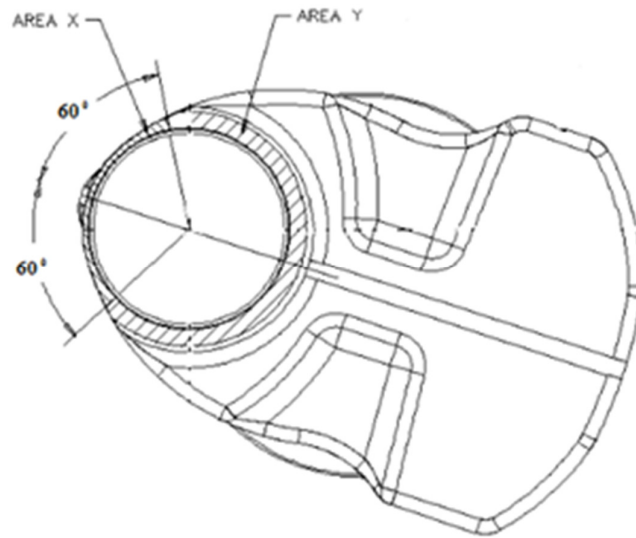


Figure 3.13 Crankshaft pin journal cross-section.

The pin journal rolling process cycle is demonstrated on Figure 3.14 describing the application with respect to crank revolution on areas X and Y. Figure 3.15 shows the loading profile in main journal rolling process.

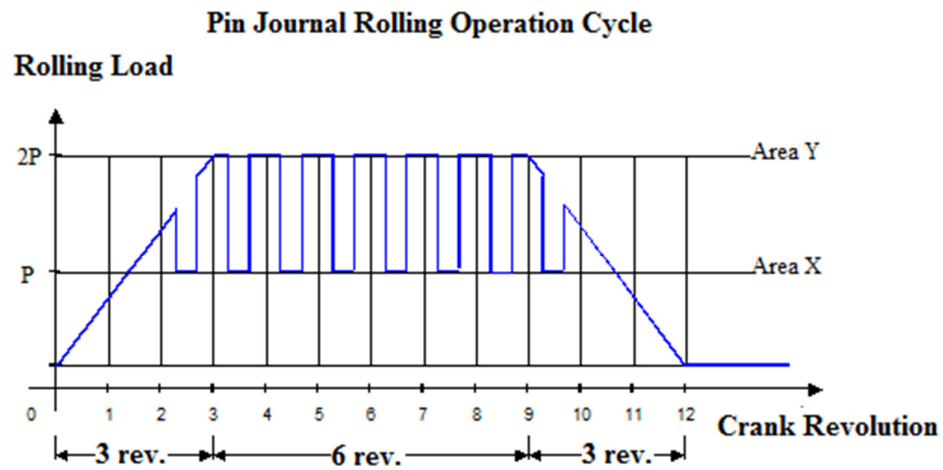


Figure 3.14 Pin journal rolling process cycle.

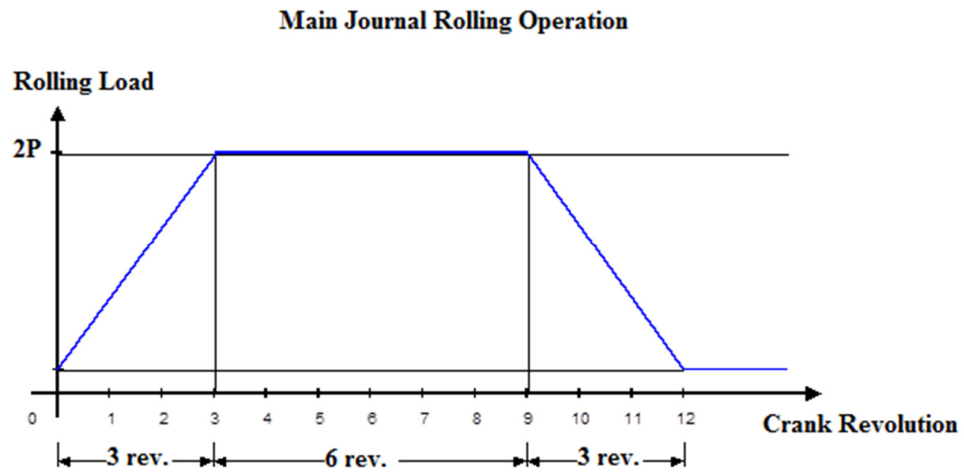


Figure 3.15 Main Journal rolling process cycle.

In the frame of this work, seven design conditions of the crankshafts, in aspects of fillet rolling load, were used. Fillet rolling load conditions are summarized on Table 3.7.

Table 3.7 Crankshaft design conditions.

Material	Rolling Condition				
	Unrolled	Rollel al			
		12.5kN	15kN	20kN	24kN
GJS 800-2	✓		✓		
38MnVS6	✓	✓	✓	✓	✓

3.3.2 Induction Hardening Process

Steel crankshaft journals were also subjected to induction hardening process as a surface improvement process.

Induction hardening was applied on main and pin journals to improve the surface hardness. For this purpose, journal surfaces were heated by induction approximately to 910°C at pin journals and 800°C at main journals for austenization; and followingly quenched to polymer solution at room temperature.

Typical case depths of 1.9mm for pin journals and 1.7mm for main journals were obtained by this process. The fillet region kept un-affected by this process. Hardness obtained by this process on the journals is minimum 50HRc. Figure 3.16 shows the induction hardened region and undercut region.

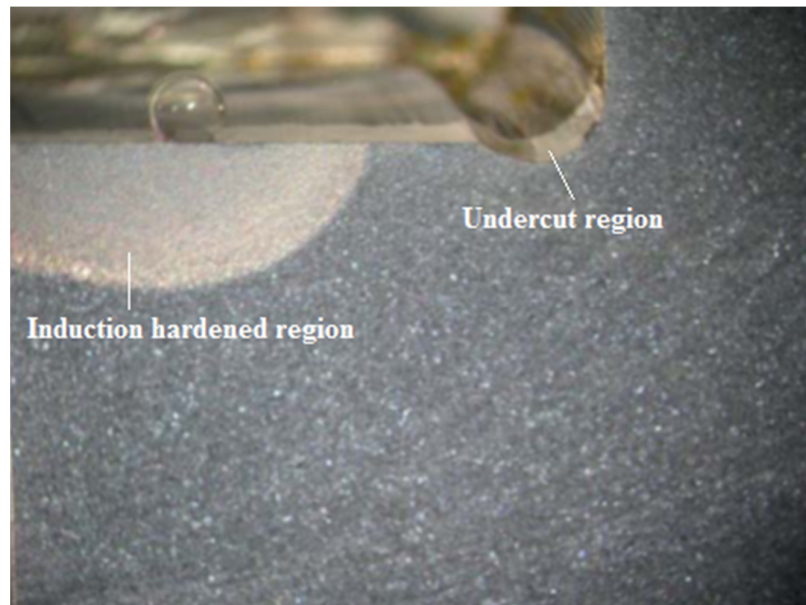


Figure 3.16 Induction hardened area and the undercut region of the steel crankshaft.

3.3.3 Characterization of the Test Specimens

Specimens from the crankshafts from different design conditions were prepared in order to conduct microstructural analysis, undercut depth and radius measurements; and hardness tests to characterize the fillet rolling regions.

3.3.3.1 Undercut Microstructure

Microstructural analysis were carried out on the plastically deformed regions of the crankshafts at area Y. Figures 3.17 to 3.23 show the microstructures at the rolling area of the crankshafts at different rolling conditions.

As depicted from these figures, in ductile cast iron crankshafts no apparent change was observed in pearlite grain sizes and shapes. On the other hand, small changes in graphite morphology was observed near to the surface on the fillet rolled crankshafts. When the undercut microstructures from the crankshafts fillet rolled at different loads are examined, it is easily observed that both pearlite and ferrite grains are elongated perpendicular to the rolling direction and thickness of the grain decreases in the direction of rolling. The change in grain structure increases with the increasing rolling load.

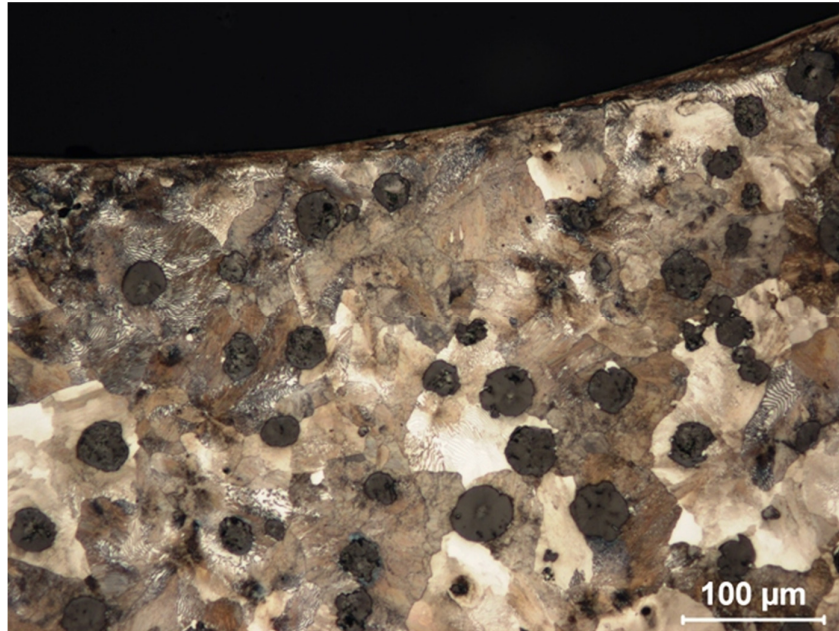


Figure 3.17 Microstructural view from the fillet region of EN GJS 800-2 crankshaft at unrolled condition, 100X.

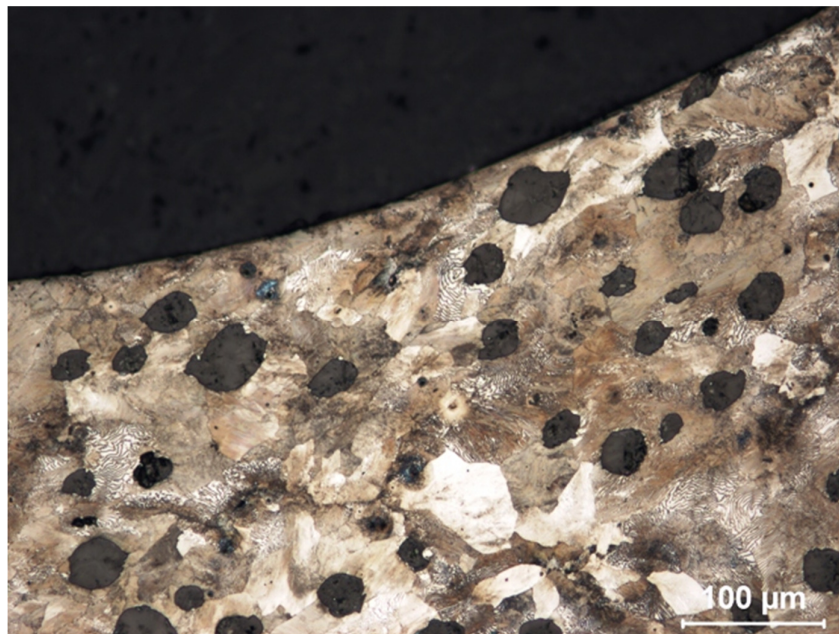


Figure 3.18 Microstructural view from the fillet region of EN GJS 800-2 crankshaft rolled at 15kN, 100X.

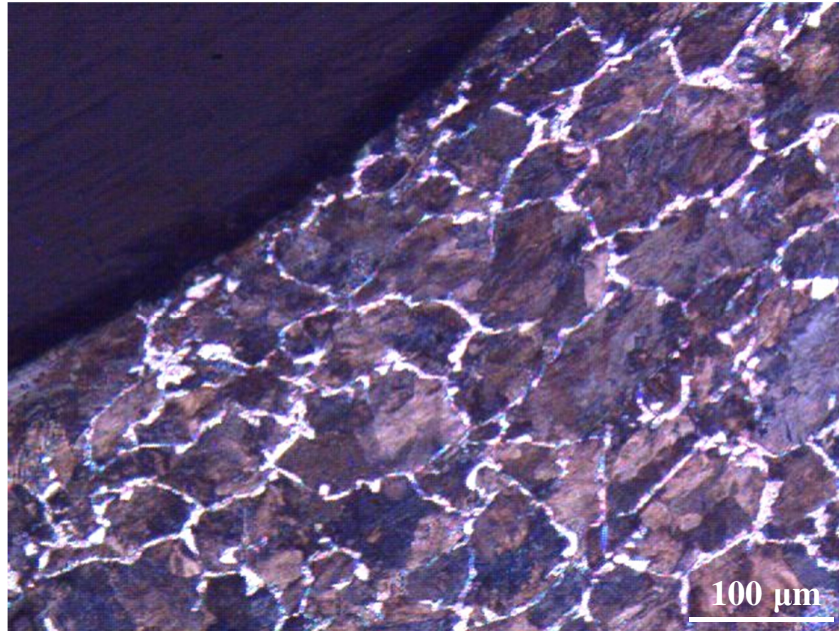


Figure 3.19 Microstructural view from the fillet region of 38MnVS6 crankshaft at unrolled condition, 100X.

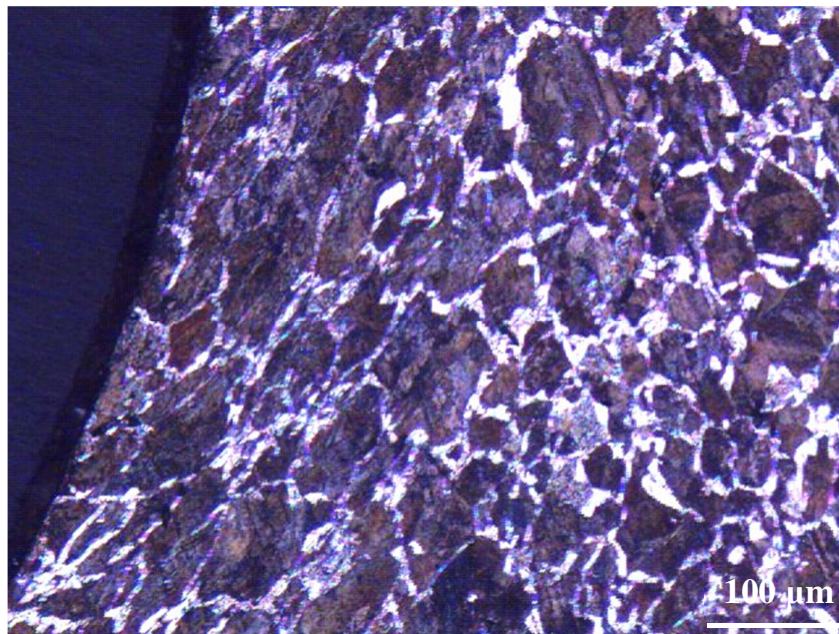


Figure 3.20 Microstructural view from the fillet region of 38MnVS6 crankshaft rolled at 12.5kN, 100X.

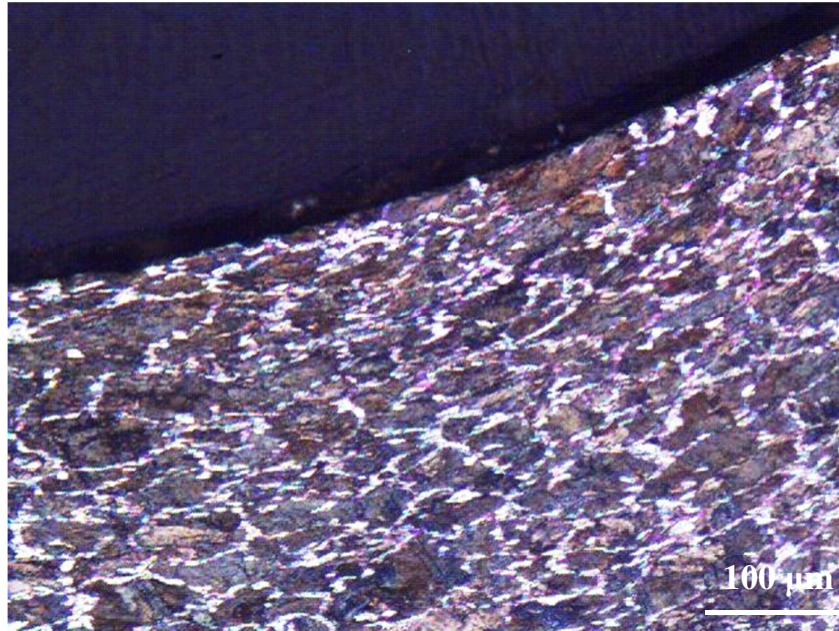


Figure 3.21 Microstructural view from the fillet region of 38MnVS6 crankshaft rolled at 15kN, 100X.

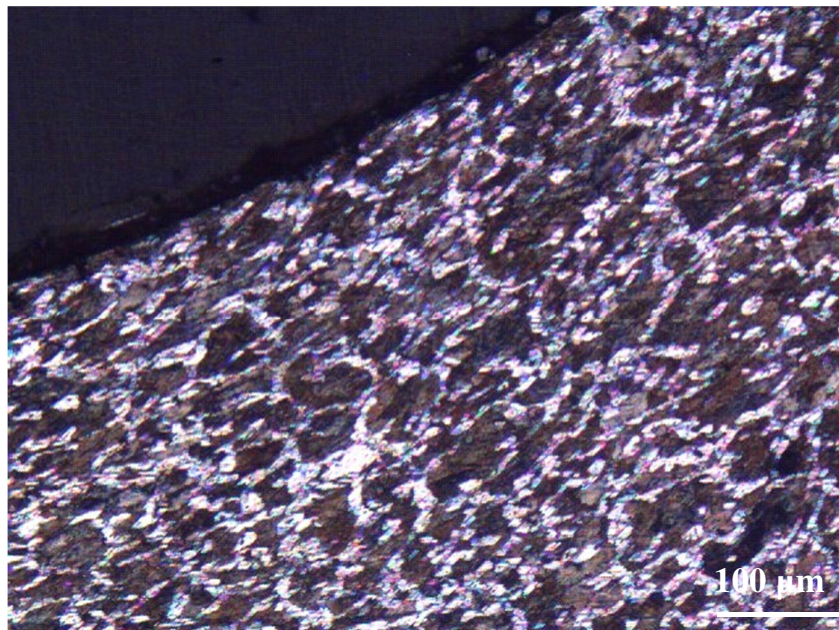


Figure 3.22 Microstructural view from the fillet region of 38MnVS6 crankshaft rolled at 20kN, 100X.

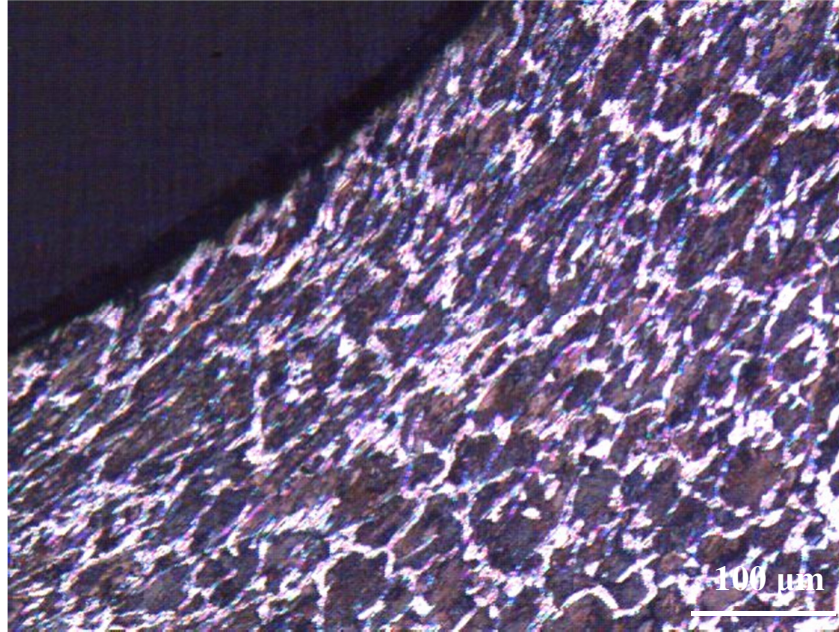


Figure 3.23 Microstructural view from the fillet region of 38MnVS6 crankshaft rolled at 24kN, 100X.

3.3.3.2 Undercut Depth and Radius

Fillet regions of the crankshafts were monitored by the help of Sigmaskop which is a camera utility which can provide 2D projection of the investigated region and measurement of radial and linear dimensions. Figure 3.24 shows the undercut region of a steel crankshaft at unrolled condition for demonstration.

To measure the undercut depth and radius of the specimens, crankshafts were placed under the camera, cranks axis being perpendicular to the optical reading direction of the camera. Three points defining the radius of curvature were marked to define the undercut region; namely radius start and points; and the point at which the depth of the undercut is maximum. By the use of these data, camera software calculates the undercut depth and radius.

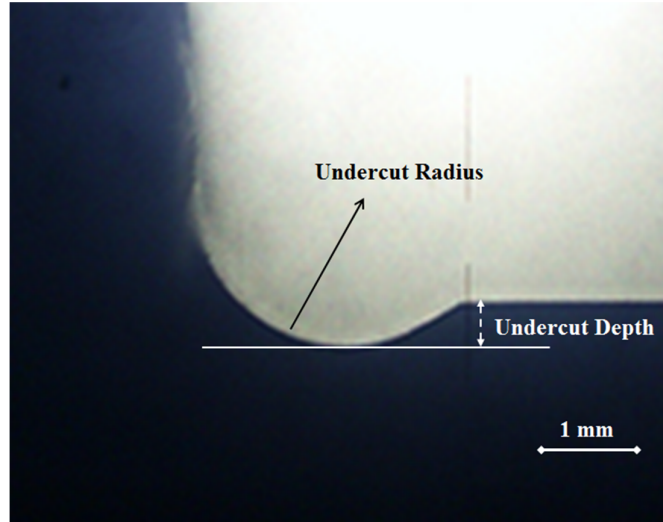


Figure 3.24 Undercut profile of the steel crank at unrolled condition and the measurement locations.

Measured data at each design condition of the crankshaft were tabulated on Tables 3.8 and 3.9. Table 3.10 summarizes the amount of increase in undercut depth and radius in millimeters and percentages.

Table 3.8 Undercut depth and radius measurements at different rolling load conditions for EN-GJS 800-2 crankshafts.

Rolling Load (kN)	Undercut Depth (mm)	Undercut Radius (mm)
0	0.417	1.465
0	0.401	1.462
15	0.472	1.518
15	0.457	1.525

Table 3.9 Undercut depth and radius measurements at different rolling load conditions for 38MnVS6 crankshafts.

Rolling Load (kN)	Undercut Depth (mm)	Undercut Radius (mm)
0	0.408	1.461
0	0.414	1.454
12.5	0.489	1.531
15	0.522	1.547
20	0.546	1.559
20	0.557	1.554
24	0.554	1.562

Table 3.10 Increase in undercut depth and radius at different rolling conditions for cast iron and steel crankshafts.

Crankshaft Material	Rolling Load (kN)	Increase in Undercut Depth (mm)	Increase in Undercut Depth (%)	Increase in Undercut Radius (mm)	Increase in Undercut Radius (%)
EN-GJS 800-2	15	0.056	13.6	0.058	4.0
38MnVS6	12.5	0.078	19.0	0.073	5.0
38MnVS6	15	0.111	27.0	0.089	6.1
38MnVS6	20	0.141	34.2	0.099	6.8
38MnVS6	24	0.143	34.8	0.105	7.2

3.3.3.3 Undercut Hardness Profile

Increase in hardness at the undercut region was characterized by micro hardness measurements. Due to the large variation of data through the depth, measurements were constrained at the subsurface of the deformed region. For each condition, hardness values were measured at a 0.75mm radial distance

from the rolling surface. Results and amount of increase in hardness were tabulated on Tables 3.11 and 3.12.

Table 3.11 Undercut hardness profiles at different rolling conditions for EN-GJS 800-2 crankshafts.

Hardness (Vickers 0.5)	
Rolling Condition	
Unrolled	Rolled at 15kN
311	352
Increase in Hardness (%)	13

Table 3.12 Undercut hardness profiles at different rolling conditions for 38MnVS6 crankshafts.

Hardness (Vickers 0.5)				
Rolling Condition				
Unrolled	Rolled at 12.5kN	Rolled at 15kN	Rolled at 20kN	Rolled at 24kN
279	324	344	357	362
Increase in Hardness (%)	16	23	28	30

3.4 Resonant Bending Fatigue Tests

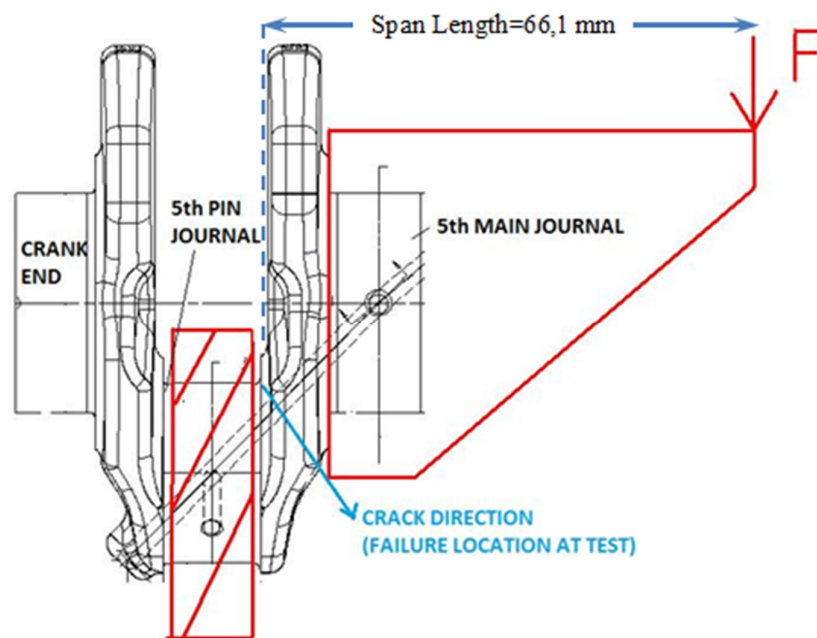
Specimens from crankshafts were cut for fatigue rig tests and tested under cyclic bending conditions on a resonant type fatigue test machine. Cyclic bending moments were applied on the fillet region of 5th pin journal where is the most critical region of the crankshaft under service. Tests were conducted at completely reversed constant amplitude cyclic loads.

The resonant fatigue testing method is based on the mechanical stiffness theory. Under testing, the frequency of the test is stabilized at the resonance frequency of the component on the test rig, depending on the material's Elastic Modulus and geometry of the system. With the formation and propagation of a crack on the specimen, the resonant frequency of the test rig decreases with the decreasing cross-section and mechanical stiffness of the system [65].

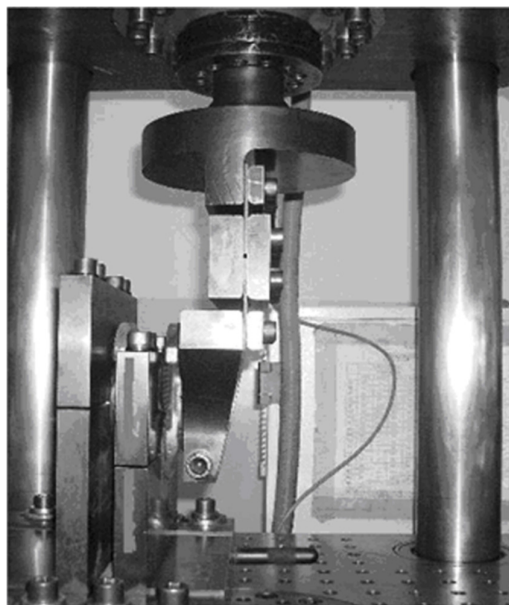
During the tests, the resonance test frequencies for the ductile cast iron and steel specimens were observed to be approximately 35 Hertz and 40 Hertz respectively. In order to cover both crack initiation and propagation stages on the test specimens, a relatively large value of frequency limit of ± 4 Hertz was used as the test failure criterion for both material types.

For the applied bending moments, number of cycles to failure were recorded to construct the stress versus number of cycles to failure (S-N) curves of the crankshafts at rolled and un-rolled conditions. Test run-out criterion was selected as 10 million cycles. Thus, the fatigue strength values used in this study define the fatigue strengths at 10 million cycles.

Predefined bending moments, at a span length of 66.1mm, were applied to the pin fillet region next to main journal side throughout the tests. Figure 3.25 shows the schematic and actual views of the test specimen, test set-up and demonstrates the test failure region.



(a) Schematic view of the test specimen and test set-up



(b) Photograph of the test set-up

Figure 3.25 Schematic and actual views of the test set-up.

Tests were conducted according to staircase test methodology [43]. By the use of this method, first specimen was tested at a predefined moment amplitude level based on experience. If the specimen failed, stress amplitude level was decreased one step for the next test. If the specimen did not fail, a one step higher stress amplitude was used for the following test. This procedure was repeated until a valuable number of data is obtained to construct the S-N curve and endurance limit analysis.

The corresponding stress values for the applied moments of tests were calculated by using the resonant bending test rig simulation model developed by a previous study. Details of calculations will be explained in the frame of next chapter [47].

A stress increment of 8.20MPa was used, around the fatigue limit region, throughout the tests exceptionally, a lower range of 3.28MPa was selected for ductile cast iron crankshafts rolled at 15kN to overcome the variations coming from rolling process and casting process itself.

3.4.1 Resonant Bending Fatigue Test Data

The recorded number of cycles to failure were recorded against applied bending load throughout the tests. The test data were tabulated covering the applied load in kN, corresponding bending moment (Nm), calculated stress value at the critical location of failure (MPa) and the number of cycles to failure/run-out on Tables 3.13 to 3.19 for each test condition. The test data were constructed as stress versus number of cycles on a semi-logarithmic scale and demonstrated on Figures 3.26 to 3.32 for each condition. The total sample size and sample size at the staircase calculation region were also shown on the figures.

Table 3.13 Fatigue test data for EN-GJS 800-2 at unrolled condition.

Load (kN)	Moment (Nm)	Stress (MPa)	No. Of Cycles	Failure/Runout
14.00	925	459	380950	Failure
12.00	793	394	708729	Failure
11.00	727	361	767806	Failure
10.00	661	328	1161583	Failure
9.00	595	295	1755247	Failure
8.75	578	287	1663409	Failure
8.50	562	279	1825051	Failure
8.25	545	271	1879124	Failure
8.00	529	262	2342569	Failure
7.75	512	254	2323952	Failure
7.50	496	246	3258120	Failure
7.25	479	238	2923761	Failure
7.00	463	230	4876599	Failure
6.75	446	221	4013912	Failure
6.50	430	213	6138566	Failure
6.25	413	205	7248912	Failure
6.25	413	205	7986574	Failure
6.00	397	197	9284522	Failure
6.00	397	197	6383463	Failure
6.00	397	197	7329531	Failure
6.00	397	197	10000000	Runout
5.75	380	189	10000000	Runout
5.75	380	189	10000000	Runout
5.75	380	189	10000000	Runout

Table 3.14 Fatigue test data for EN-GJS 800-2 rolled at 15kN fillet rolling load.

Load (kN)	Moment (Nm)	Stress (MPa)	No. Of Cycles	Failure/Runout
26.25	1735	861	178999	Failure
26.00	1719	853	452348	Failure
25.75	1702	845	303371	Failure
25.50	1686	836	817245	Failure
25.35	1676	831	1562301	Failure
25.25	1669	828	1776672	Failure
25.15	1662	825	2327561	Failure
25.05	1656	822	1276038	Failure
24.95	1649	818	2004430	Failure
24.85	1643	815	2247812	Failure
24.85	1643	815	2865356	Failure
24.75	1636	812	3898056	Failure
24.75	1636	812	7747234	Failure
24.75	1636	812	2702067	Failure
24.65	1629	809	5412596	Failure
24.65	1629	809	6226452	Failure
24.65	1629	809	7691208	Failure
24.65	1629	809	3608777	Failure
24.55	1623	805	6524565	Failure
24.75	1636	812	10000000	Runout
24.65	1629	809	10000000	Runout
24.65	1629	809	10000000	Runout
24.55	1623	805	10000000	Runout
24.55	1623	805	10000000	Runout
24.55	1623	805	10000000	Runout
24.45	1616	802	10000000	Runout

Table 3.15 Fatigue test data for 38MnVS6 at unrolled condition.

Load (kN)	Moment (Nm)	Stress (MPa)	No. Of Cycles	Failure/Runout
14.00	925	459	183961	Failure
11.00	727	361	302904	Failure
10.00	661	328	402717	Failure
9.00	595	295	598254	Failure
8.00	529	262	661929	Failure
7.75	512	254	765982	Failure
7.50	496	246	988325	Failure
7.25	479	238	953744	Failure
7.00	463	230	1247135	Failure
6.75	446	221	1183924	Failure
6.50	430	213	2057642	Failure
6.25	413	205	1703622	Failure
6.00	397	197	2174057	Failure
5.75	380	189	2085293	Failure
5.50	364	180	2497189	Failure
5.25	347	172	3498732	Failure
5.00	331	164	5363692	Failure
5.00	331	164	6829251	Failure
5.00	331	164	2893072	Failure
4.75	314	156	7889214	Failure
4.75	314	156	5742918	Failure
4.75	314	156	5236982	Failure
4.50	297	148	10000000	Runout
4.50	297	148	10000000	Runout
4.50	297	148	10000000	Runout
4.75	314	156	10000000	Runout
4.75	314	156	10000000	Runout

Table 3.16 Fatigue test data for 38MnVS6 rolled at 12.5kN fillet rolling load.

Load (kN)	Moment (Nm)	Stress (MPa)	No. Of Cycles	Failure/Runout
26.00	1719	853	138836	Failure
25.50	1686	836	226892	Failure
25.00	1653	820	321569	Failure
24.75	1636	812	426991	Failure
24.50	1619	804	696490	Failure
24.25	1603	795	649811	Failure
24.00	1586	787	799649	Failure
23.75	1570	779	1327665	Failure
23.50	1553	771	2259876	Failure
23.25	1537	763	6646586	Failure
23.00	1520	754	7938242	Failure
23.00	1520	754	8286741	Failure
23.25	1537	763	6228333	Failure
23.00	1520	754	7198820	Failure
23.25	1537	763	8991025	Failure
22.75	1504	746	10000000	Runout
22.75	1504	746	10000000	Runout
23.00	1520	754	10000000	Runout
22.75	1504	746	10000000	Runout
23.00	1520	754	10000000	Runout
23.00	1520	754	10000000	Runout

Table 3.17 Fatigue test data for 38MnVS6 rolled at 15kN fillet rolling load.

Load (kN)	Moment (Nm)	Stress (MPa)	No. Of Cycles	Failure/Runout
27.00	1785	886	266732	Failure
26.50	1752	869	427092	Failure
26.00	1719	853	588655	Failure
25.75	1702	845	956227	Failure
25.50	1686	836	1876541	Failure
25.25	1669	828	1593814	Failure
25.00	1653	820	2566748	Failure
24.75	1636	812	3349874	Failure
24.50	1619	804	6414563	Failure
24.25	1603	795	8453674	Failure
24.25	1603	795	7814908	Failure
24.25	1603	795	6126937	Failure
24.50	1619	804	5345712	Failure
24.25	1603	795	10000000	Runout
24.00	1586	787	10000000	Runout
24.00	1586	787	10000000	Runout
24.00	1586	787	10000000	Runout
24.25	1603	795	10000000	Runout

Table 3.18 Fatigue test data for 38MnVS6 rolled at 20kN fillet rolling load.

Load (kN)	Moment (Nm)	Stress (MPa)	No. Of Cycles	Failure/Runout
29.00	1917	951	284029	Failure
28.50	1884	935	235499	Failure
28.00	1851	918	281817	Failure
27.75	1834	910	1193748	Failure
27.50	1818	902	991777	Failure
27.25	1801	894	1268021	Failure
27.00	1785	886	297409	Failure
26.75	1768	877	1304825	Failure
26.50	1752	869	680183	Failure
26.25	1735	861	3189461	Failure
26.00	1719	853	2943785	Failure
25.75	1702	845	5123542	Failure
25.50	1686	836	7562199	Failure
25.50	1686	836	8683264	Failure
25.25	1669	828	6895255	Failure
25.50	1686	836	6954123	Failure
25.25	1669	828	8654785	Failure
25.25	1669	828	7956323	Failure
25.25	1669	828	10000000	Runout
25.25	1669	828	10000000	Runout
25.00	1653	820	10000000	Runout
25.00	1653	820	10000000	Runout

Table 3.19 Fatigue test data for 38MnVS6 rolled at 24kN fillet rolling load.

Load (kN)	Moment (Nm)	Stress (MPa)	No. Of Cycles	Failure/Runout
29.00	1917	951	232842	Failure
28.50	1884	935	202149	Failure
28.00	1851	918	208015	Failure
27.50	1818	902	508198	Failure
27.00	1785	886	266732	Failure
26.75	1768	877	847923	Failure
26.50	1752	869	427092	Failure
26.25	1735	861	998198	Failure
26.00	1719	853	2526836	Failure
25.75	1702	845	1246304	Failure
25.50	1686	836	3155752	Failure
25.25	1669	828	5958937	Failure
25.25	1669	828	6126782	Failure
25.25	1669	828	5532145	Failure
25.00	1653	820	7856533	Failure
25.00	1653	820	8956583	Failure
25.00	1653	820	6458213	Failure
25.00	1653	820	10000000	Runout
25.00	1653	820	10000000	Runout
24.75	1636	812	10000000	Runout
24.75	1636	812	10000000	Runout

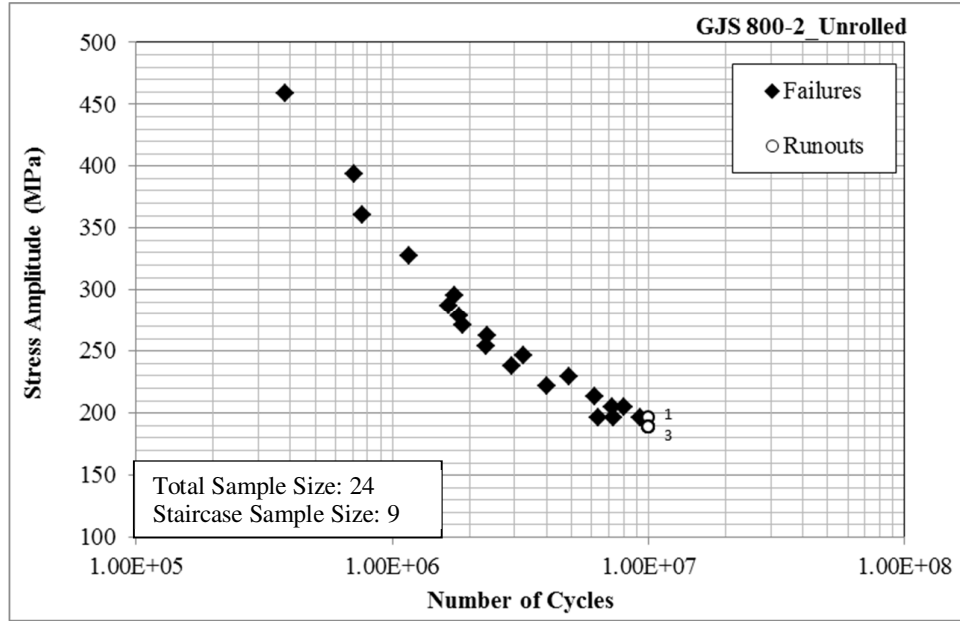


Figure 3.26 S-N curve for EN-GJS 800-2 at unrolled condition.

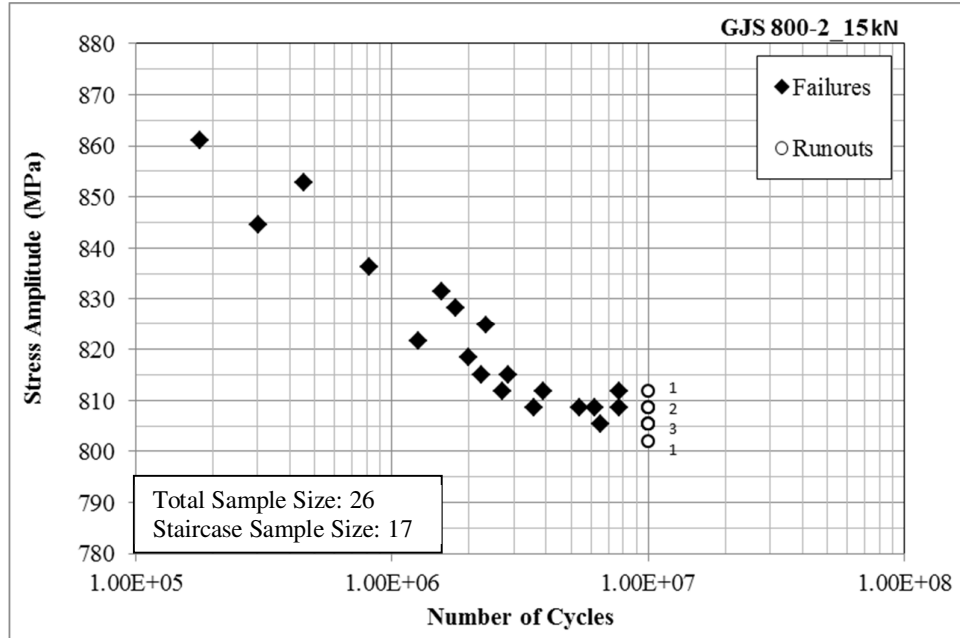


Figure 3.27 S-N curve for EN-GJS 800-2 rolled at 15kN fillet rolling load.

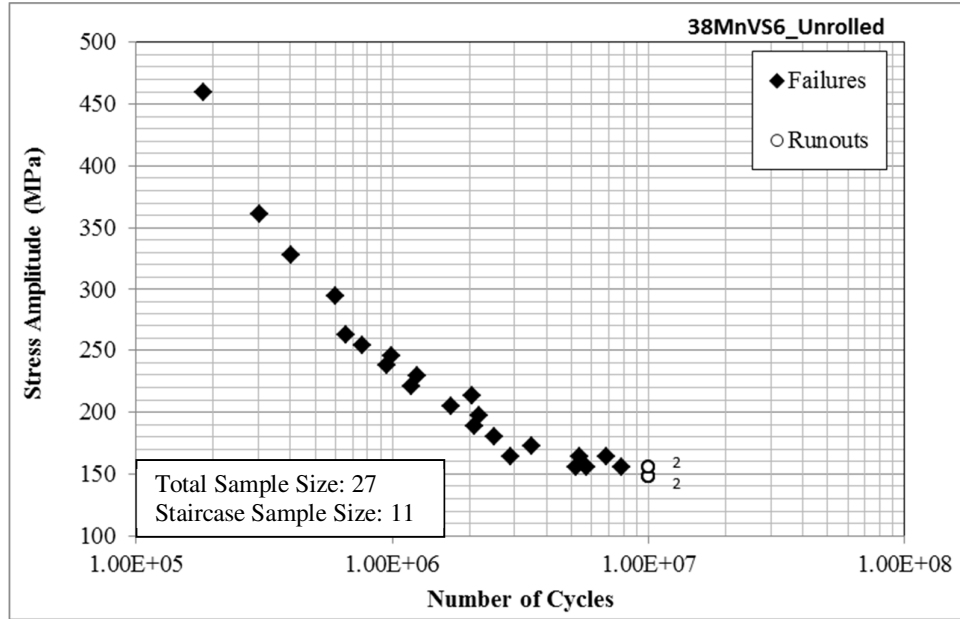


Figure 3.28 S-N curve for 38MnVS6 at unrolled condition.

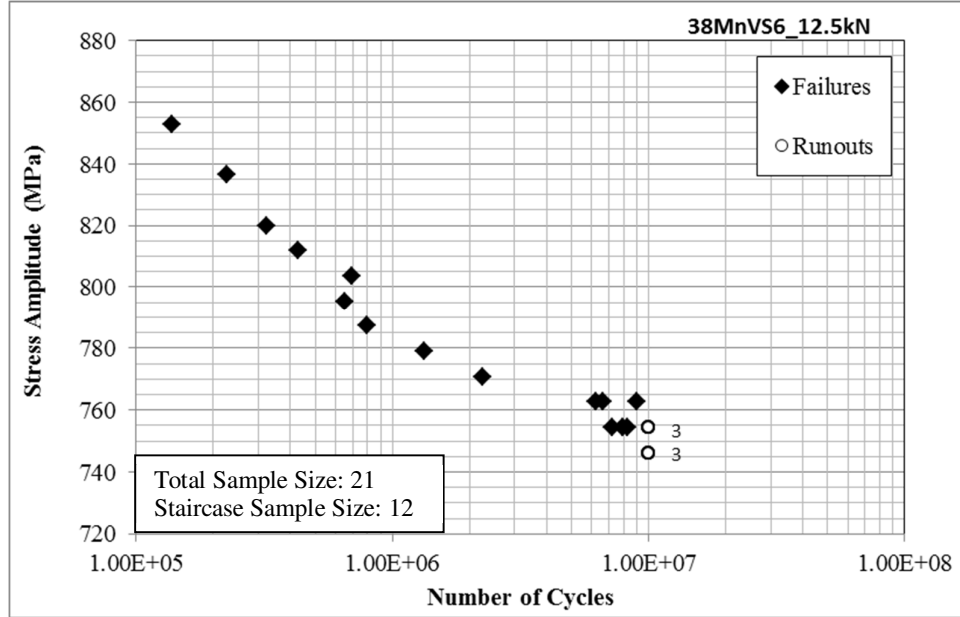


Figure 3.29 S-N curve for 38MnVS6 rolled at 12.5kN fillet rolling load.

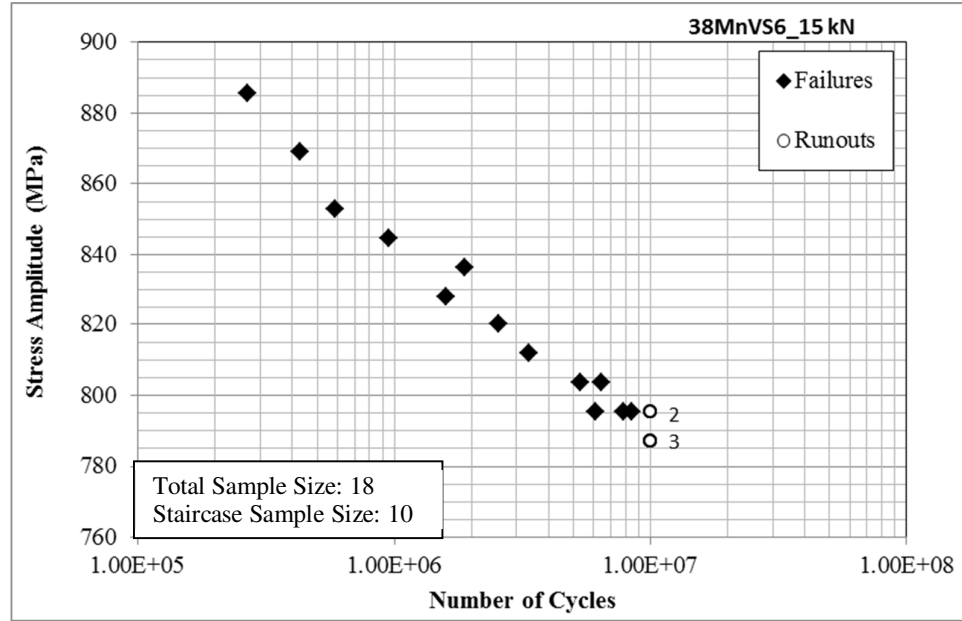


Figure 3.30 S-N curve for 38MnVS6 rolled at 15kN fillet rolling load.

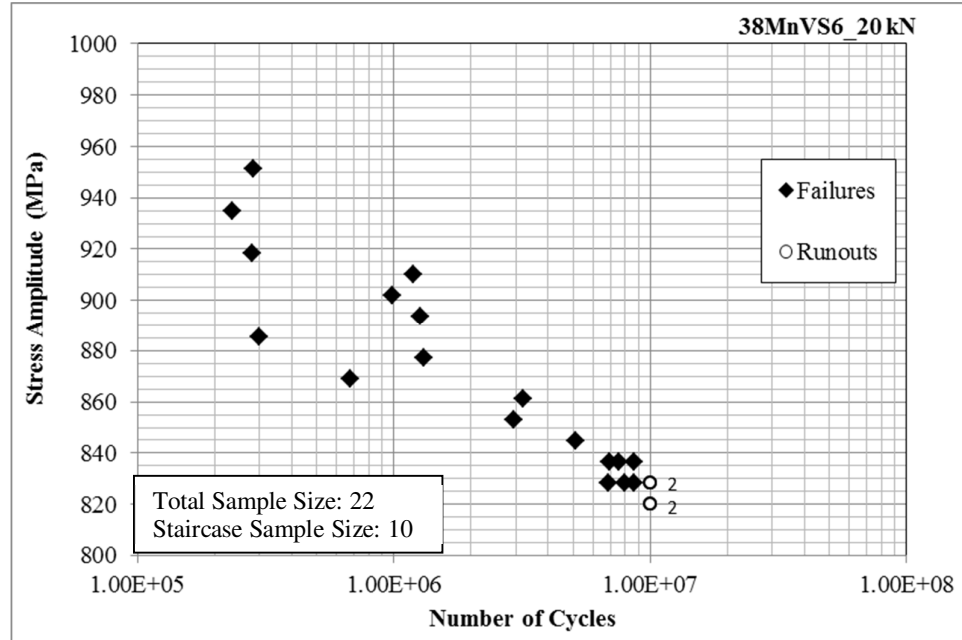


Figure 3.31 S-N curve for 38MnVS6 rolled at 20kN fillet rolling load.

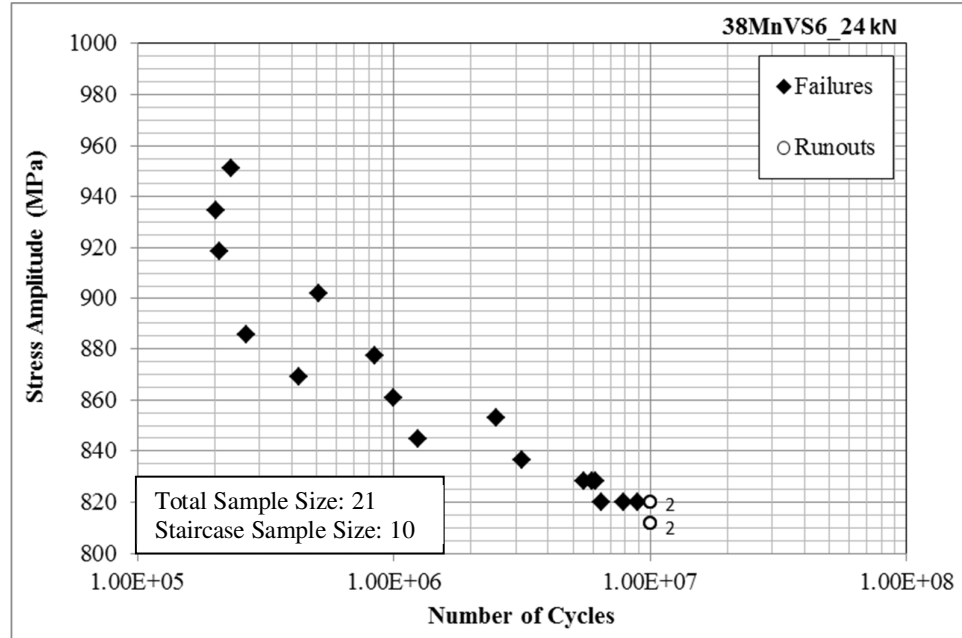


Figure 3.32 S-N curve for 38MnVS6 rolled at 24kN fillet rolling load.

3.4.2 Statistical Analyses of the Fatigue Test Results and Fatigue Limit Calculations

As a first step, the staircase test data were analyzed by Dixon-Mood method [35] in order to calculate the fatigue limits.

Following this, fatigue limits were calculated by Maximum Likelihood Method assuming normal and Weibull distributions.

In order to construct the P-S-N curves, two different regression models were applied. The first is the Basquin Model [29] to obtain a constant log-normal life distribution. The second model is Random Fatigue Life Model described by Pascual and Meeker [40].

Distribution analyses and life regressions were conducted by a excel macro developed for RFL model by Annis [28] and modified by Engler et. al. [29].

The theories based on the described analysis methods were described previously in Chapter 2.

3.4.2.1 Fatigue Limit Calculations by Dixon-Mood Method

In order to apply Dixon-Mood calculations, failure-run-out data were analyzed at transition region of the S-N test data shown on Figures 3.26 to 3.32. Figures 3.33 to 3.39 summarize the failure-run-out data for each test condition.

Equations 2.26 to 2.31 described in section 2.2.3.2.1 were applied to calculate mean and 90% confidence fatigue limits. Standard deviations were also calculated for each S-N data. Table 3.20 summarizes the Dixon-Mood analysis results.

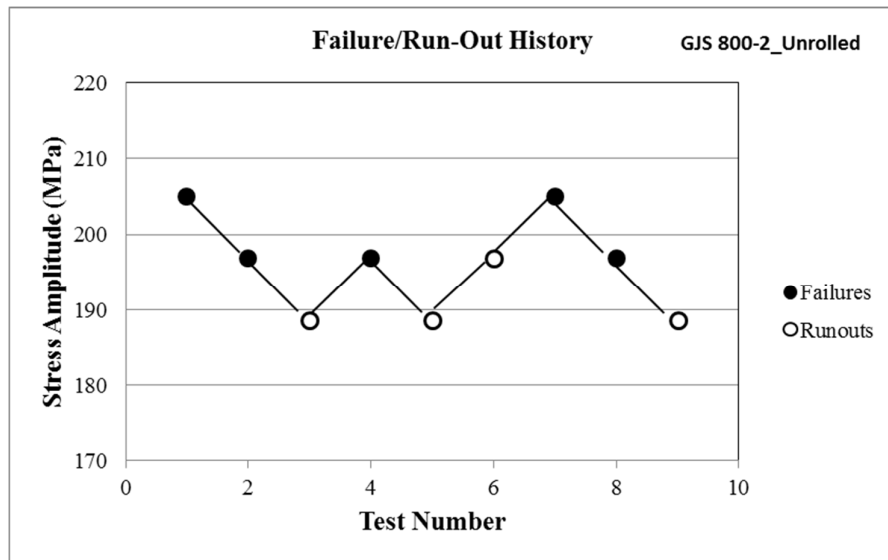


Figure 3.33 Failure run-out history for EN GJS 800-2 at unrolled condition.

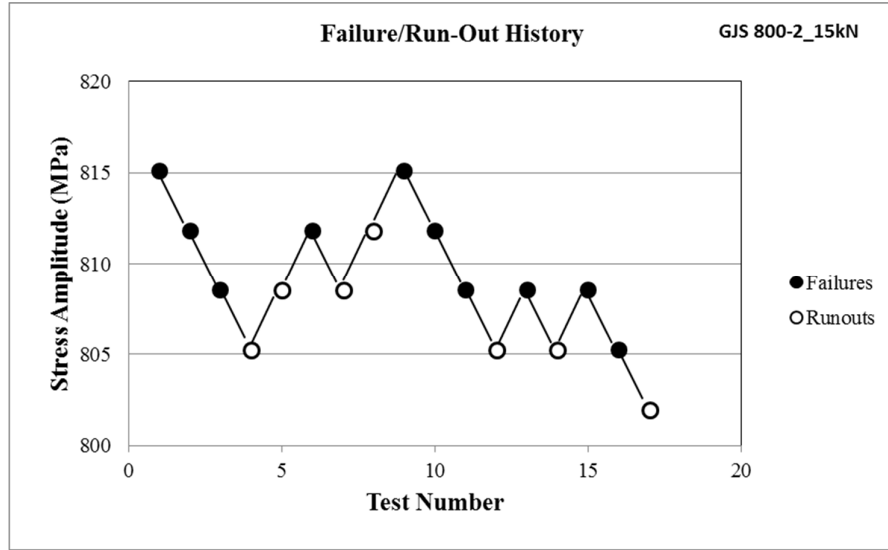


Figure 3.34 Failure run-out history for EN GJS 800-2 rolled at 15kN fillet rolling load.

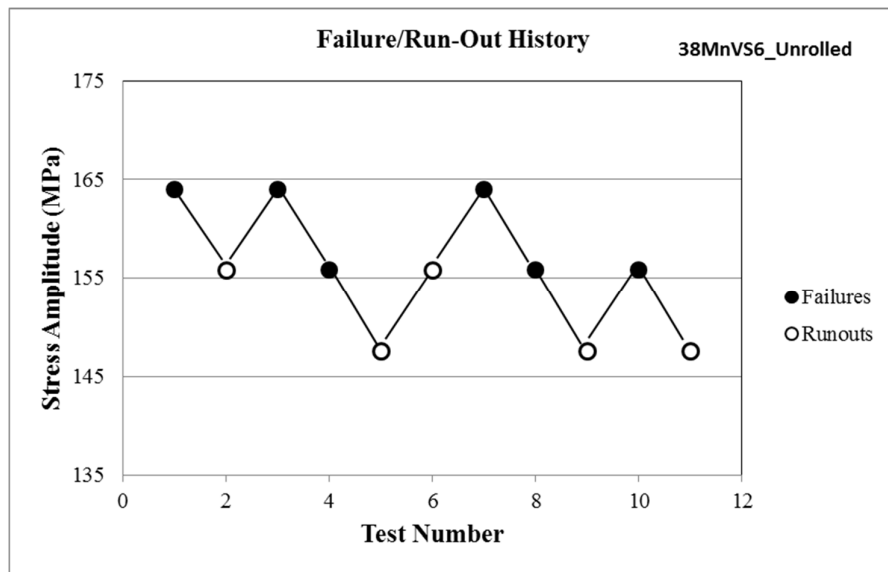


Figure 3.35 Failure run-out history for 38MnVS6 at unrolled condition.

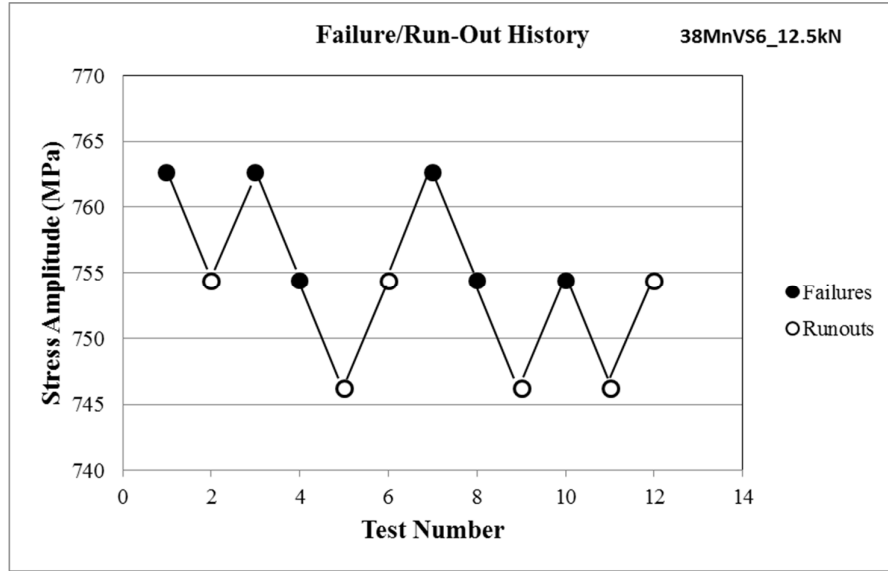


Figure 3.36 Failure run-out history for 38MnVS6 rolled at 12.5kN fillet rolling load.

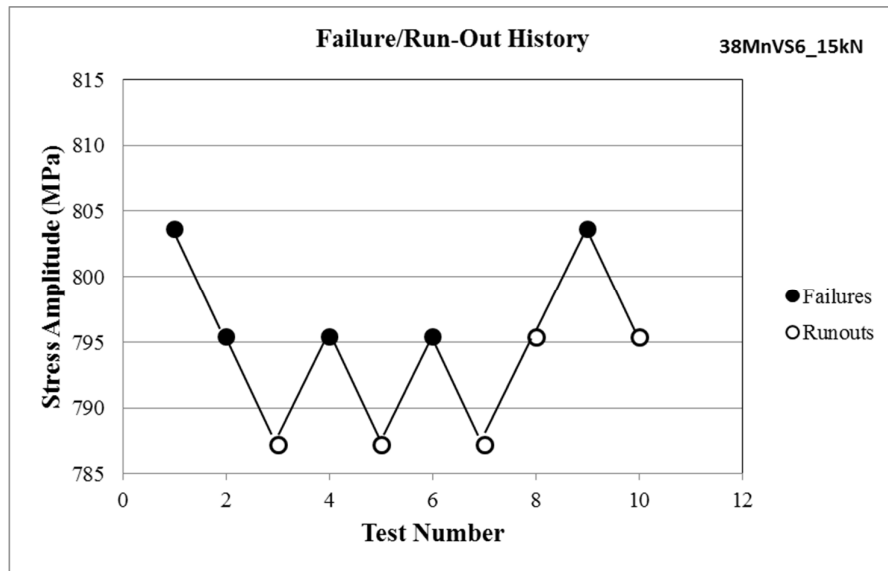


Figure 3.37 Failure run-out history for 38MnVS6 rolled at 15kN fillet rolling load.

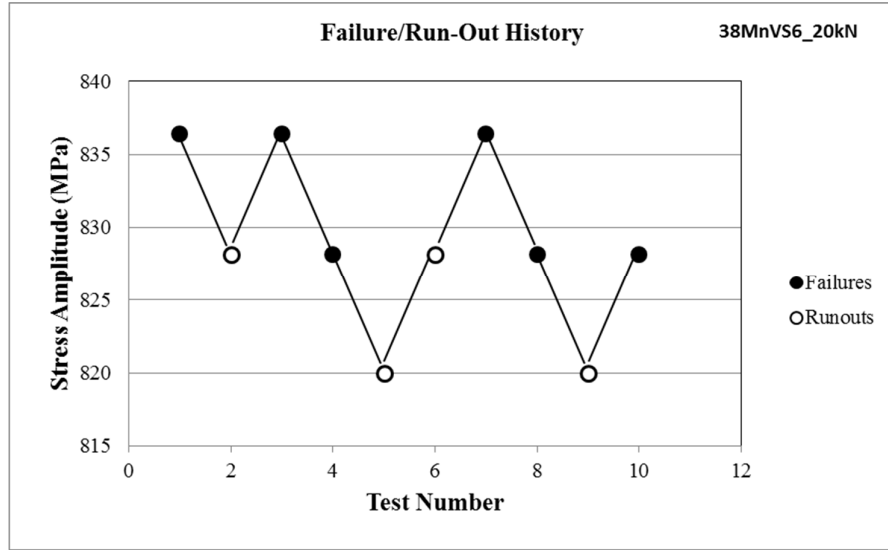


Figure 3.38 Failure run-out history for 38MnVS6rolled at 20kN fillet rolling load.

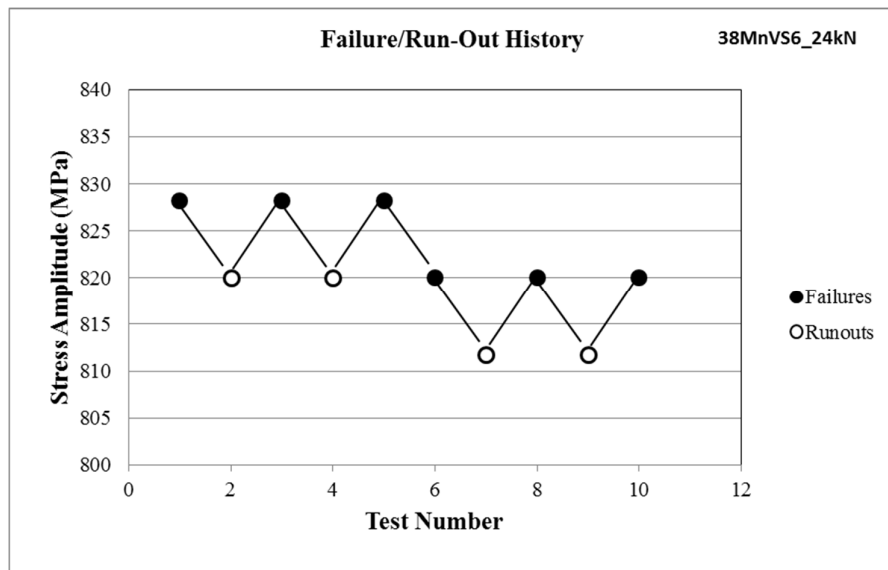


Figure 3.39 Failure run-out history for 38MnVS6rolled at 24kN fillet rolling load.

Table 3.20 Dixon-Mood calculation results.

	Mean Fatigue Limit (MPa)	Fatigue Limit at 90% Confidence		Standard Deviation (σ) (MPa)	Stress Increment (Sd) (MPa)	Sd/σ
		Lower	Upper			
		(MPa)	(MPa)			
GJS 800-2 Un-Rolled	200.90	195.33	206.47	4.35	8.20	1.89
GJS 800-2 Rolled at 15kN	810.98	808.75	813.21	1.74	3.28	1.89
38MnVS6 Un-Rolled	159.90	154.33	165.47	4.35	8.20	1.89
38MnVS6 Rolled at 12.5kN	763.00	757.43	768.57	4.35	8.20	1.89
38MnVS6 Rolled at 15kN	795.40	789.83	800.97	4.35	8.20	1.89
38MnVS6 Rolled at 20kN	832.30	826.73	837.87	4.35	8.20	1.89
38MnVS6 Rolled at 24kN	824.10	818.53	829.67	4.35	8.20	1.89

3.4.2.2 Maximum Likelihood Method Calculations and Life Regressions

Maximum Likelihood Method was used in order to calculate the fatigue limits assuming both normal and Weibull distribution of the test data. In addition, life regressions and fatigue limit calculations were conducted by MLE analysis based on modified Basquin and RFL methods.

By MLE method, the failure and run-out data were analyzed separately by using data censoring.

Equation 3.6 was used for Modified Basquin curve fit method and equations 3.7 and 3.8 were used for RFL curve fit method. during analysis, run-out data were censored by the use of MLE method [29].

$$\sigma_a = C(2N_f)^b \Rightarrow \ln(N_f) = -\frac{\ln(2^b C)}{b} + \frac{1}{b} \ln(\sigma_a) + err = B_0 + B_1 \ln(\sigma_a) + err \quad (3.6)$$

$$\ln(N_f) = B_0 + B_1 \ln(S_a - S_L) + err \quad (3.7)$$

$$S_L = e^{\ln(\eta) + \ln(-\ln(1-P)) / \beta} \quad (3.8)$$

Figures 3.40 to 3.67 summarize the life regression curves at different probability levels, probability density functions and cumulative distribution functions for each test condition.

Tables 3.21 to 3.27 summarize the MLE analysis results tabulating the mean, median and 90% confidence limits, standard deviations and maximum likelihood values for each method.

The curve fit parameters on equations 3.1-3.3 are described and the results for each case were tabulated on Tables 3.28 and 3.29 respectively.

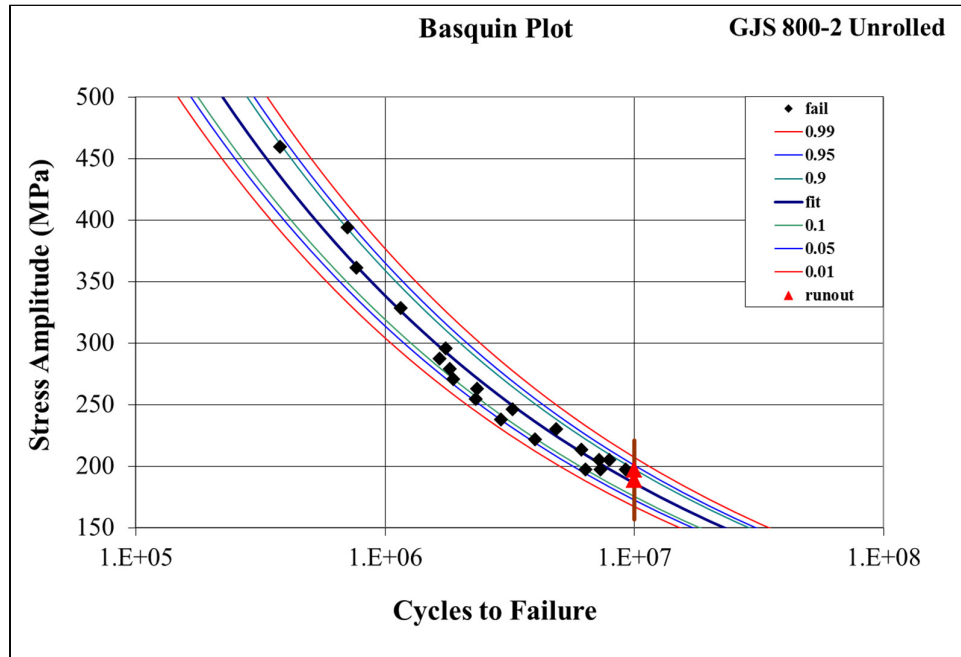


Figure 3.40 Basquin curve fit for EN GJS 800-2 at unrolled condition.

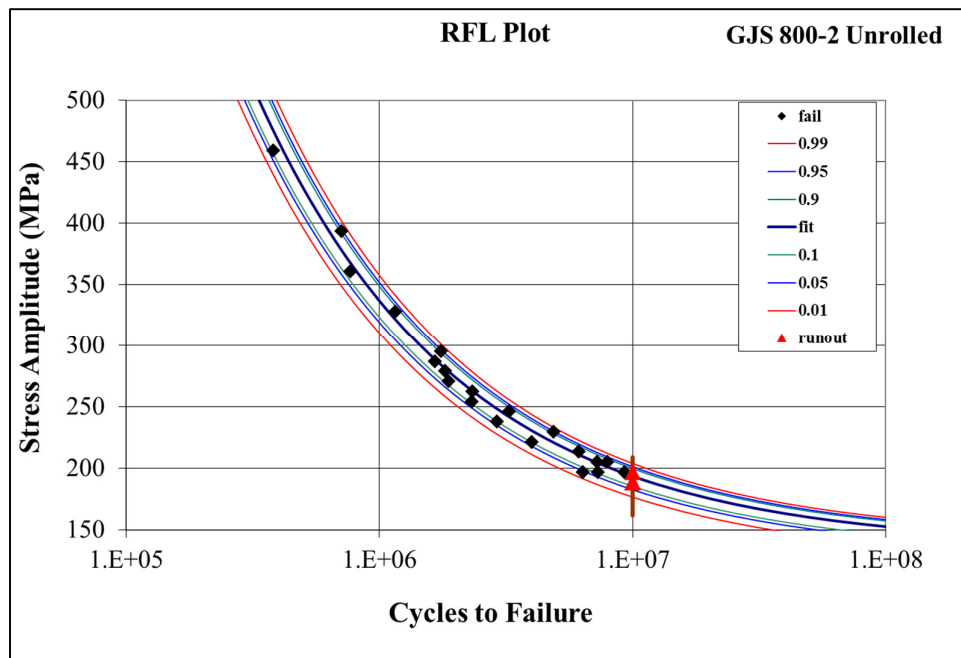


Figure 3.41 RFL curve fit for EN GJS 800-2 at unrolled condition.

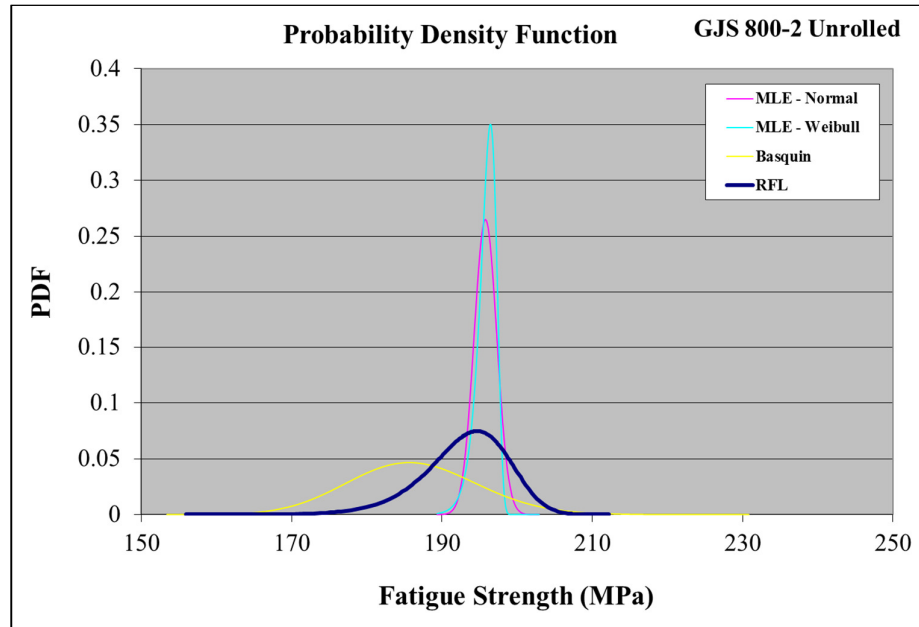


Figure 3.42 Probability density functions for EN GJS 800-2 at unrolled condition.

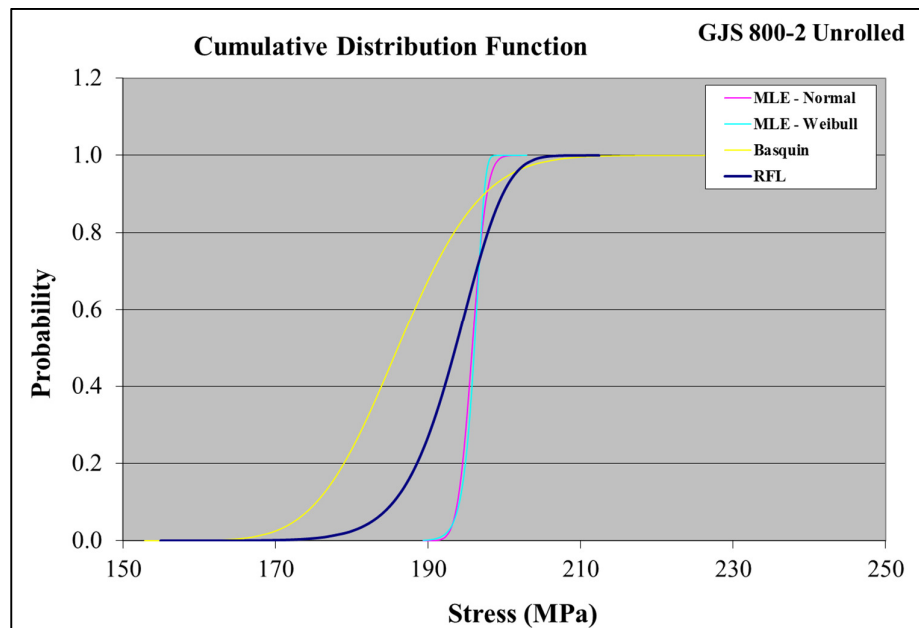


Figure 3.43 Cumulative distribution functions for EN GJS 800-2 at unrolled condition.

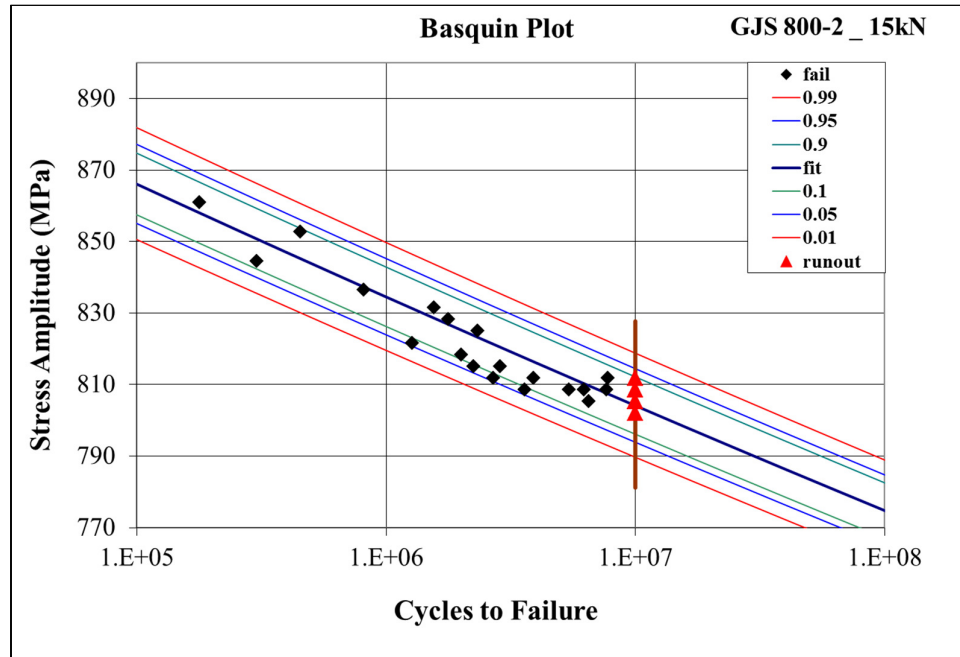


Figure 3.44 Basquin curve fit for EN GJS 800-2 rolled at 15kN rolling load.

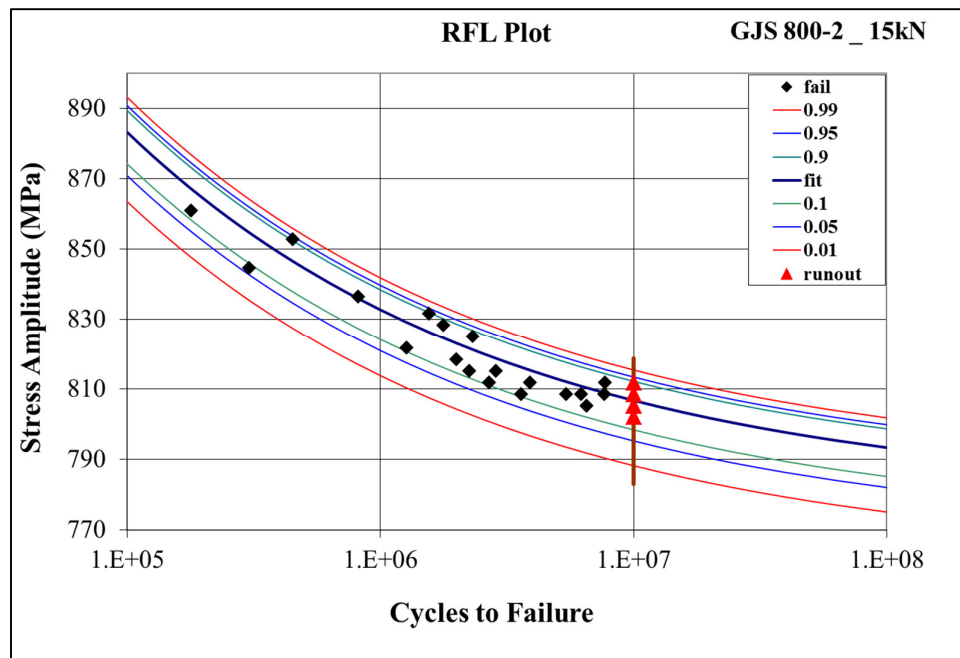


Figure 3.45 RFL curve fit for EN GJS 800-2 rolled at 15kN rolling load.

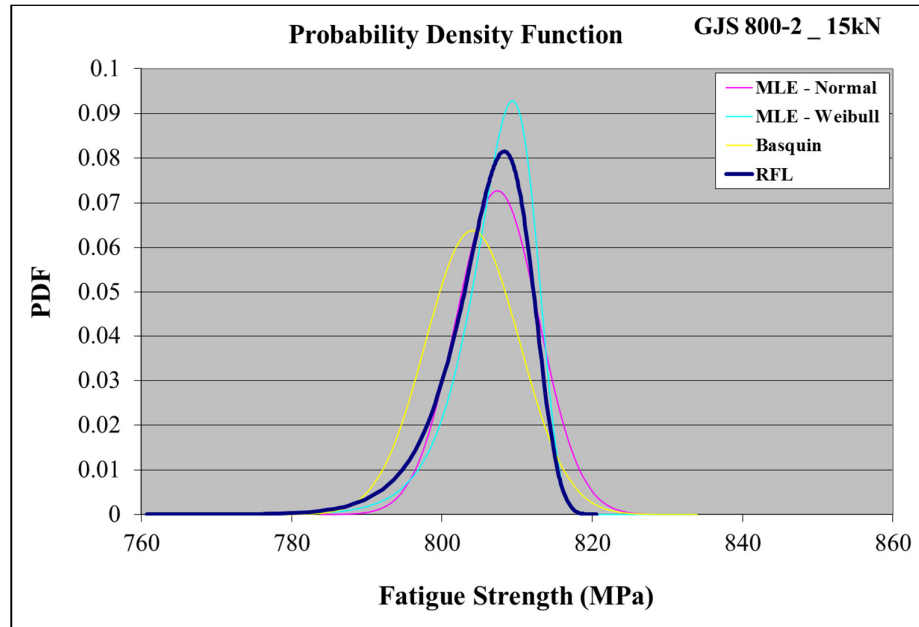


Figure 3.46 Probability density functions for EN GJS 800-2 rolled at 15kN rolling load.

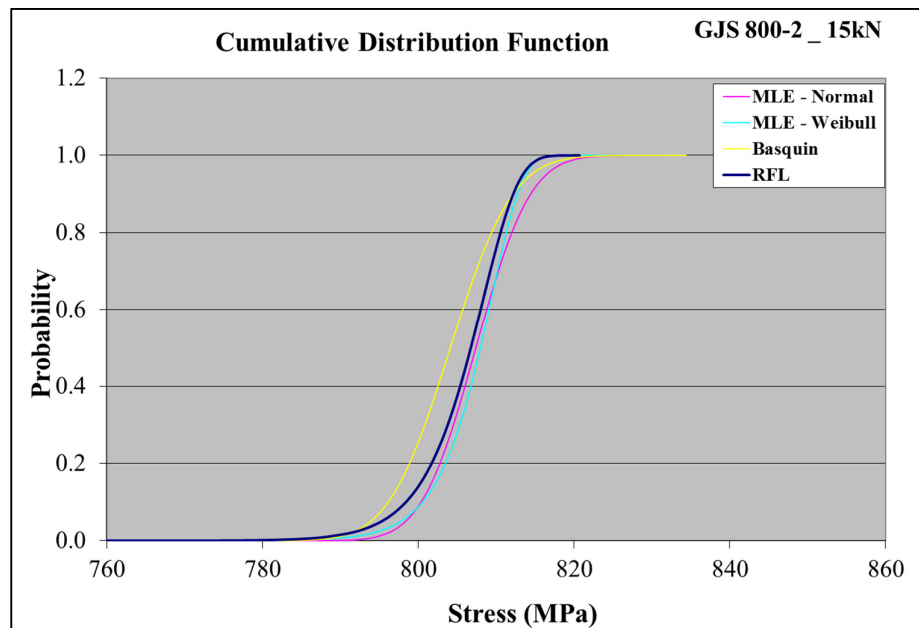


Figure 3.47 Cumulative distribution functions for EN GJS 800-2 rolled at 15kN rolling load.

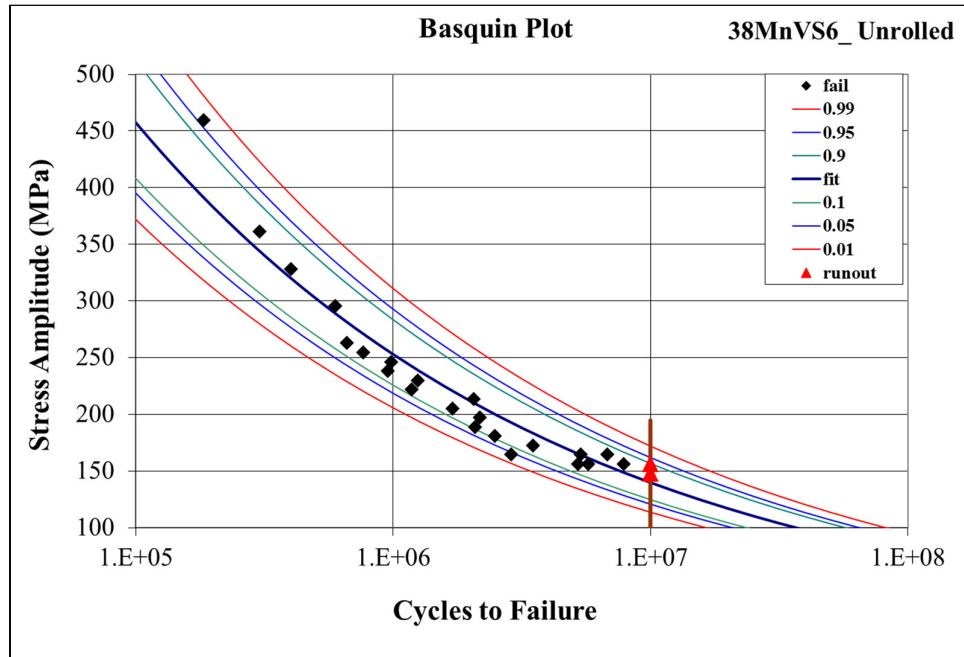


Figure 3.48 Basquin curve fit for 38MnVS6 at unrolled condition.

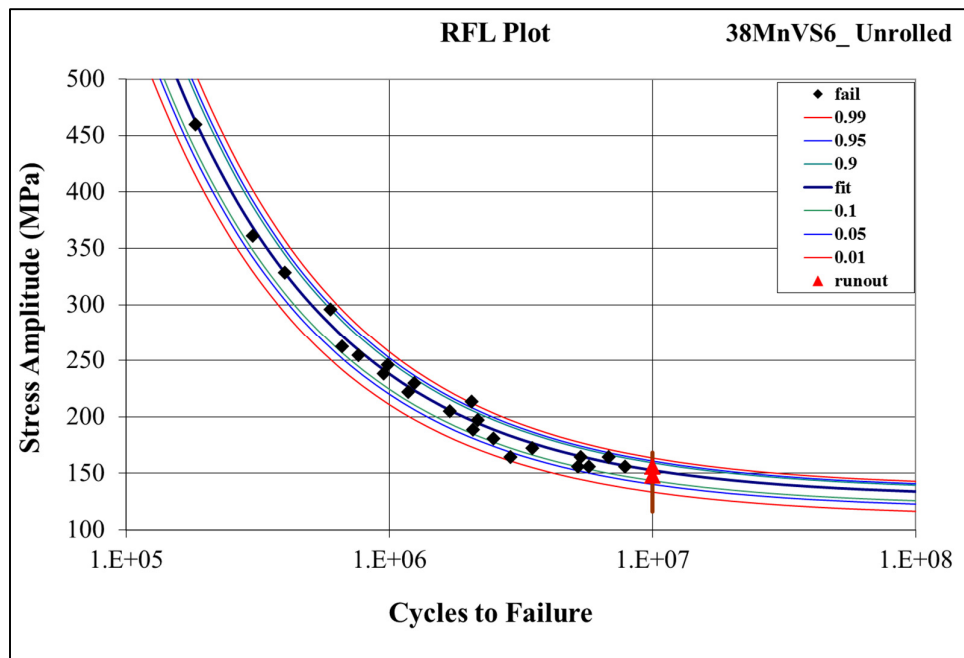


Figure 3.49 RFL curve fit for 38MnVS6 at unrolled condition.

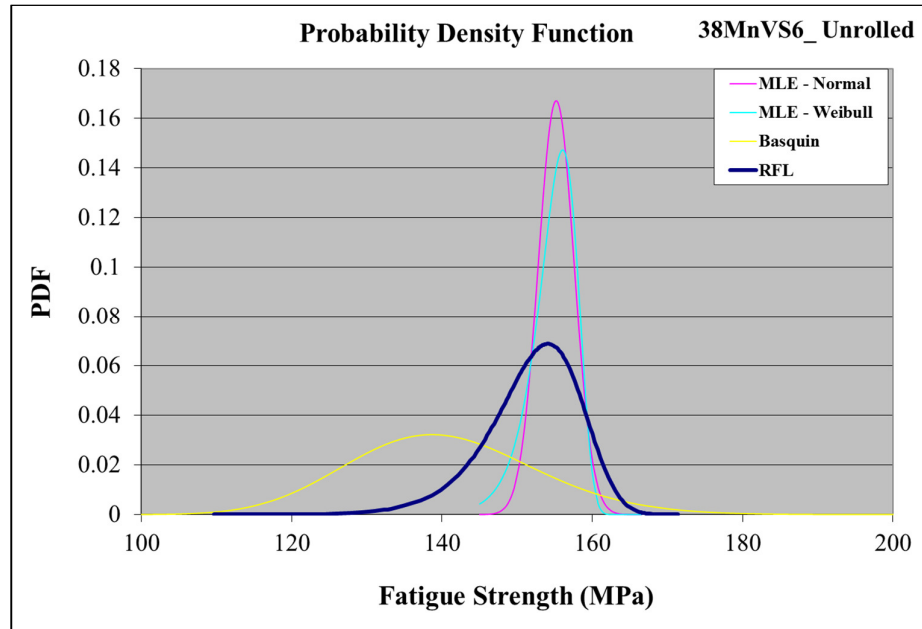


Figure 3.50 Probability density functions for 38MnVS6 at unrolled condition.

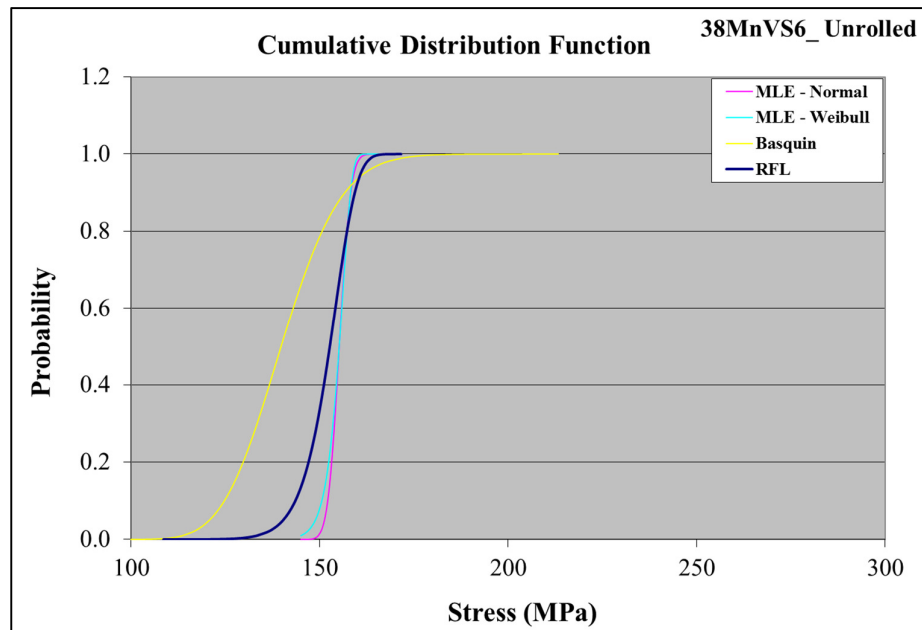


Figure 3.51 Cumulative distribution functions for 38MnVS6 at unrolled condition.

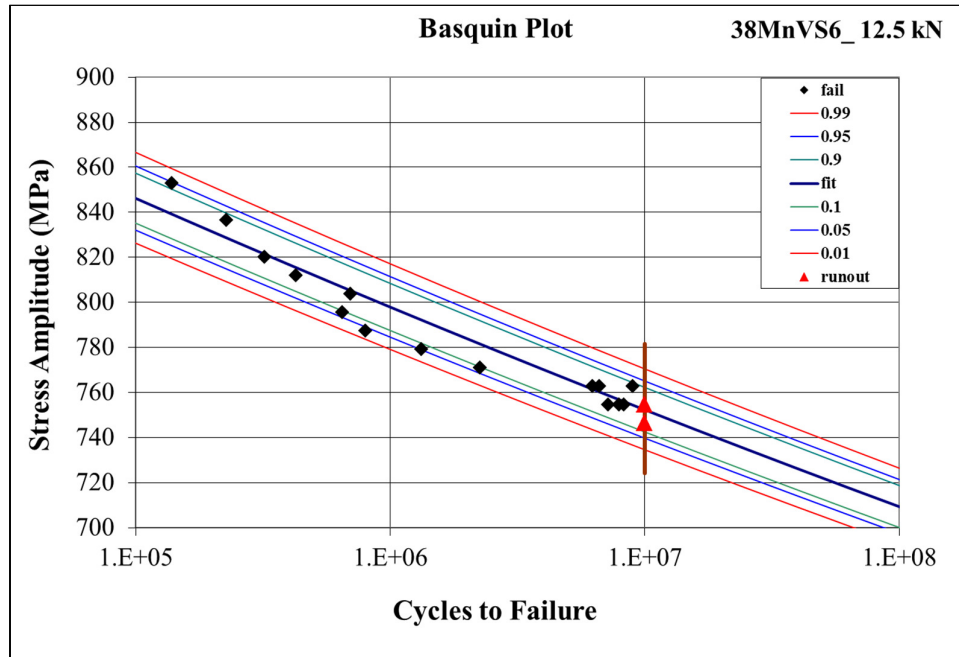


Figure 3.52 Basquin curve fit for 38MnVS6 rolled at 12.5kN rolling load.

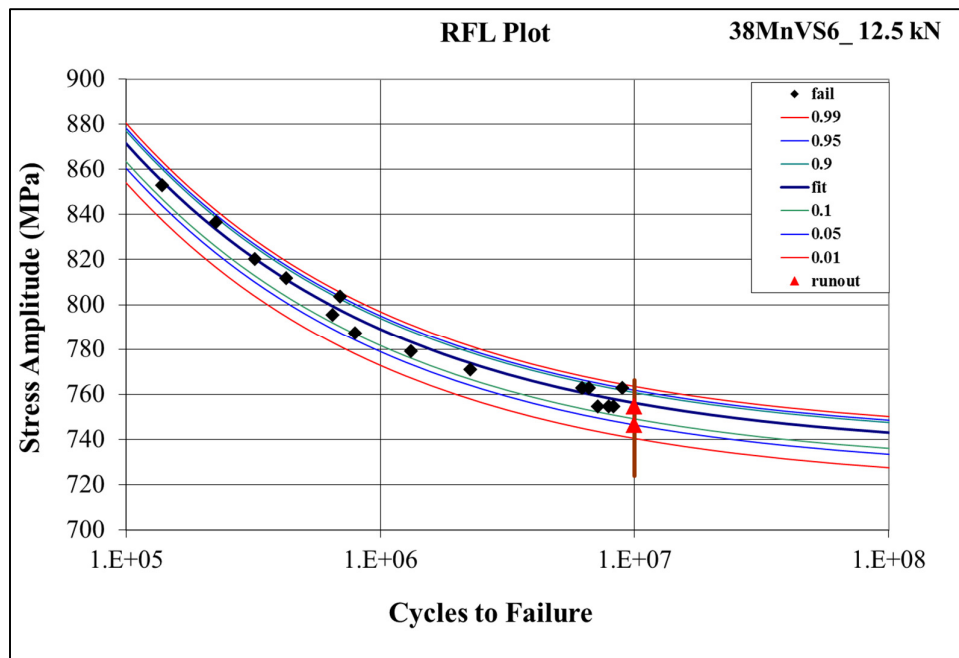


Figure 3.53 RFL curve fit for 38MnVS6 rolled at 12.5kN rolling load.

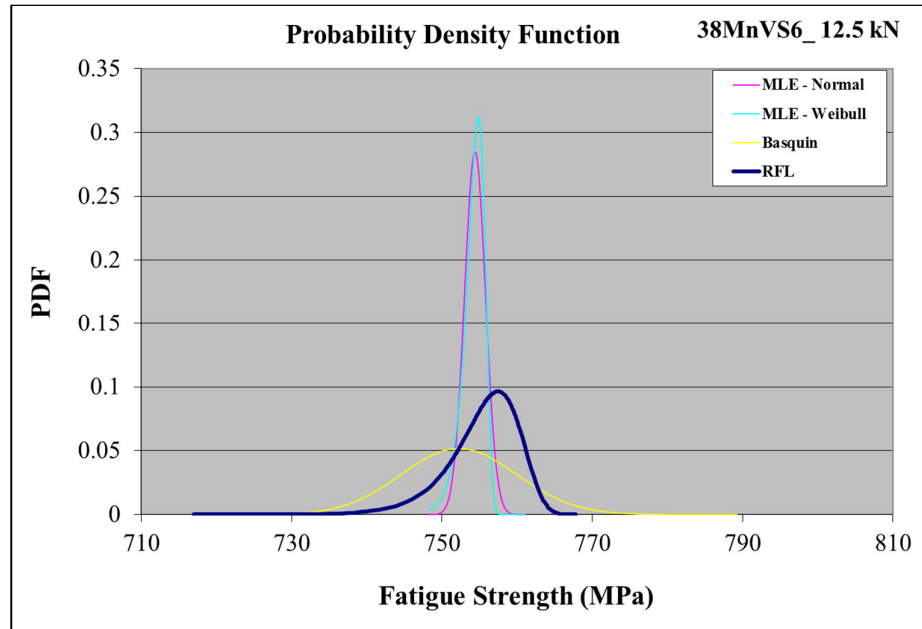


Figure 3.54 Probability density functions for 38MnVS6 rolled at 12.5kN rolling load.

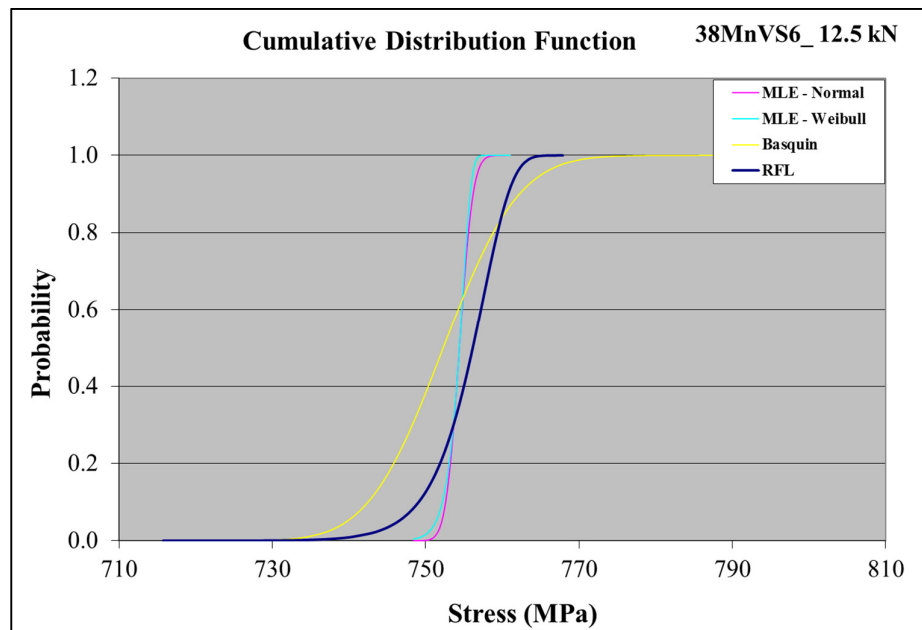


Figure 3.55 Cumulative distribution functions for 38MnVS6 rolled at 12.5kN rolling load.

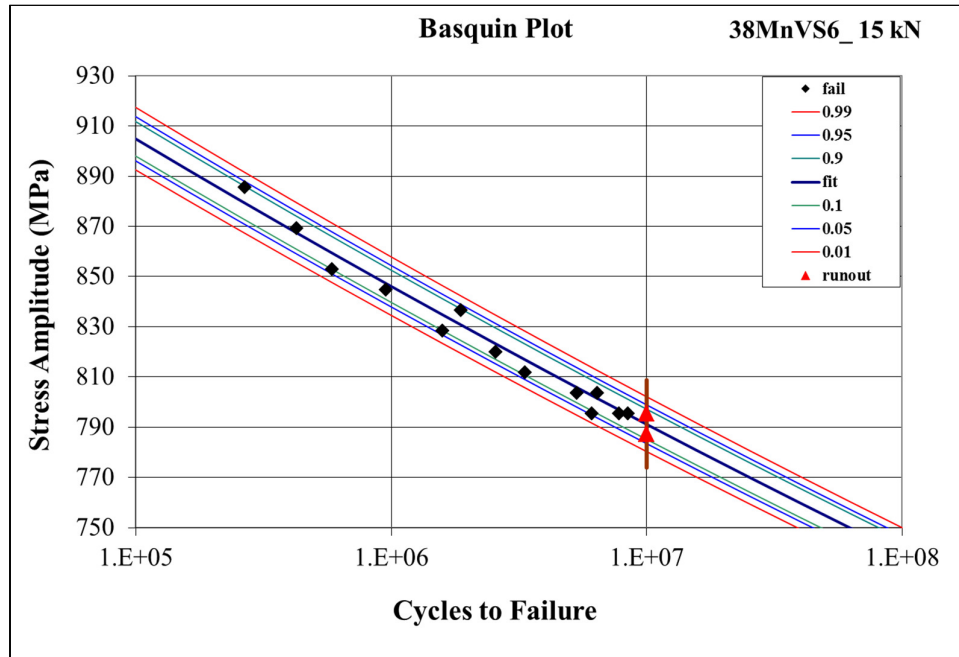


Figure 3.56 Basquin curve fit for 38MnVS6 rolled at 15kN rolling load.

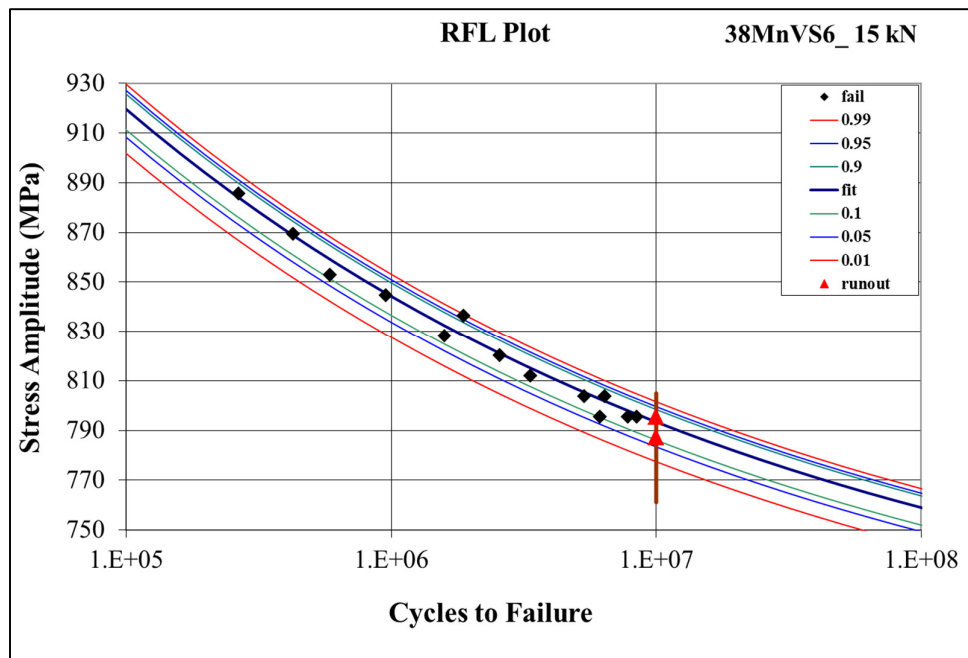


Figure 3.57 RFL curve fit for 38MnVS6 rolled at 15kN rolling load.

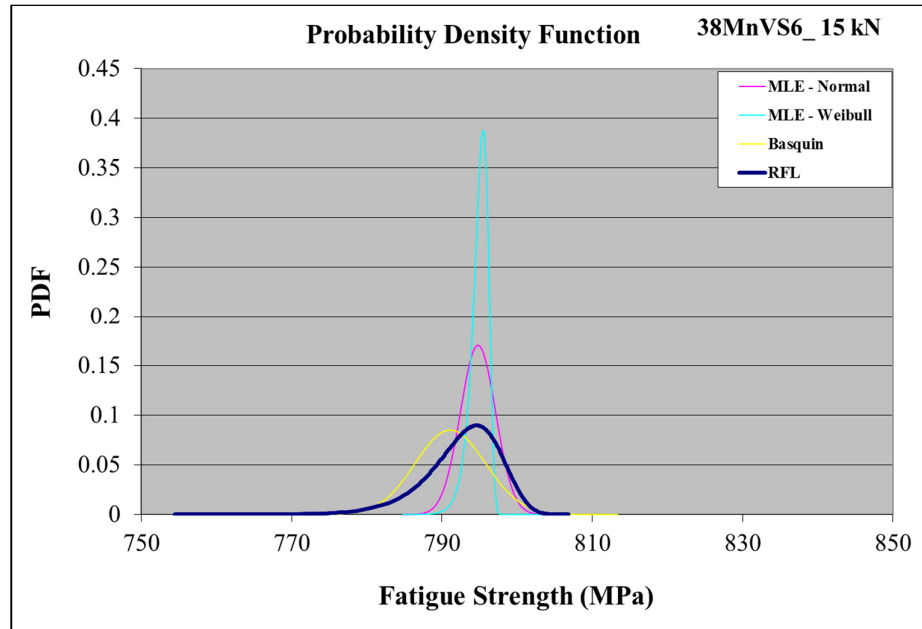


Figure 3.58 Probability density functions for 38MnVS6 rolled at 15kN rolling load.

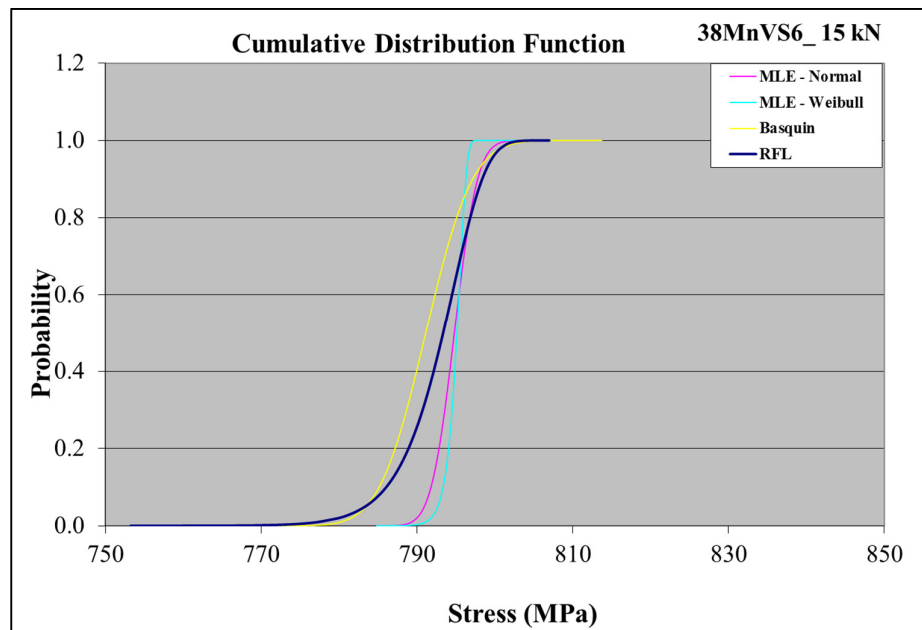


Figure 3.59 Cumulative distribution functions for 38MnVS6 rolled at 15kN rolling load.

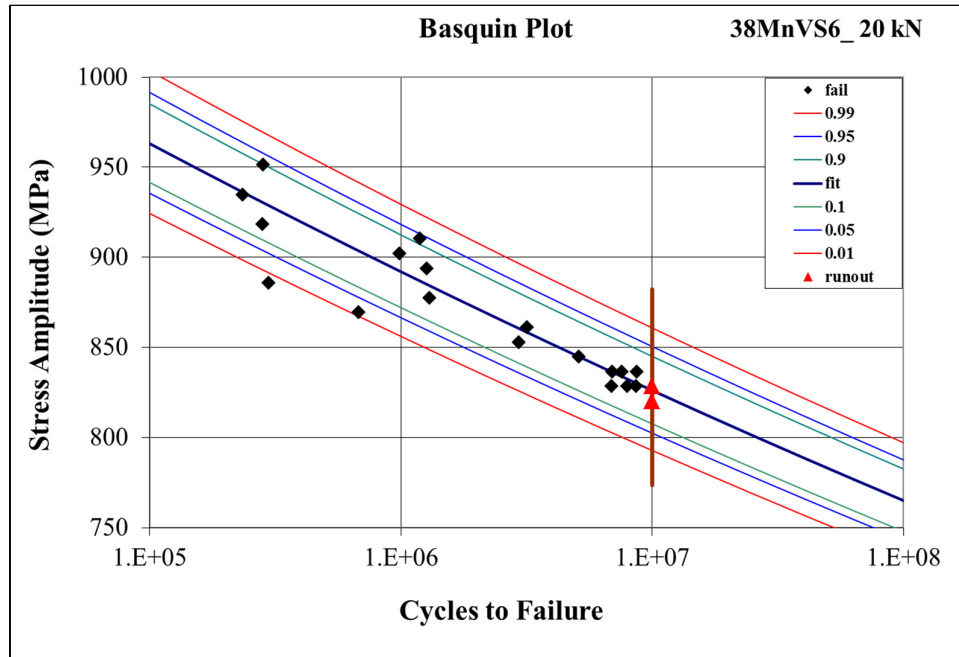


Figure 3.60 Basquin curve fit for 38MnVS6 rolled at 20kN rolling load.

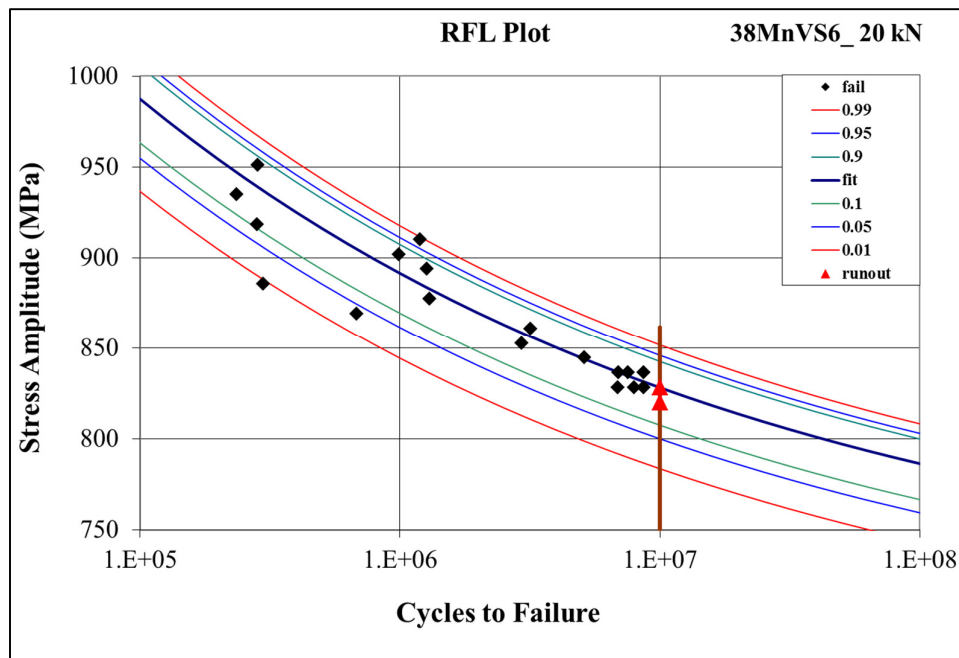


Figure 3.61 RFL fit for 38MnVS6 rolled at 20kN rolling load.

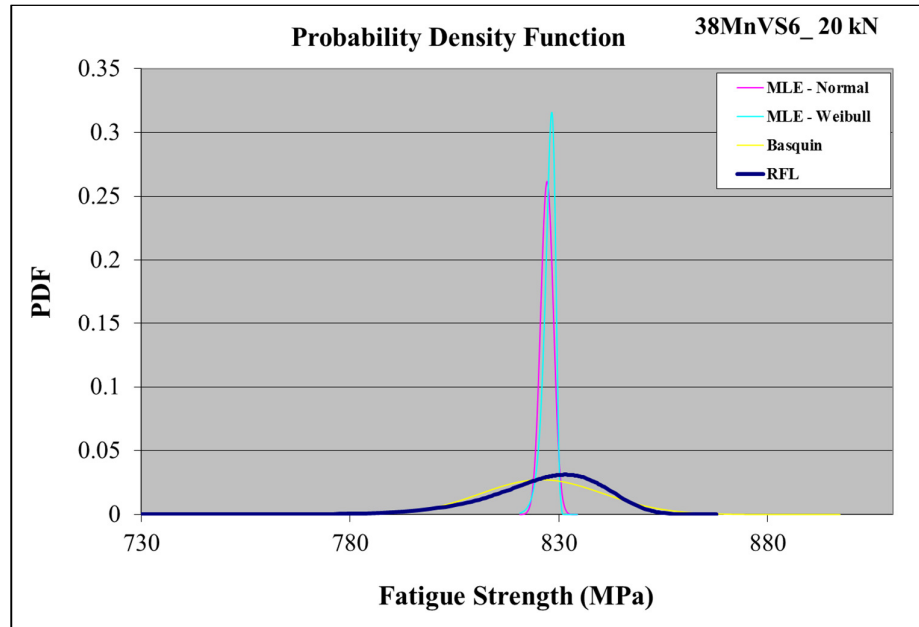


Figure 3.62 Probability density functions for 38MnVS6 rolled at 20kN rolling load.

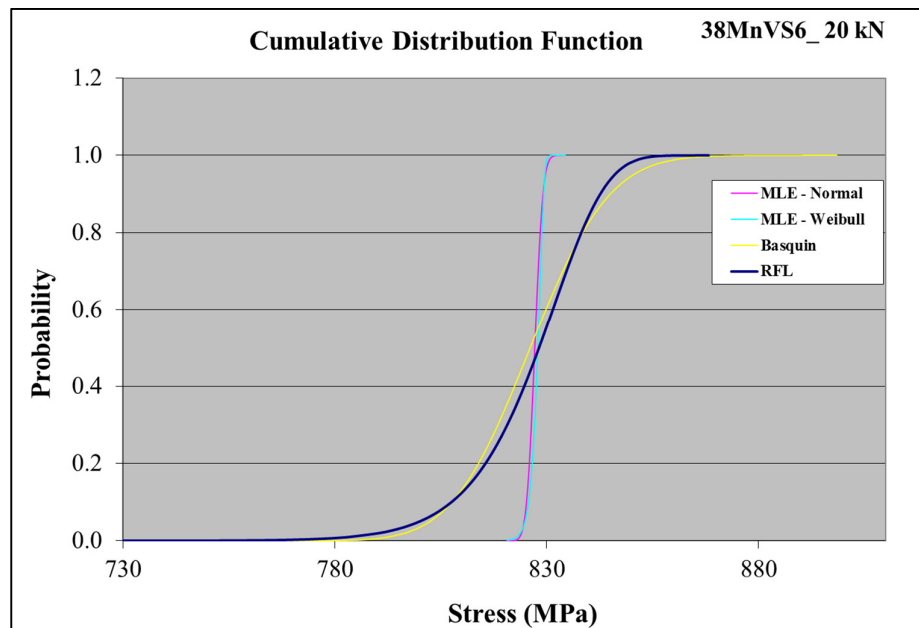


Figure 3.63 Cumulative distribution functions for 38MnVS6 rolled at 20kN rolling load.

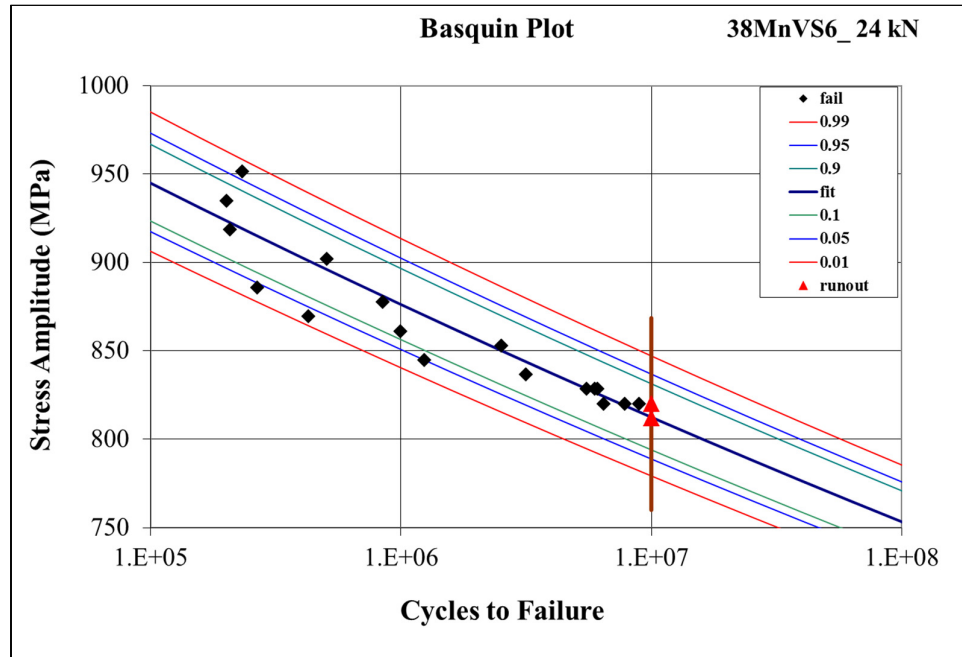


Figure 3.64 Basquin curve fit for 38MnVS6 rolled at 24kN rolling load.

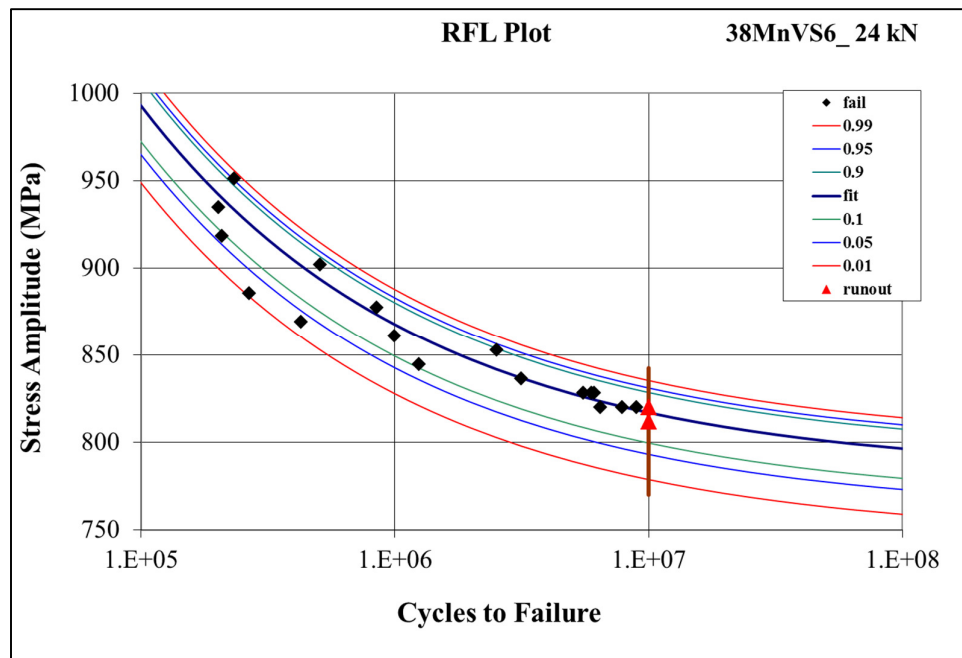


Figure 3.65 RFL curve fit for 38MnVS6 rolled at 24kN rolling load.

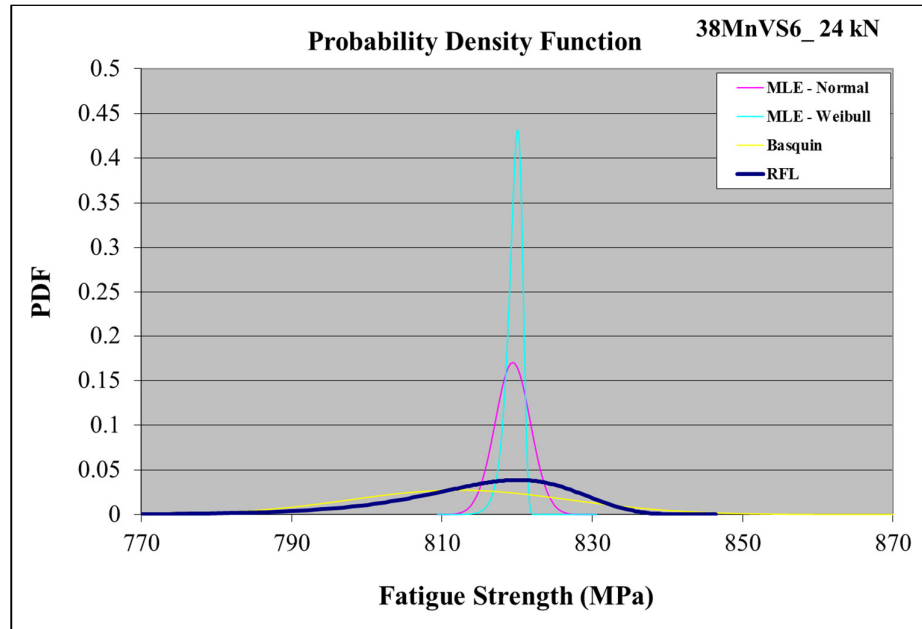


Figure 3.66 Probability density functions for 38MnVS6 rolled at 24kN rolling load.

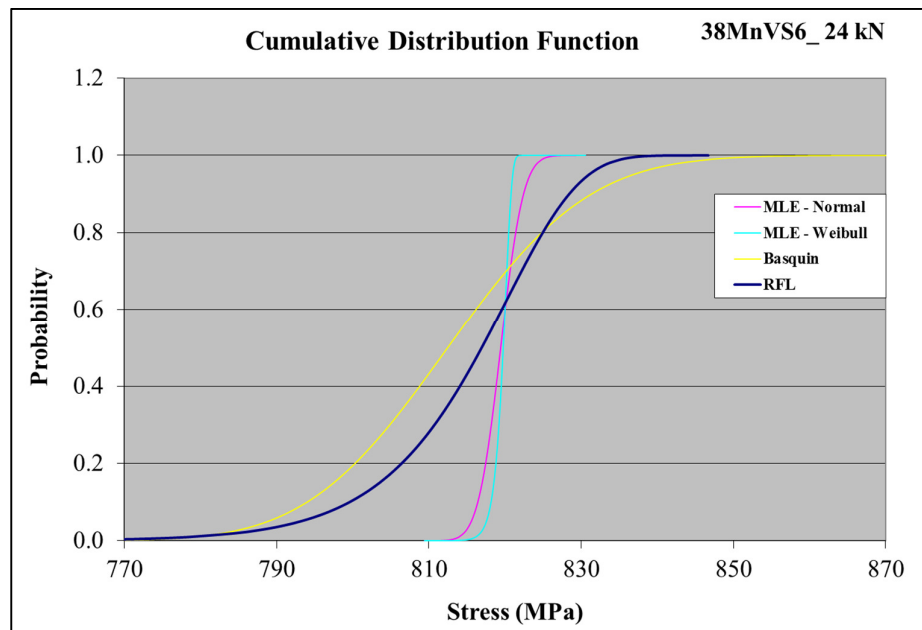


Figure 3.67 Cumulative distribution functions for 38MnVS6 rolled at 24kN rolling load.

Table 3.21 Summary of MLE results for EN GJS 800-2 at unrolled condition.

Method	Regression Model	Distribution	Mean (MPa)	Median (MPa)	Standard Deviation (MPa)	Likelihood	B10 (MPa)
MLE	Modified Basquin	Log-Normal	186.23	186.03	8.59	1.40E+01	175.37
MLE	RFL	----	192.95	193.60	5.75	1.31E+05	185.45
MLE	----	Normal	195.78	195.78	1.51	1.05E-01	193.86
MLE	----	Weibull	195.86	196.07	1.34	1.05E-01	194.15

Table 3.22 Summary of MLE results for EN GJS 800-2 rolled at 15kN rolling load.

Method	Regression Model	Distribution	Mean (MPa)	Median (MPa)	Standard Deviation (MPa)	Likelihood	B10 (MPa)
MLE	Modified Basquin	Log-Normal	804.13	804.11	6.25	5.34E-09	796.13
MLE	RFL	----	805.71	806.74	5.68	3.51E-08	798.04
MLE	----	Normal	807.38	807.38	5.49	1.38E-04	800.35
MLE	----	Weibull	807.14	807.95	5.05	1.52E-04	800.37

Table 3.23 Summary of MLE results for 38MnVS6 at unrolled condition.

Method	Regression Model	Distribution	Mean (MPa)	Median (MPa)	Standard Deviation (MPa)	Likelihood	B10 (MPa)
MLE	Modified Basquin	Log-Normal	140.34	139.79	12.50	2.40E-06	124.74
MLE	RFL	----	151.89	152.70	6.35	8.86E+01	143.48
MLE	----	Normal	155.20	155.20	2.39	3.45E-02	152.14
MLE	----	Weibull	154.70	155.19	3.14	3.15E-02	150.57

Table 3.24 Summary of MLE results for 38MnVS6 rolled at 12.5kN rolling load.

Method	Regression Model	Distribution	Mean (MPa)	Median (MPa)	Standard Deviation (MPa)	Likelihood	B10 (MPa)
MLE	Modified Basquin	Log-Normal	752.33	752.29	7.71	1.45E-05	742.48
MLE	RFL	----	755.26	756.14	4.81	4.42E-01	749.08
MLE	----	Normal	754.40	754.40	1.40	1.56E-02	752.61
MLE	----	Weibull	754.15	754.40	1.51	1.56E-02	752.18

Table 3.25 Summary of MLE results for 38MnVS6 rolled at 15kN rolling load.

Method	Regression Model	Distribution	Mean (MPa)	Median (MPa)	Standard Deviation (MPa)	Likelihood	B10 (MPa)
MLE	Modified Basquin	Log-Normal	791.15	791.12	4.69	5.05E-01	785.14
MLE	RFL	----	792.51	793.36	5.04	1.60E+00	786.05
MLE	----	Normal	794.80	794.80	2.34	3.45E-02	791.80
MLE	----	Weibull	794.94	795.14	1.21	3.45E-02	793.35

Table 3.26 Summary of MLE results for 38MnVS6 rolled at 20kN rolling load.

Method	Regression Model	Distribution	Mean (MPa)	Median (MPa)	Standard Deviation (MPa)	Likelihood	B10 (MPa)
MLE	Modified Basquin	Log-Normal	826.21	826.08	14.6	5.77E-08	807.59
MLE	RFL	----	826.11	828.18	14.28	1.81E-07	807.52
MLE	----	Normal	827.17	827.17	1.52	1.05E-01	825.22
MLE	----	Weibull	827.63	827.88	1.49	3.45E-02	825.69

Table 3.27 Summary of MLE results for 38MnVS6 rolled at 24kN rolling load.

Method	Regression Model	Distribution	Mean (MPa)	Median (MPa)	Standard Deviation (MPa)	Likelihood	B10 (MPa)
MLE	Modified Basquin	Log-Normal	812.46	812.59	14.57	4.11E-08	794.00
MLE	RFL	----	814.98	816.93	11.84	2.32E-06	799.58
MLE	----	Normal	819.42	819.42	2.35	3.45E-02	816.42
MLE	----	Weibull	819.58	819.76	1.09	3.46E-02	818.16

Table 3.28 Definitions of Modified Basquin and RFL model parameters.

Model	Parameter	Descriptor
Modified Basquin	C	S-N curve coefficient
	b	S-N curve coefficient
	err	Standard deviation in lognormal fatigue life
Random Fatigue Limit	B ₀	S-N curve coefficient
	B ₁	S-N curve coefficient
	η	Weibull location parameter for fatigue limit
	β	Weibull scale parameter for fatigue limit
	err	Standard deviation in lognormal fatigue life

Table 3.29 Modified Basquin and RFL model parameter values.

Model	Parameter	EN-GJS 800-2 Unrolled	EN-GJS 800-2 15kN	38MnVS6 Unrolled	38MnVS6 12.5kN	38MnVS6 15kN	38MnVS6 20kN	38MnVS6 24kN
Modified Basquin	C	14719.03	1054.54	10595.66	1155.78	1291.82	1446.92	1409.95
	b	-0.26	-0.02	-0.26	-0.03	-0.03	-0.03	-0.03
	err	0.18	0.48	0.35	0.40	0.20	0.53	0.55
Random Fatigue Limit	B ₀	23.55	27.60	20.95	23.84	43.52	42.75	25.13
	B ₁	-1.84	-3.46	-1.52	-2.51	-5.87	-5.54	-2.55
	η	137.57	780.80	130.26	735.67	688.55	708.95	785.76
	β	41.94	180.60	29.74	200.00	200.00	73.03	87.25
	err	0.05	0.02	0.06	0.02	0.04	0.10	0.04

3.5 Fracture Characteristics

In this part, both macro- a micro-analysis were carried on failed crankshaft samples from the resonant bending fatigue rig tests in order evaluate the fracture characteristics.

As described schematically on Figure 3.68 fatigue cracks start at the crank pin fillet region where stress concentration is present and propagates towards the free end of the section following the path shown. Representatively, the crack path on a failed sample was emphasized by liquid penetrant application and demonstrated on Figure 3.69 on an EN-GJS 800-2 cast iron crankshaft sample after test. This representative figure summarizes the crack path observed in all test specimens at each design conditions of the crankshaft. This path is approximately 55 degrees to the crankshaft axis as in-service failures which explains the reason of selecting this angle in rolling operation. Approximately the same direction and angle to the crankshaft axis were observed on all test samples. Figure 3.70 demonstrates the crack initiation, crack propagation and final fracture regions on the fracture surface of a fully fractured specimen of an EN-GJS 800-2 crankshaft representatively.

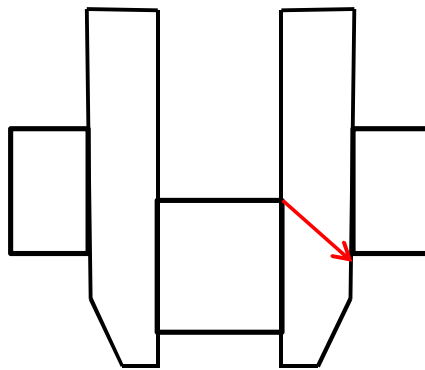


Figure 3.68 A schematic representation crack propagation direction along the crankshaft cross-section.



Figure 3.69 Crack path on failure region on an EN-GJS 800-2 crankshaft sample rolled at 15kN.

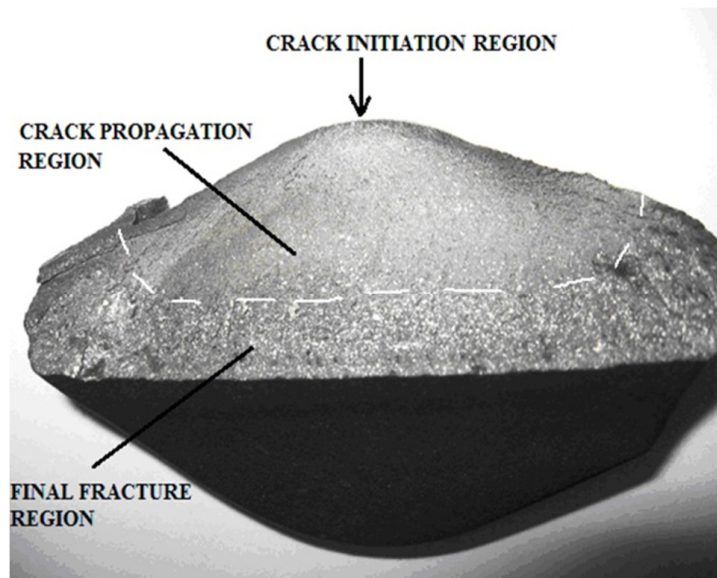


Figure 3.70 Crack surface from a fully fractured test specimen from EN-GJS 800-2 crankshaft rolled at 15kN.

On Figure 3.71 a steel crankshaft test sample section is shown depicting the undercut region and induction hardened zone. Figure 3.72 shows the crack through the section magnified by liquid penetrant.

Figure 3.73 shows the microscopic view of the cracked region. As can be seen from this figure, a secondary crack is associated with the main crack; which indicates a high stress concentration at the fillet region.

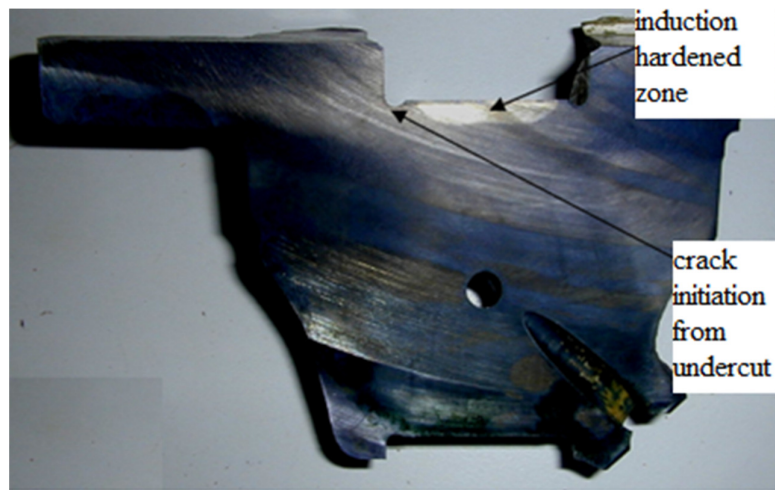


Figure 3.71 Crankshaft section showing the undercut region and induction hardened region (from 38MnVS6 crankshaft sample rolled at 12.5kN).

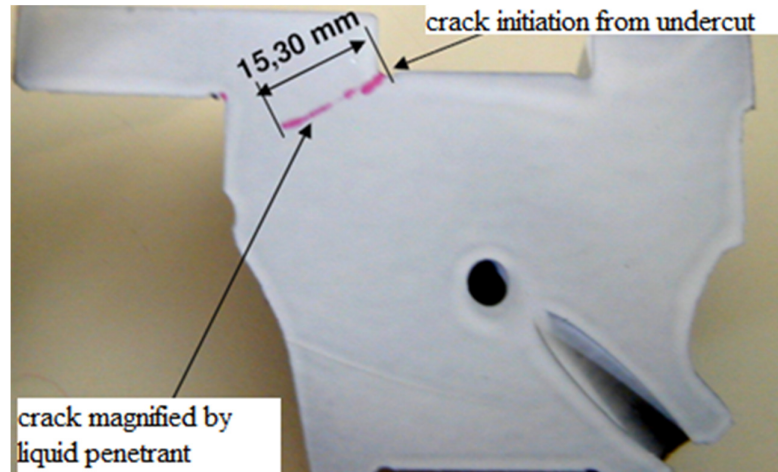


Figure 3.72 Crack along the section magnified by liquid penetrant (from 38MnVS6 crankshaft sample rolled at 12.5kN).

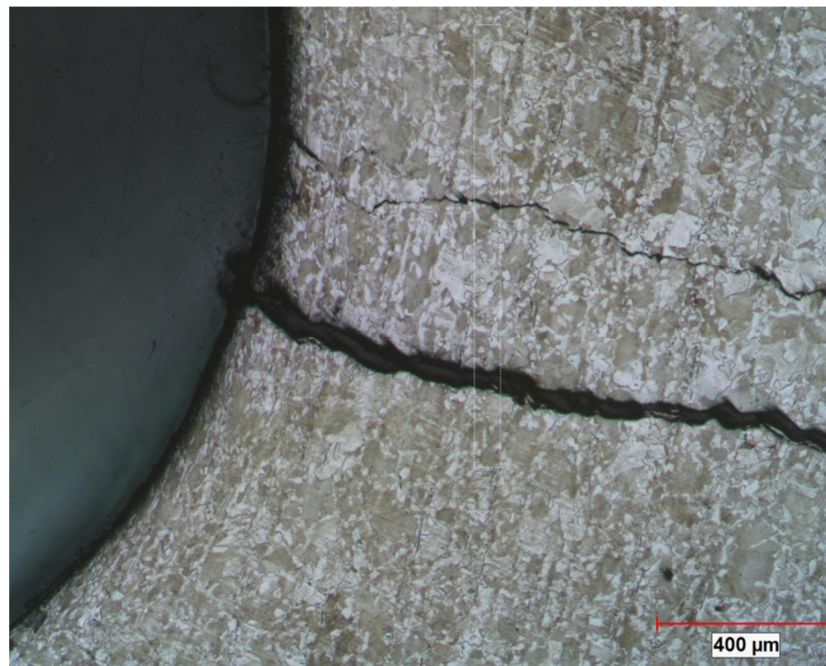


Figure 3.73 Primary and a secondary crack on a 38MnVS6 crankshaft sample rolled at 12.5kN.

Figure 3.74 shows the crack initiation region on a ductile cast iron crankshaft test specimen monitored by Scanning Electron Microscope (SEM). Graphite nodules distributed in microstructure can be differentiated on this micrograph. As indicated by arrows, cracks may initiate at multiple sites depending on the amount of stress concentration. Figures 3.75 and 3.76 show more magnified views of a crack initiation sites.

Figure 3.77 and 3.78 show graphite nodules in pearlite matrix which is the classical bulls eye structure for ductile cast iron. Graphite nodules near or open to the surface can serve as stress concentration points and can de-bond from the pearlite matrix under loading, which in turn can lead to fatigue crack initiation.

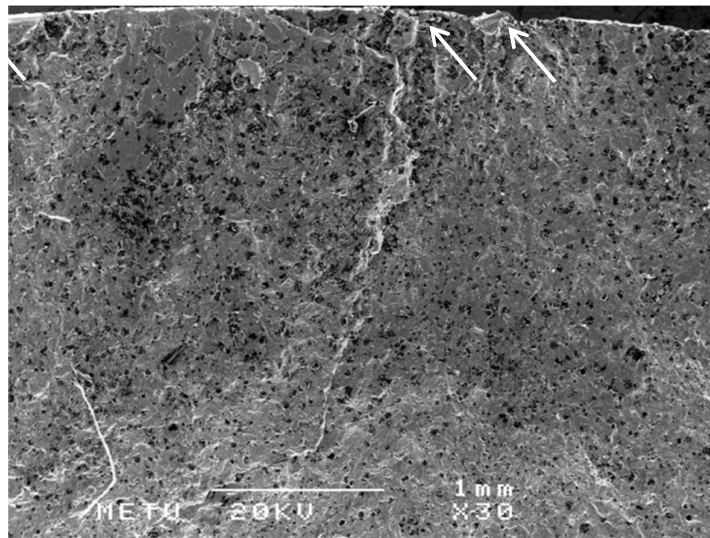


Figure 3.74 Fractograph showing the crack initiation region, X30 (EN-GJS 800-2 crankshaft rolled at 15kN).

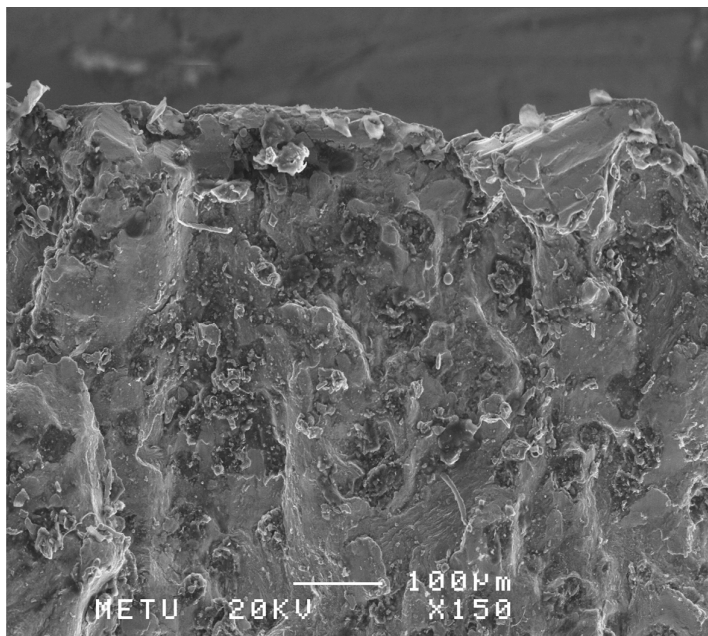


Figure 3.75 Fractograph showing the crack initiation region, X150 (EN-GJS 800-2 crankshaft rolled at 15kN).

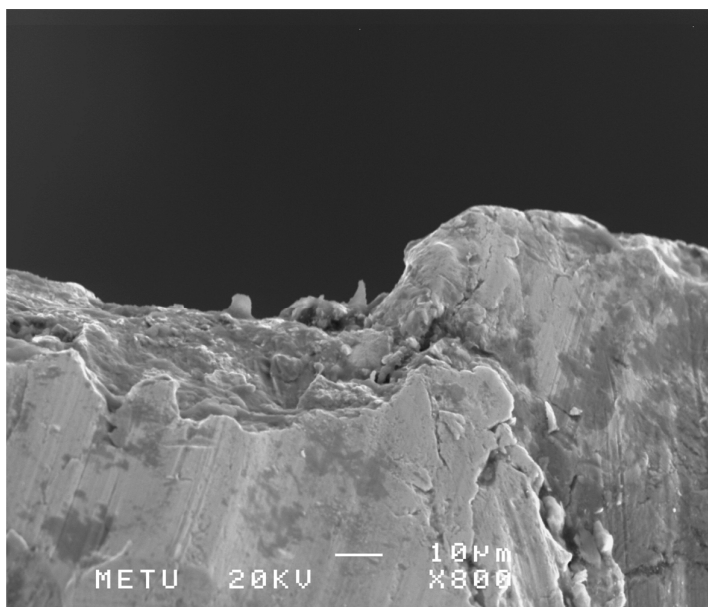


Figure 3.76 Fractograph showing the crack initiation region, X800 (EN-GJS 800-2 crankshaft rolled at 15kN).

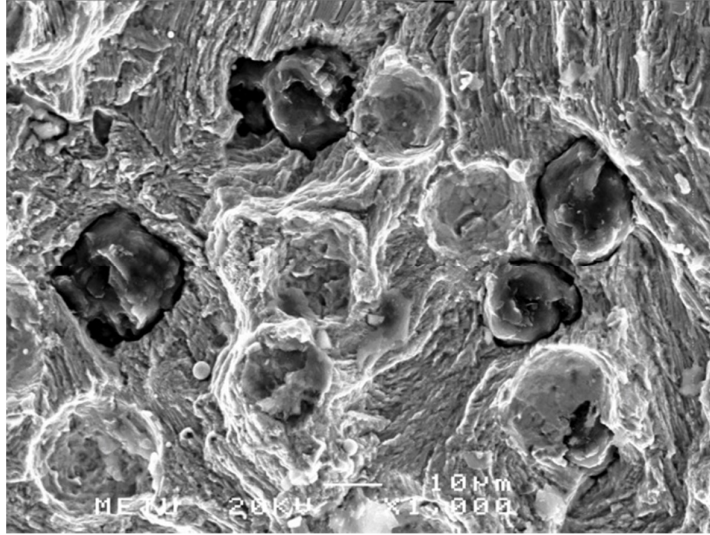


Figure 3.77 Graphite nodules in pearlite matrix, X1000 (EN-GJS 800-2 crankshaft rolled at 15kN).

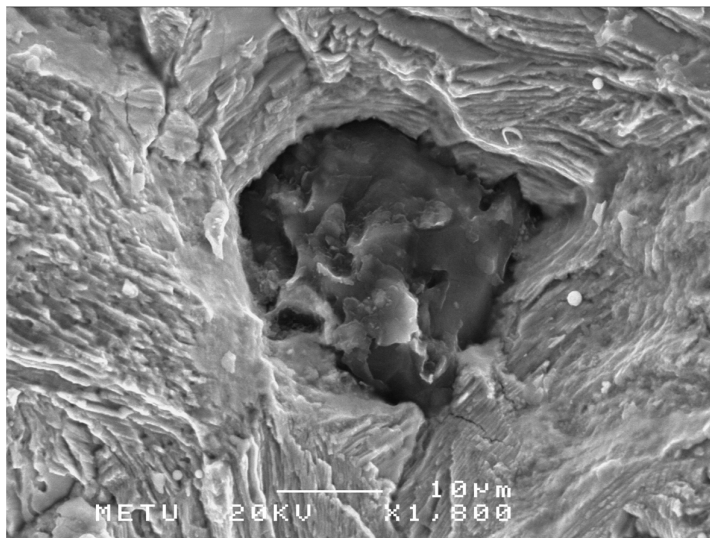


Figure 3.78 Graphite nodule in pearlite matrix, X1800 (EN-GJS 800-2 crankshaft rolled at 15kN).

Figure 3.79 shows the multiple crack initiation sites on a steel crankshaft test specimen monitored by Scanning Electron Microscope (SEM). Figure 3.80 shows the two crack initiation sites at X1400 magnification. Figure 3.81 is a representative fractograph showing the fatigue striations in the crack propagation region. Figures 3.82 and 3.83 show the cleavage planes and river patterns which describe brittle type of fracture in the uncontrolled crack growth region.

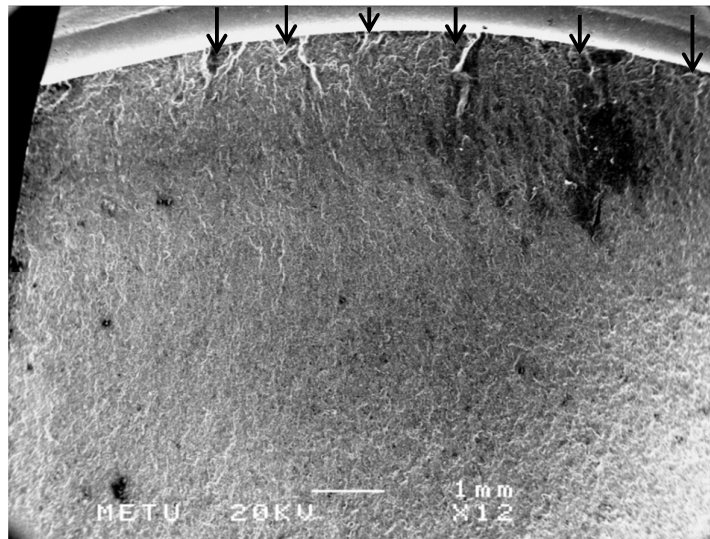


Figure 3.79 Multiple crack initiation sites at the undercut region, X12 (38MnVS6 crankshaft rolled at 12.5kN).

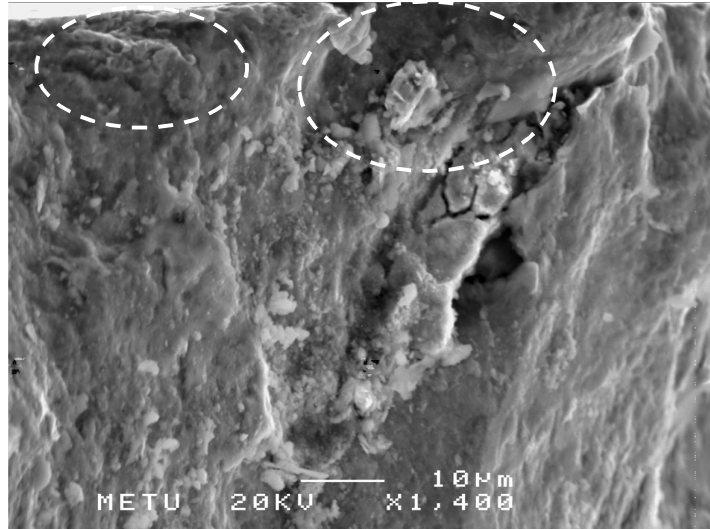


Figure 3.80 Fractograph showing the two crack initiation sites, X1400 (38MnVS6 crankshaft rolled at 12.5kN).

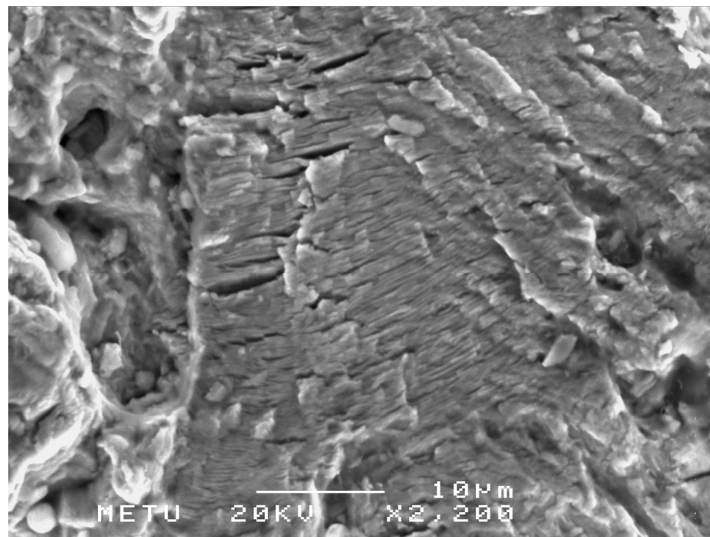


Figure 3.81 Fatigue striations in the crack propagation zone, X2200 (38MnVS6 crankshaft rolled at 12.5kN).

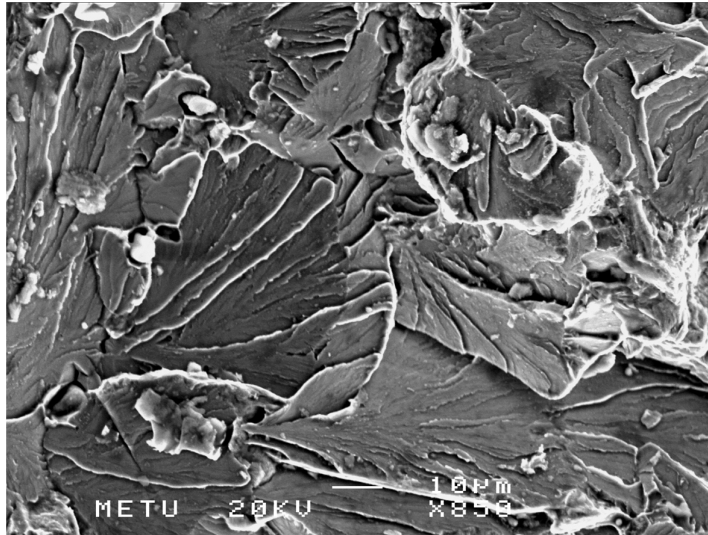


Figure 3.82 Cleavage planes from final fracture region, X850 (38MnVS6 crankshaft rolled at 12.5kN).



Figure 3.83 River patterns from the final fracture region, X1900 (38MnVS6 crankshaft rolled at 12.5kN).

CHAPTER 4

FINITE ELEMENT ANALYSIS

This chapter is composed of two main sections. In the first section, the finite element method, used in residual stress calculations, is summarized. The second section aims to describe the stress calculation method in resonance bending fatigue tests.

4.1 Residual Stress Calculations

This section summarizes the method developed to calculate the residual stresses induced at the fillet region as a result of fillet rolling process. For this purpose, fillet rolling process was dynamically simulated by ABAQUS commercial program and compressive residual stresses induced at the fillet region were calculated through the crankshaft section.

4.1.1 Finite Element Model

In order to simulate the finite element process, three dimensional crankshaft section and fillet roller models were constructed by Hypermesh.

The model is illustrated schematically in Figure 4.1. At the fillet region a fine mesh size of 0.1mm was used and mesh size was increased gradually from the fillet region. For the crankshaft, C3D4 tetrahedral elements were used. For the roller, rigid elements of R3D4 type were used. Detailed views of the fillet region and the roller were shown on Figure 4.2 and 4.3.

Rolling process was simulated dynamically by the use of ABAQUS program. An explicit model was used since the rolling process is time dependent. The actual rolling process velocity of 80RPM was used in simulations. An elastic-plastic material model was used for residual stress calculations with Von Mises Yield criterion. Experimentally obtained true stress-strain data (Figures 3.3 and 3.4) for the two type of crankshaft materials were used for the application of Kinematic Hardening model for deformation process. Since Kinematic Hardening model is used, one cycle of the process was utilized in the simulations. In order to save from CPU timings, rolling process was restricted to 120 degrees of crankshaft rotation during analyses.

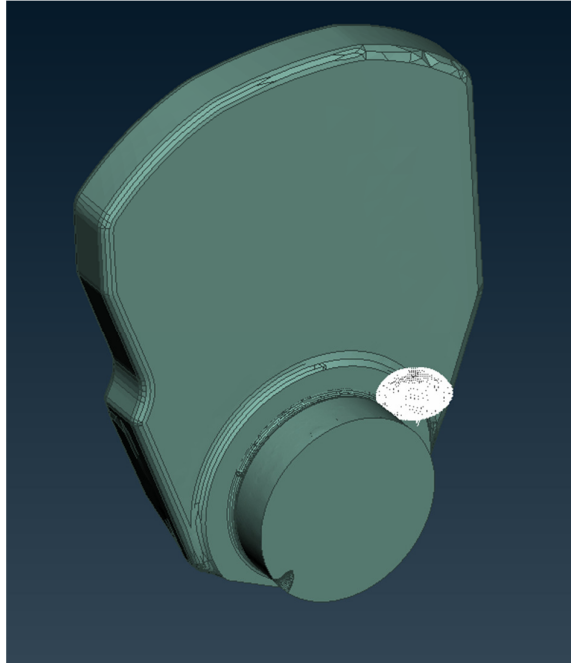


Figure 4.1 Model for rolling process; crankshaft section and the roller.

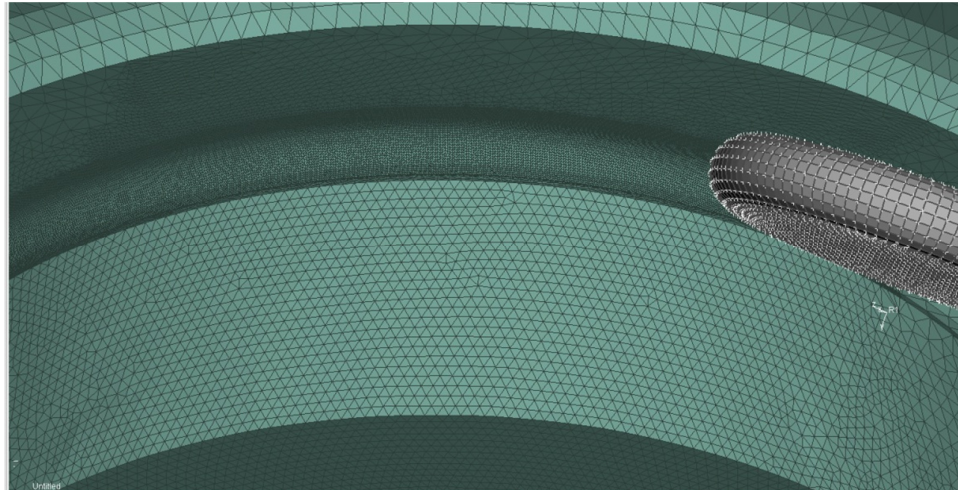


Figure 4.2 View of the fillet region and the roller.

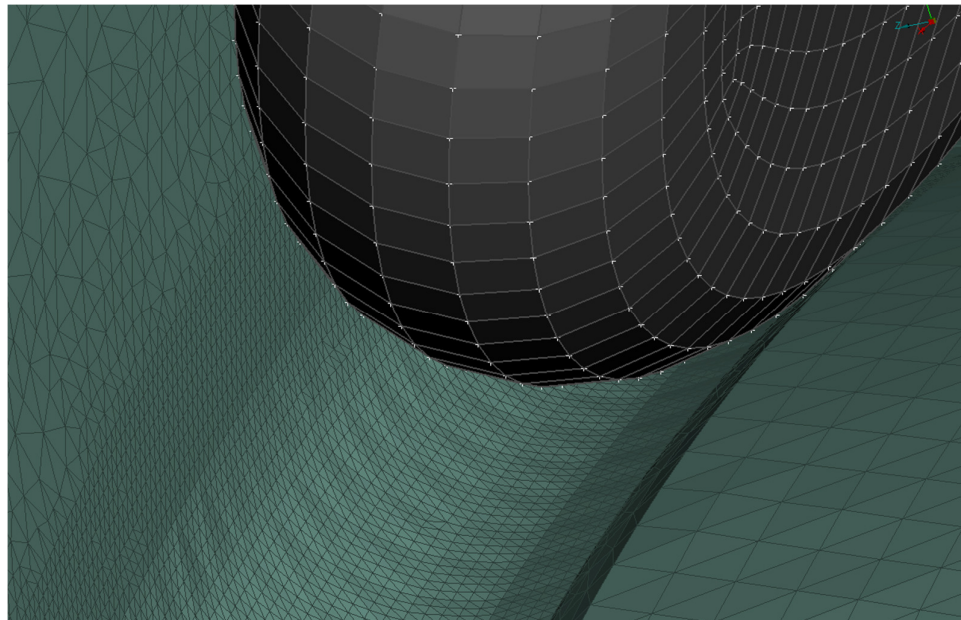


Figure 4.3 More detailed view of the roller and the fillet region at the contact area showing the varying element sizes.

4.1.2 Boundary Conditions and Analysis Steps

Rolling operation was simulated in the analysis in two steps; i) load application ii) crankshaft rotation under the applied load. The final roller removal process was ignored and results of the analysis were taken from the unaffected region from the roller at the end of the analysis.

The roller and defined local axis is shown on Figure 4.4. In step 1, translations of roller in y and z directions were fixed and in x direction was allowed. Rotations around three axes were fixed. In step 2, the same boundary conditions were used.

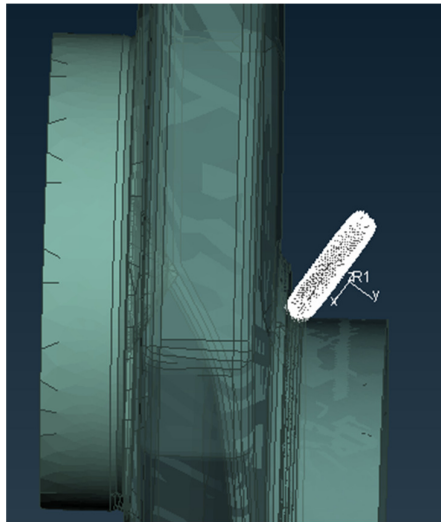


Figure 4.4 The roller and the local axis.

For the crankshaft section used, two reference points were defined on the two end planes of the section. Degree of freedom of two end planes were restricted at the center of these two planes to define the reference points. The reference point on the center of the pin journal was defined as R1 and on the center of

main journal as R2. Figure 4.5 and 4.6 define the reference points on the crankshaft section used.

For R1, translations in the all directions were allowed and rotations around all axes were fixed in step 1. In step 2, the same boundary conditions were used for the translations whereas rotation around x and y axes were fixed and around z axis was allowed.

For R2, translations and rotations in all directions were fixed in step 1. In step 2, translations in x and y directions were allowed and in z direction fixed. Rotations in all directions were allowed to define the rotation of the crankshaft around pin journal axis.

The summarized boundary conditions enabled to simulate the actual rolling steps.

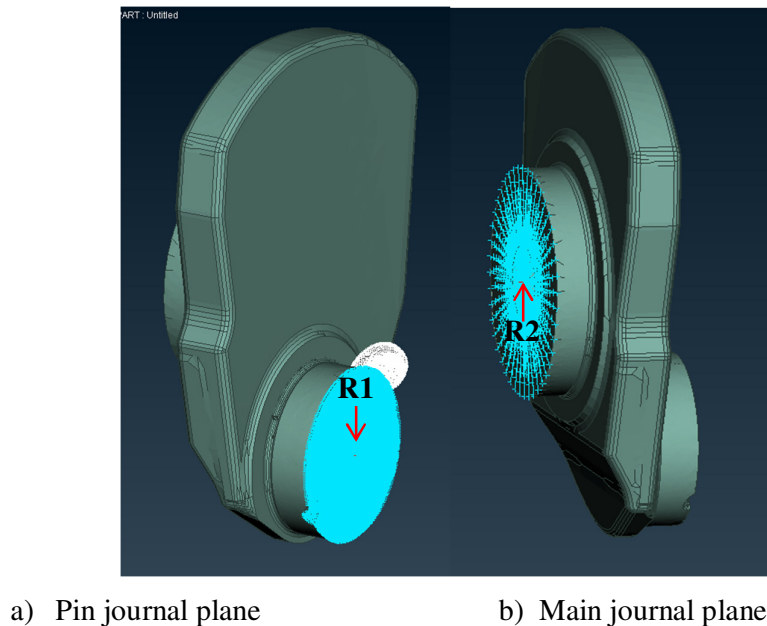


Figure 4.5 Crankshaft reference points for defining the boundary conditions.

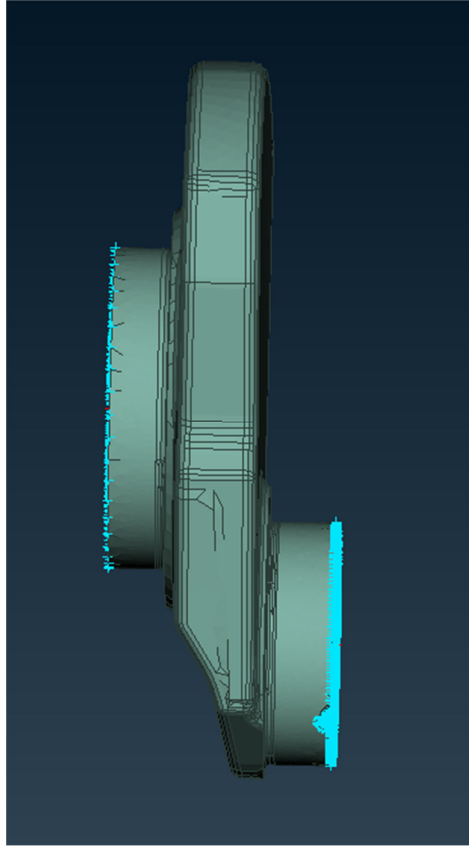


Figure 4.6 Crankshaft section and the end planes from side view.

4.1.3 Residual Stress Calculation Results

Figure 4.7 shows the stress contour along the rolling path representatively from the residual stress analysis of 38MnVS6 steel crankshaft rolled at 12.5kN. In order to represent the analysis results, crankshaft model is cut in a radial direction from the fillet region. From this cross-section, in the direction of rolling load; which is also the crack direction and 55° to the crankshaft axis; compressive residual stresses were derived through the depth. The path is shown on Figure 4.8. Figure 4.9 and 4.10 show the representative stress distributions on this cross-section under the applied load and after load removal conditions respectively.

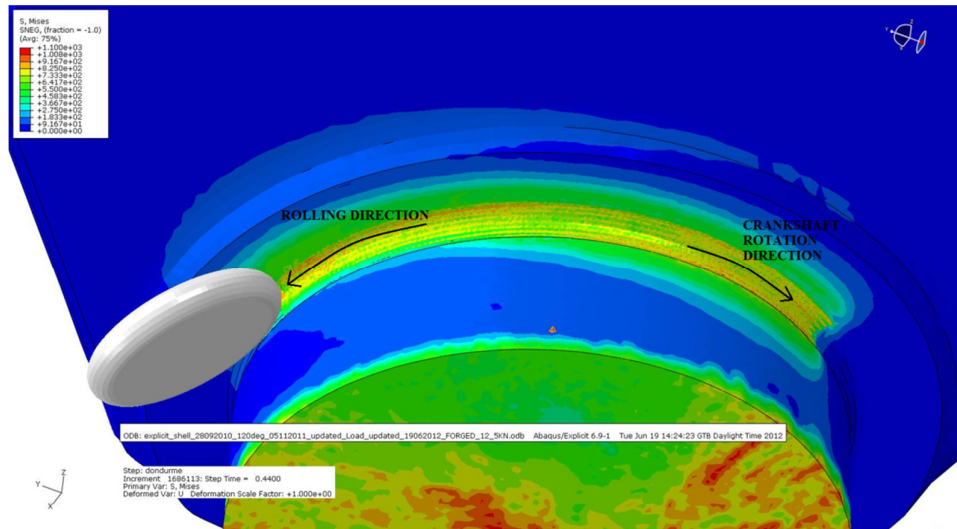


Figure 4.7 Stress contour along the rolling path.

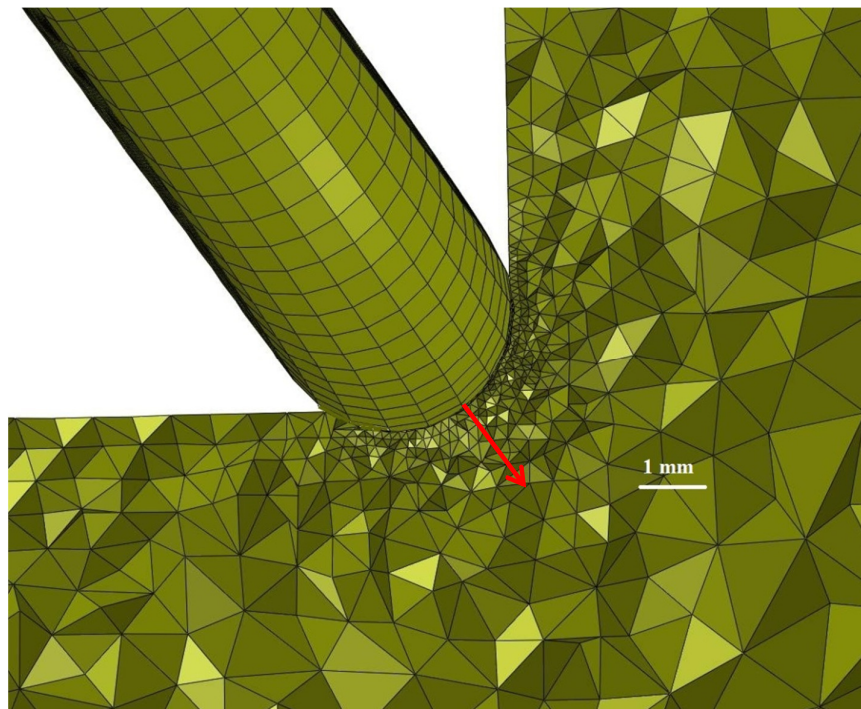


Figure 4.8 Residual stress reading direction.

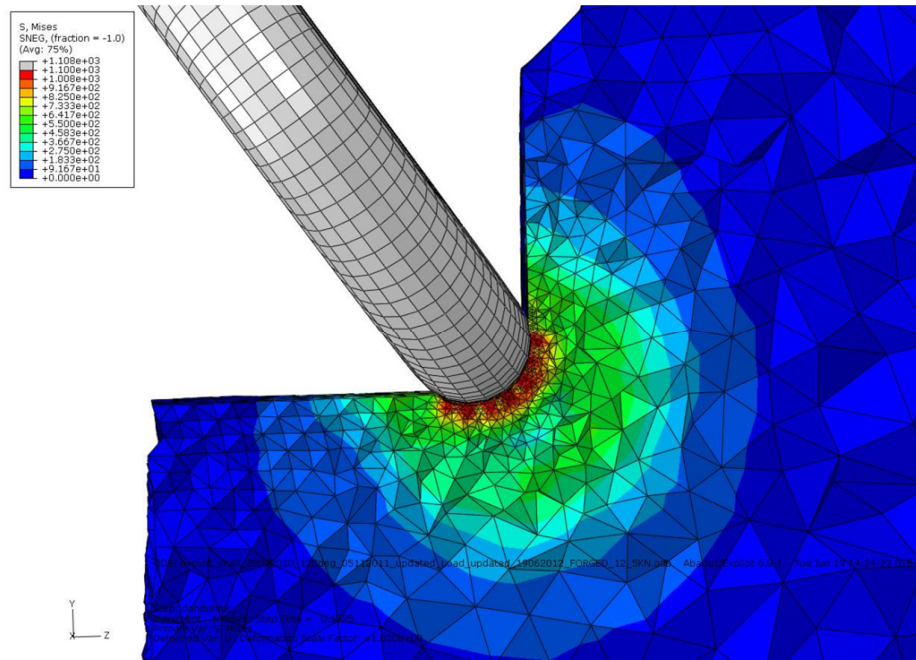


Figure 4.9 Stress contour on the crankshaft cross-section under rolling load.

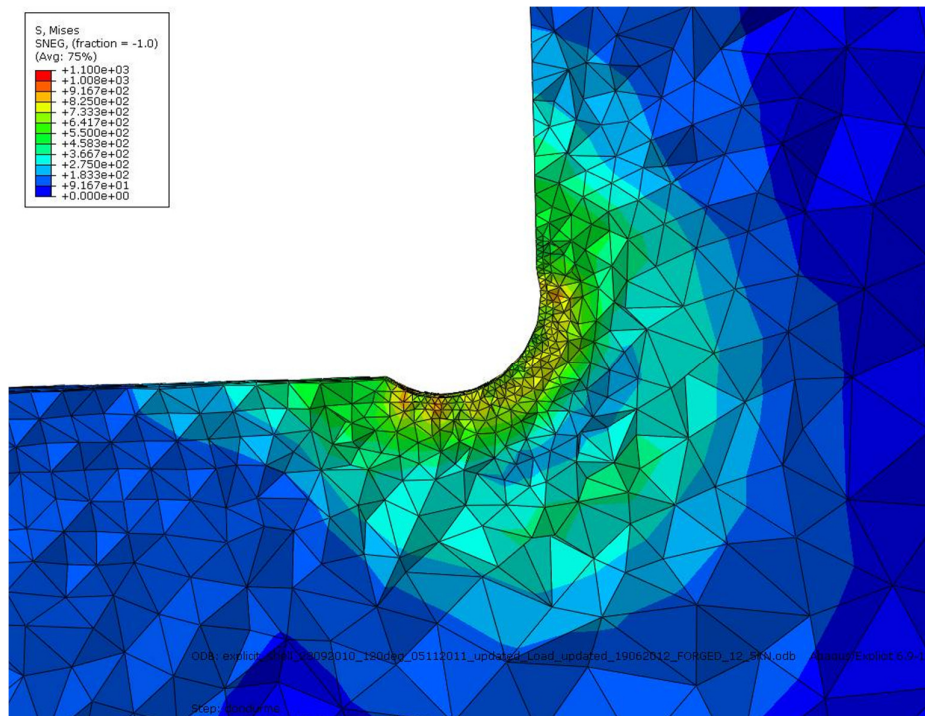


Figure 4.10 Stress contour on the crankshaft cross-section after load removal.

The stress profiles along the defined path, under the load and after load removal were shown on Figures 4.11 to 4.15 comparatively in order to demonstrate the unloading behavior.

The stresses through the depth remaining after load removal, that are compressive residual stresses are presented separately as well on Figures 4.16 to 4.20 with polynomial curve fits.

Discussion of the obtained results and their relationship to fatigue strength are conducted in the next chapter.

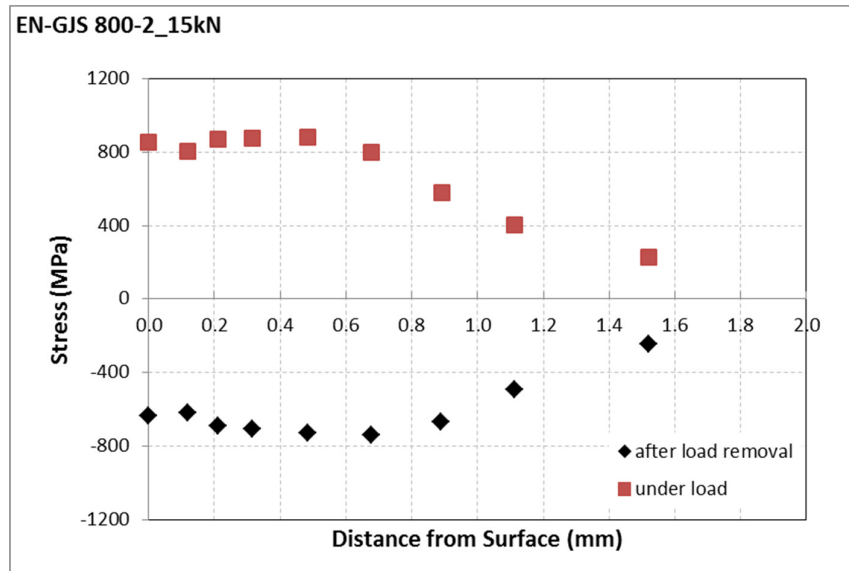


Figure 4.11 Stress profiles for EN GJS 800-2 crankshaft rolled at 15kN, under load and after load removal.

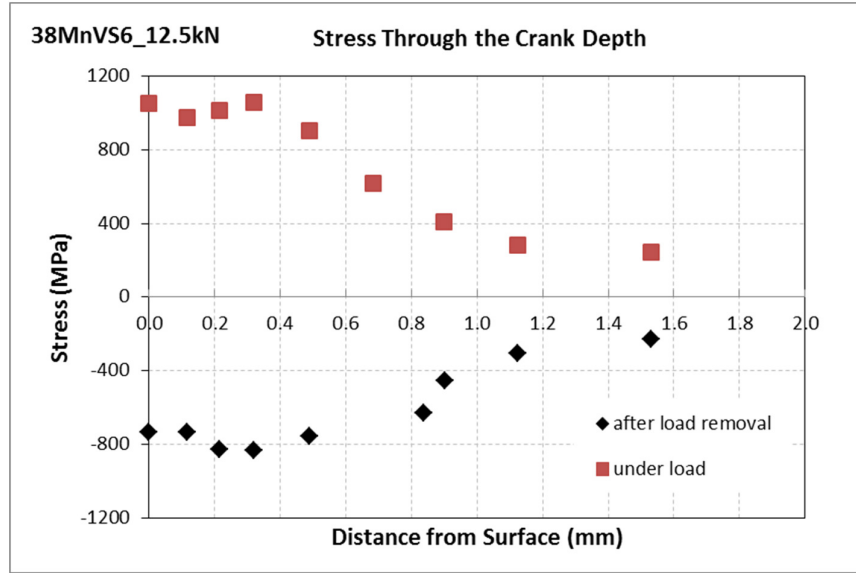


Figure 4.12 Stress profiles for 38MnVS6 crankshaft rolled at 12.5kN, under load and after load removal.

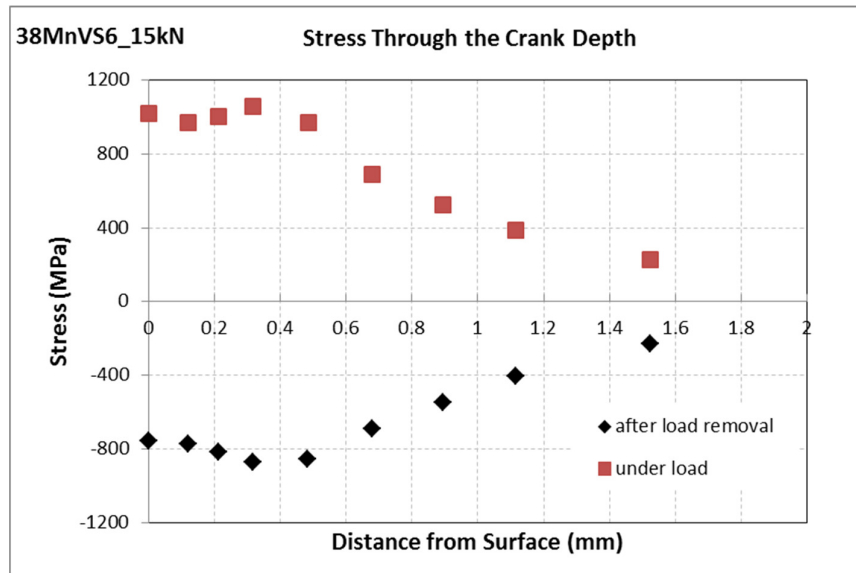


Figure 4.13 Stress profiles for 38MnVS6 crankshaft rolled at 15kN, under load and after load removal.

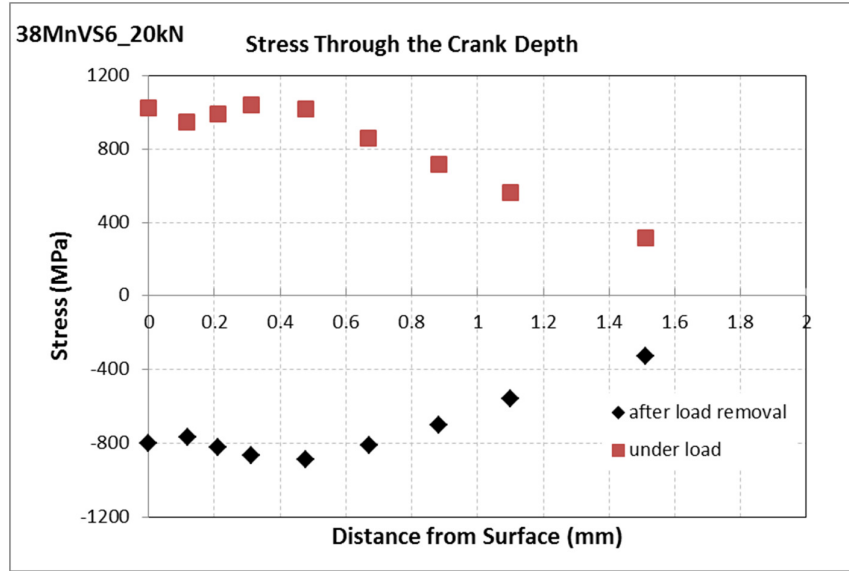


Figure 4.14 Stress profiles for 38MnVS6 crankshaft rolled at 20kN, under load and after load removal.

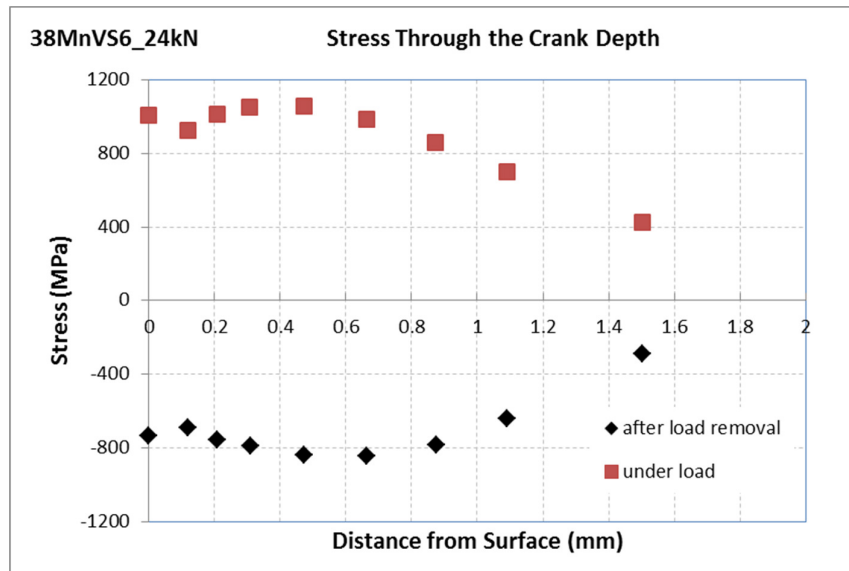


Figure 4.15 Stress profiles for 38MnVS6 crankshaft rolled at 24kN, under load and after load removal.

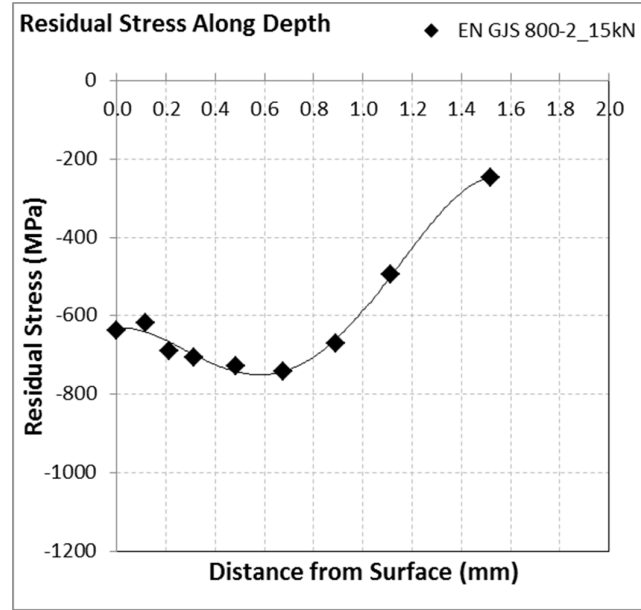


Figure 4.16 Residual stress profile for EN GJS 800-2 crankshaft rolled at 15kN.

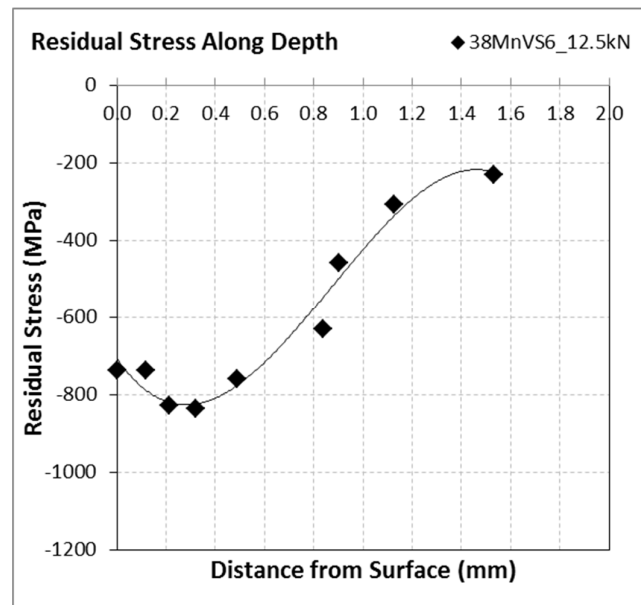


Figure 4.17 Residual stress profile for 38MnVS6 crankshaft rolled at 12.5kN.

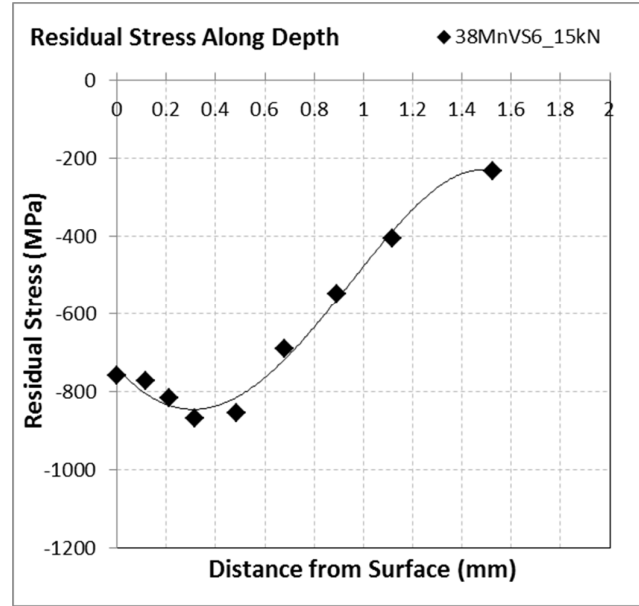


Figure 4.18 Residual stress profile for 38MnVS6 crankshaft rolled at 15kN.

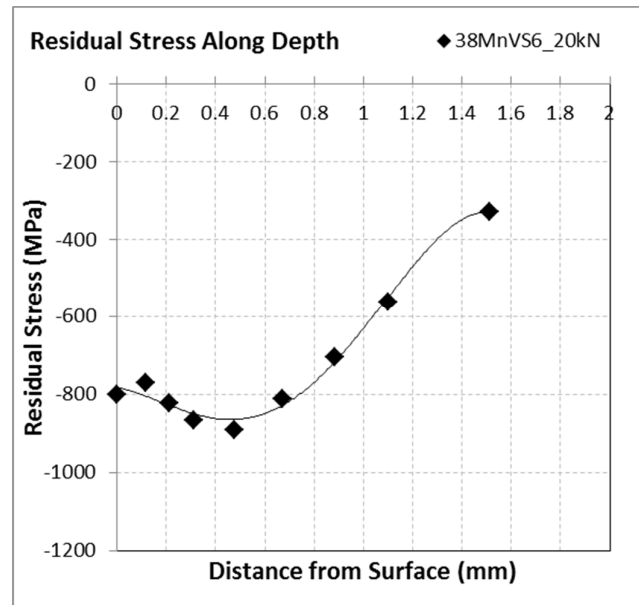


Figure 4.19 Residual stress profile for 38MnVS6 crankshaft rolled at 20kN.

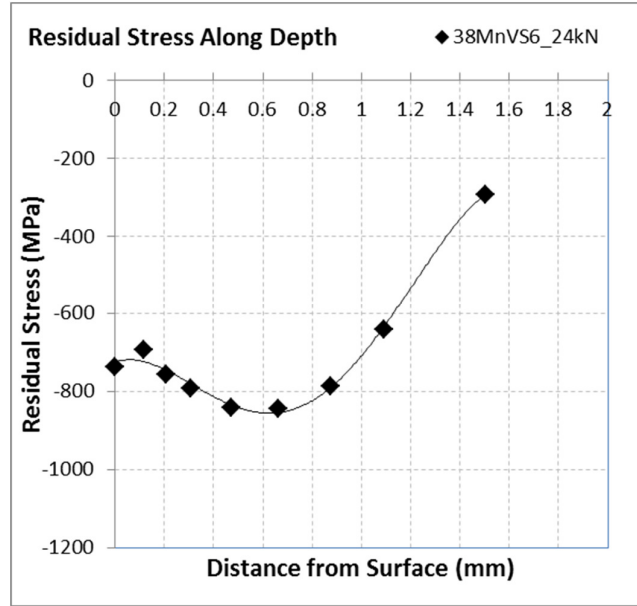


Figure 4.20 Residual stress profile for 38MnVS6 crankshaft rolled at 24kN.

4.2 Bending Test Stress Calculations

Due to complex geometry of the crankshafts, calculations of the stresses induced at the fillet region is complicated. In addition, due to the small size of the fillet region, a direct measurement of the stresses by strain gages is not possible at exactly on the fillets.

In order to calculate the induced stresses at the fillet region as a result of applied bending moments, a two-step procedure was utilized based on the fundamental rules and with the advent of computer aided analysis.

The maximum bending stress of a component can be calculated from the below formula [66];

$$\sigma_{max} = \frac{M.c}{I} = \frac{M}{Z} \quad (4.1)$$

where M is the bending moment, c is the vertical distance from neutral axis, I is the moment of inertia and Z is the section modulus.

The section modulus of the fillet region is a function of journal diameter, web thickness, web width simply. On the other hand, since the thickness is not uniform around the section, to define a value of Z is complicated.

In addition, a stress concentration is present at the fillet region due to the undercut geometry. The bending stress concentration factor at the pin journal fillets is defined as [67];

$$\beta_B = K\beta_B \cdot f_B(s, w) \cdot f_B(w) \cdot f_B(b) \cdot f_B(r) \cdot f_B(d_G) \cdot f_B(d_H) \cdot f_B(recess) \quad (4.2)$$

where

$K\beta_B$ is a dimensionless factor; $s = S/D$; $w = W/D$; $b = B/D$;
 $r = R_G/D$ $d_G = D_{BG}/D$; $d_H = D_{BH}/D$; $f_B(recess) = f(T_H, T_G)$;

and

D	crankpin diameter
S	pin overlap [$S = (D+D_G)/2-E$]
W	web thickness
B	web width
R_G	fillet radius of journal
D_{BG}	diameter of axial bore in journal
D_{BH}	diameter of axial bore in crankpin
T_H	recess of crankpin fillet
T_H	recess of journal fillet
D_G	journal diameter
E	pin eccentricity

These geometrical features are also described on Figure 4.21.

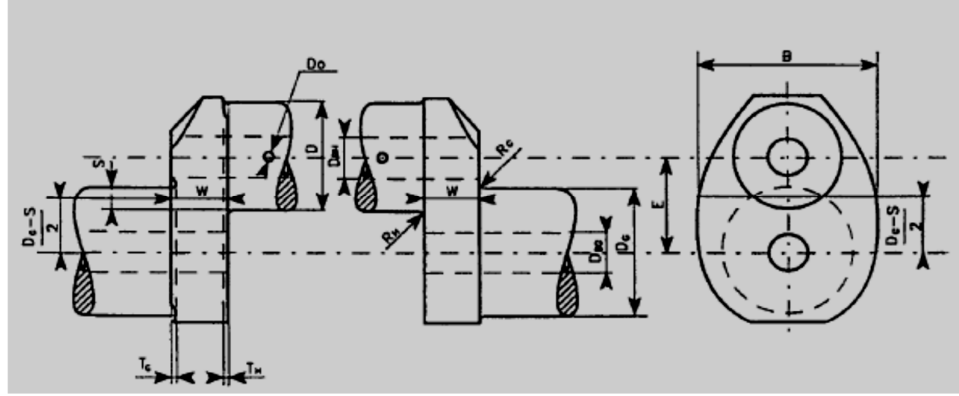


Figure 4.21 Crankshaft dimensions related to stress concentration factor at the fillet region [67].

With the motivation of the knowledge that both maximum bending stress and stress concentration factor are functions of crankshaft and fillet geometry, the stress value at the fillet region induced, as a result of applied bending moment in resonant bending fatigue tests, can be described as;

$$\sigma_{max,bending} = K \cdot M \quad (4.3)$$

where K is the geometric factor covering both the functions of crankshaft and fillet geometry and M is the applied bending moment. So it was proposed, within the frame of this study, that once the value of K is calculated, it can be used to calculate the stress values at the fillets for different applied moments, since the same geometry and loading mode is used throughout the tests.

For this purpose, a simulation of fatigue test rig was used, developed in a previous study by Finite Element Method [51]. By this method, a finite element

model developed by Hypermesh was used to conduct a linear elastic stress analysis in Nastran to obtain the stresses at the fillet region. Figure 4.22 shows the test rig model. The crankshaft and test rig used in the referenced study are the same as in the frame of this study.

Figure 4.23 shows a representative stress contour on the fillet region with the applied bending moment. As expected, the stress values are found to be maximum at the top center of the circular cross-section of the fillet rolled region. In consistence, the location of maximum stress is the crack initiation point observed on the crankshaft test samples.

From the applied moment value and calculated stress value by the test simulation, the factor K was calculated as 0.496. After running sufficient analysis for verification, applied test moments were used to calculate the corresponding stress values at the fillet region which were tabulated on Tables 3.13 to 3.19.

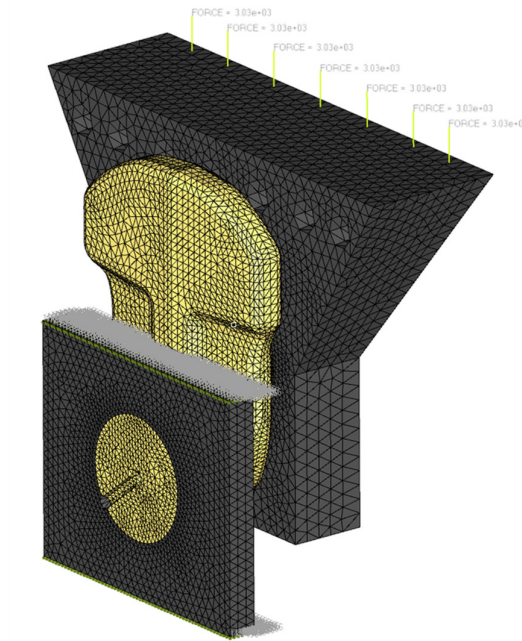


Figure 4.22 CAE model for the Resonance Bending Test [51].

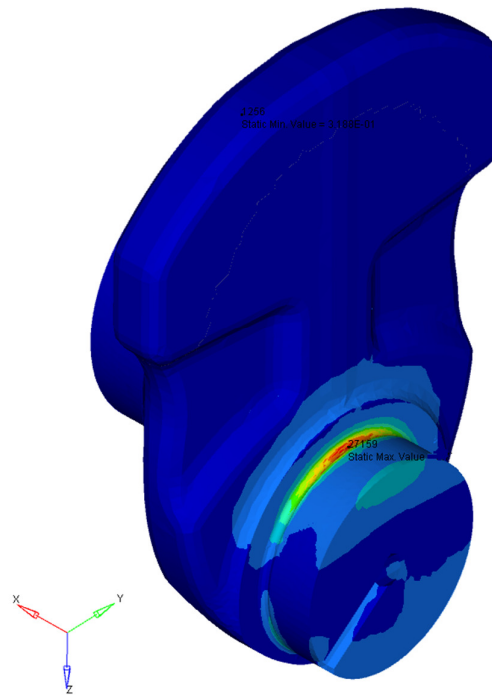


Figure 4.23 Representative stress contour at the fillet region [51].

CHAPTER 5

DISCUSSION

5.1 Methodology and Results

5.1.1 Resonance Bending Fatigue Tests

Resonance fatigue tests based on the frequency drop failure criterion provides time saving by the advance of early crack detection without waiting for the two-piece failure of the components. For this purpose, frequency shift limits of the tests are generally set at frequencies lower than 1% of the resonance frequency and any visible crack is accepted as failure criterion. In this study, with aim of obtaining S-N curves covering both the crack formation and the crack propagation stages, a relatively larger frequency shift limit of ± 4 Hz was selected as failure criterion which is approximately 10% of the resonance frequencies of the cast iron and steel crankshaft samples. The measured resonance frequencies of the test systems with the cast iron and steel crankshafts are 35Hz and 40Hz respectively. As a result of this approach, macroscopically visible cracks were observed on the test samples; moreover nine two-piece failures occurred at rolled cast iron crankshaft samples at high testing loads.

In order to comment on the frequency and test load variation throughout resonance frequency testing, representative frequency, load amplitude, mean test load versus number of cycles curves were constructed and demonstrated on Figures 5.1 to 5.3.

On Figure 5.1, it can be derived that, after stabilization of the frequency at beginning of the test, the frequency stays constant for a certain number of cycles after which, a linear frequency drop with number of cycles is observed. This linear decrease in frequency can be attributed to crack propagation at a constant rate. After this, an accelerated decrease is observed on frequency which reaches the frequency limit of $\pm 4\text{Hz}$ where the test terminates.

Based on the mechanical stiffness theory, and the crack propagation laws, it can be stated that the stable frequency region can roughly be accepted as covering the crack initiation and stage I crack propagation regions which is indicated as Region I on Figure 5.1. Similarly, the Region II on the same figure can be accepted as the Stage II, stable crack propagation region whereas region III corresponds to unstable crack propagation region, Stage III. It should also be noted that unstable crack propagation is induced after approximately 1 Hz frequency drop. Figures 5.2 and 5.3 show the uncontrolled increase in the load amplitude and mean stress at the final failure point which correlates well with the final frequency drop on Figure 5.1. These findings show that the frequency limit of $\pm 4\text{ Hz}$ is a well-defined value to monitor the final fracture stage.

For exact correlation with the test frequency profile with number of cycles, a detailed investigation can also be conducted by correlation of the crack size; with the test frequency which is out of the scope of this study.

In section 3.5, on Figure 3.70, the fracture surface of a ductile cast iron crankshaft sample was demonstrated showing the crack initiation, propagation and final fracture regions which also explains that both crack initiation and propagation stages were captured throughout the tests.

Depending on the findings discussed in this section , it can be concluded that using a frequency limit of 10% of the resonance frequency enables to successfully obtain complete S-N curves of the crankshafts including both crack initiation, propagation and final fracture stages.

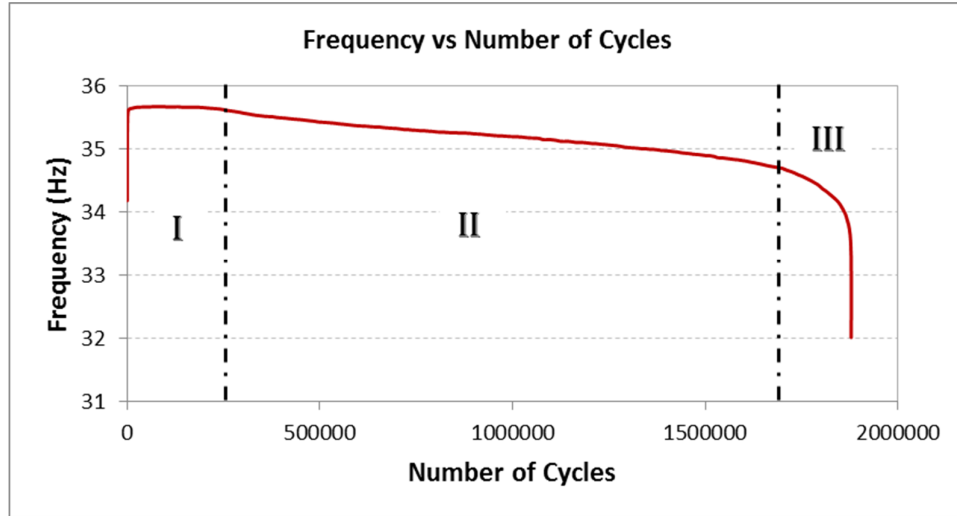


Figure 5.1 Frequency change with number of cycles throughout testing of un-rolled EN-GJS 800-2 crankshaft tested under 8.25kN load amplitude.

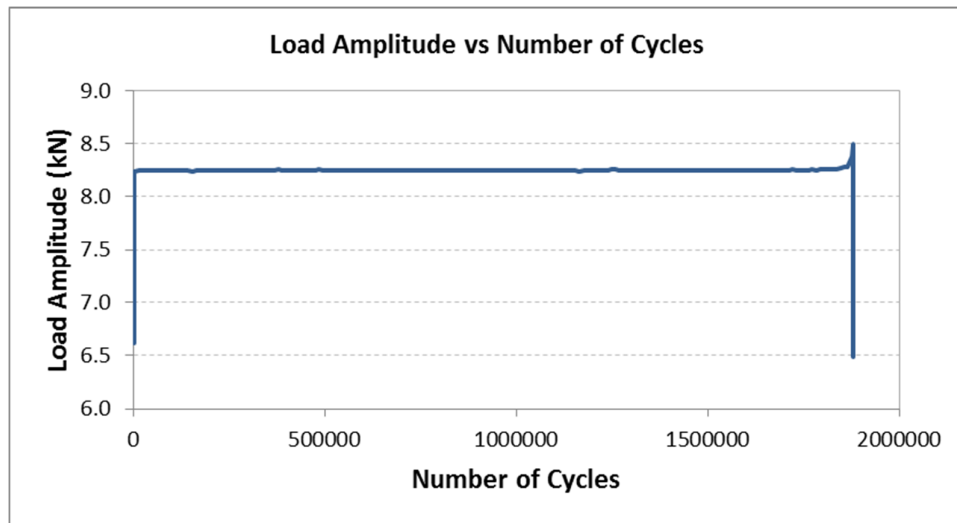


Figure 5.2 Load amplitude versus number of cycles throughout testing of un-rolled EN-GJS 800-2 crankshaft tested under 8.25kN load amplitude.

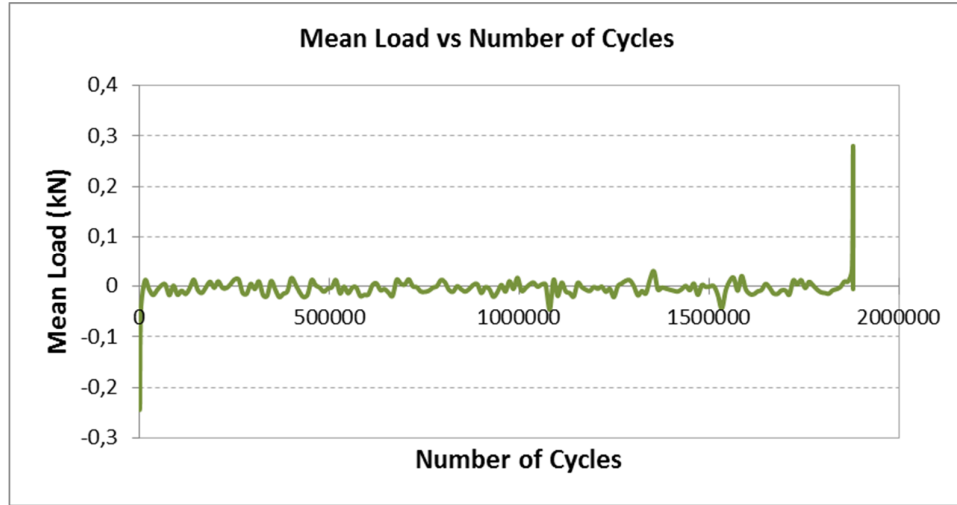


Figure 5.3 Mean load versus number of cycles throughout testing of un-rolled EN-GJS 800-2 crankshaft tested under 8.25kN load amplitude.

5.1.2 Staircase Test Methodology

In this work, test plan according to staircase test methodology was utilized to obtain the data for S-N curves. By selection of the test loads according to this methodology, relatively low number test samples were used compared to conventional S-N test methods. In addition, the transition regions of the S-N curves were successfully captured with small sample sizes as described by the failure-runout histories on Figures 3.33 to 3.39.

In addition, statistical analyses have successfully been conducted with the obtained test data to estimate the fatigue limit and to construct the S-N curves.

The stress increment of 8.20MPa used throughout the tests has been found successful to run the statistical analysis, calculate the fatigue limit and construct the S-N curves. Using a lower stress increment of 3.28MPa for ductile cast iron crankshafts rolled at 15kN has enabled to overcome the

variations coming from rolling process and casting process itself and obtain a smooth S-N curve for the analysis.

Based on the experiences obtained within the frame of this study, staircase test methodology was found successful for accelerated fatigue testing of engineering components because of its conveniency to apply and valuable data it supplies for statistical analysis.

5.1.3 Fractographic Analyses

Fractographic analyses were conducted on the failed crankshaft samples in order to shed light on the failure characteristics of the crankshafts.

By macroscopic examination of the test samples, it was observed that approximately the same crack direction and angle to the crankshaft axis were observed on all test samples. It was also observed that the crack starts at the crank pin fillet region and propagates towards the free end of the section following a path of approximately 55° to the crankshaft axis. This path reflects the failure direction also observed in service failures of the crankshafts. According to the crankshaft geometry, the fracture plane on this orientation has the smallest cross-section where torsional, bending and normal forces are effective. This explains the reason of selecting this angle typically in rolling operation of the crankshafts to improve mechanical durability [61].

Another finding of the fractographic analyses is that multiple crack initiation sites are effective on both ductile cast iron and steel crankshaft samples in the fillet region which is an expected phenomenon since stress concentration is present at the vicinity of the undercut radius of the crankshaft. Presence of secondary cracks was also observed on the steel crankshaft samples which is also an outcome of the high stress concentration at the area of concern.

As explained in section 5.1.1., selected test conditions has provided covering the unstable crack propagation region in addition to the stage I and II crack propagation regions during the tests. The crack initiation, propagation and final fracture regions were summarized on Figure 3.70 representatively on a fully fractured ductile cast iron crankshaft sample.

The crack initiation region on a ductile cast iron crankshaft test specimen monitored by SEM reveals that graphite nodules near or open to the surface can serve as stress concentration points and can de-bond from the pearlite matrix under loading. Thus, graphite nodules can be accepted as potential fatigue crack initiation sites. In addition, for both ductile cast iron and steel crankshafts, any surface irregularity residual from the machining process or microscopical features (such as grain boundaries, graphite nodules in ductile cast iron crankshafts or MnS in steel crankshafts) can selectively serve as fatigue crack initiation sites at the fillet region.

Characteristic features of fatigue crack propagation, the striations, were observed on SEM analysis of steel crankshaft samples. Cleavage planes were also observed on the fast fracture region of the steel crankshaft fracture surfaces which shows the brittle-type of failure. On the ductile cast iron crankshafts, although macroscopic characteristics were well-visible on the fracture surface, striations could not be differentiated on SEM.

5.1.4 Test Stress Calculations

In order to calculate the stresses induced at the fillet region, as a result of applied bending moments during the tests, the test rig was simulated by finite element method. Since the stress developed at the fillet region is a function of crankshaft and fillet geometry which is same for all the test conditions, a factor, covering both the effect of geometry and stress concentration, was calculated from the analysis data. By using this factor, corresponding stress values to the applied bending moments were calculated successfully.

This approach has provided to build a time saving know-how on the fatigue strength studies of the crankshafts since in literature the component-based fatigue test data are usually demonstrated as bending moments to cycles; or stress values can be measured not exactly at but near to the fillet due to geometrical inconveniency.

5.1.5 Residual Stress Calculations by Finite Element Method

Residual stresses at the fillet region were calculated through the depth successfully by the three-dimensional dynamic simulation of the rolling process. Using a small size of mesh of 0.1mm has provided an effective resolution to monitor the residual stresses up to 1.5mm depth. By the use of obtained data, residual stress variation through the depth has been successfully determined up to the defined depth. On the other hand, further valuable data could not be obtained due the increasing mesh size after this value. An increased mesh size was preferred at certain distance from the fillet region to avoid from long analyses durations. With the used mesh profile, duration for one analysis was recorded as about 3 days.

Using the experimentally determined true stress-strain data, the kinematic hardening rule was applied in the elastic-plastic model for the calculations.

According to the residual stress profiles summarized on Figures 3.16 to 3.20, the general trend is that the residual stress value increases initially and then decreases through the depth from surface to the crankshaft center. This profile has been obtained in various other investigations on the residual stress calculations at the fillet region of crankshafts [58, 61, 68].

Results of residual stress analyses are summarized on Table 5.1. On this table, maximum residual stresses, depth of peak (maximum) residual stresses, effective depth at 500MPa are listed in addition the induced maximum residual stresses under the applied load for all design cases. The residual stress profiles

for ductile cast iron and steel crankshafts are shown on the same graph on Figure 5.4. Figure 5.5 shows the residual stress profiles on steel crankshafts rolled at different loads. Figure 5.6 shows only curve fits of residual stress profiles shown on Figure 5.5 in order to be able to differentiate the residual stress profiles for different loading conditions in more detail.

Table 5.1 Summary of residual stress analysis.

Crankshaft Material	Rolling Load (kN)	Maximum Stress Under Load (MPa)	Maximum Residual Stress (MPa)	Depth of Peak Residual Stress (mm)	Effective Depth at 500MPa Residual Stress (mm)
EN-GJS 800-2	15	884	-742	0.68	1.11
38MnVS6	12.5	1057	-836	0.32	0.90
38MnVS6	15	1055	-870	0.32	0.98
38MnVS6	20	1038	-890	0.48	1.17
38MnVS6	24	1057	-845	0.66	1.24

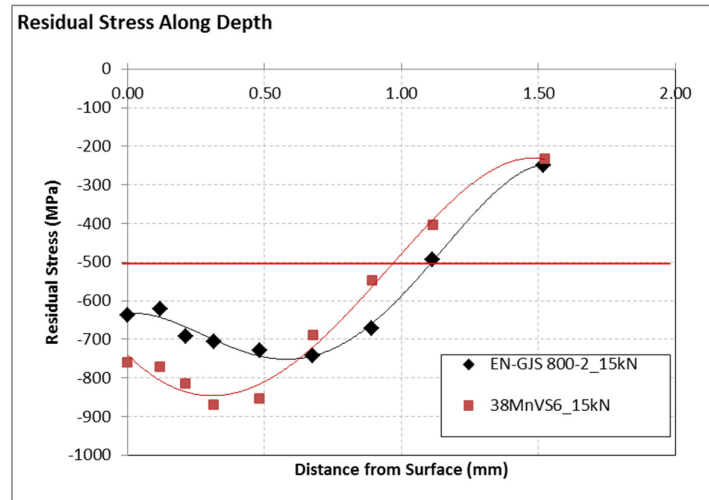


Figure 5.4 Comparison of residual stress profiles of EN-GJS 800-2 and 38MnVS6 crankshafts fillet rolled at 15kN.

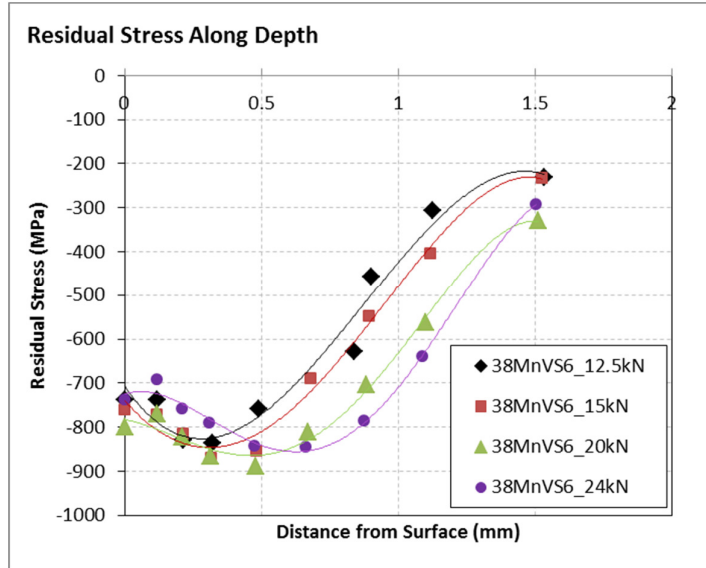


Figure 5.5 Comparison of residual stress profiles of 38MnVS6 crankshafts fillet rolled under different loads.

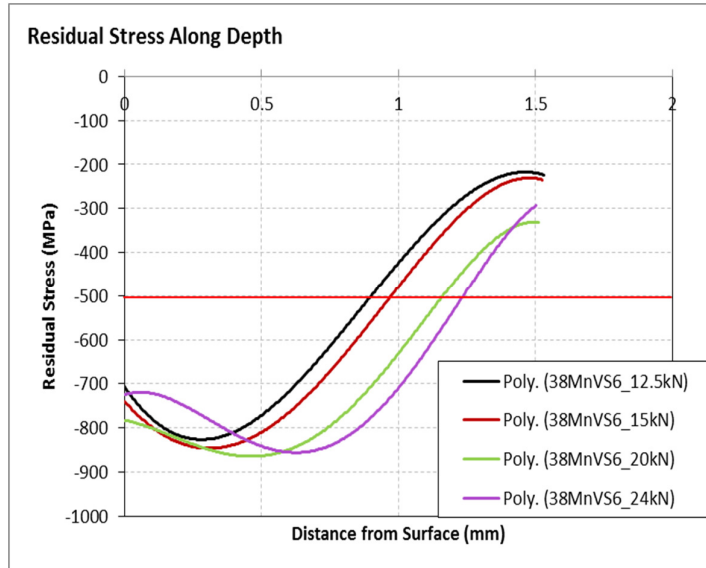


Figure 5.6 Polynomial fit residual stress profiles of 38MnVS6 crankshafts at different rolling load conditions.

The maximum (peak) compressive residual stress for EN-GJS 800-2 crankshaft rolled at 15kN was found to be 742MPa at a depth of 0.68mm. Residual stress calculations, on the 38MnVS6 crankshafts rolled under the same load, showed a maximum residual stress value of 870MPa at a depth of 0.32mm. In order to compare the effectiveness of residual stresses in more detail, the depths at which 500MPa residual stress is present, were also compared for each design condition. 500MPa was arbitrarily selected within the linear region of residual stress curves. For the cast iron crankshaft rolled at 15kN, 500MPa of residual stress is present at a depth of 1.11mm where the same residual stress value was observed at 0.98mm for steel crankshaft. Thus it can be stated that, although a higher amount of residual stress is developed in steel crankshaft, effective depth of residual stress is higher on ductile cast iron crankshaft, rolled under the same load, until 1.5mm depth. Approximately at 1.5mm, similar values of residual stresses were observed in both material type of crankshafts.

From Table 5.1, and Figure 5.6 it can be derived that while depth at peak residual stress, for 12.5 and 15kN rolling load conditions, is nearly equal for steel crankshaft; as the rolling load is increased to 20 and 24kN, maximum residual stresses were observed at higher depth values. In addition, increased rolling load results in achieving a 500MPa of residual stress value at higher depths. From 15kN to 20kN rolling load conditions, peak compressive residual stress values increase with the increasing rolling load. The difference between the minimum and maximum obtained residual stress is 6.5% for steel crankshafts rolled at different loads. For 24kN load, a lower residual stress value was calculated than that of the 20kN condition. An argument can arise at this point; with shifting of the maximum stress value to higher depths at higher loads, the peak residual stress may decrease at an amount. On the other hand, the increasing mesh size through the depth may result in such a deviation as well.

From the data obtained by residual stress analysis of steel crankshafts rolled at different rolling conditions, it can be summarized that; although increase in

peak residual stress with the increasing rolling load is not significantly high, main effect of increased rolling load is the increased effective depth of residual stress.

In order to comment on the success of the residual stress analysis, a comparison on the true-strain curves of the materials was also conducted by applying the stress values induced under the applied loads as listed on table 5.1. As a result of this analysis, which is based on loading-unloading rule on the true stress-strain curve, one would expect maximum residual stress values of 852, 1042, 1040, 1029 and 1042MPa respectively (in the order of increasing rolling load). The loading-unloading profiles are illustrated on Figure 5.7 and 5.8. As listed on Table 5.1, lower values were obtained from the finite element calculations. However, this difference is acceptable, and moreover realistic, since the rolling operation is locally applied at the fillet region and the affected region is surrounded with a large mass which is unaffected from the rolling process; an amount of residual stress relief is expected.

Although residual stress calculations and measurements for crankshaft geometries are limited in literature with same crankshaft material and rolling loads used in this study, a comparison of residual stress value for ductile cast iron crankshaft was conducted with the results of the work conducted by Spiteri et.al [58]. Spiteri et.al. have calculated the residual stress profile of a ductile cast iron crankshaft with a similar material fillet rolled at 6kN. According to this study, the maximum compressive residual stress was calculated as 800MPa at 0.25mm from the surface of the crankshaft, approximately at the direction of rolling. The value of residual stress is comparable to 742MPa calculated for EN-GJS 800-2 crankshaft fillet rolled at 15kN within this study. When the effective residual stress depths are compared, a lower depth 0.25mm was measured by Spiteri whereas the depth was calculated as 0.68mm in this study. However, this behavior is expected since it was derived that increased rolling load yields in the depth value at which maximum compressive residual stress is observed in this section.

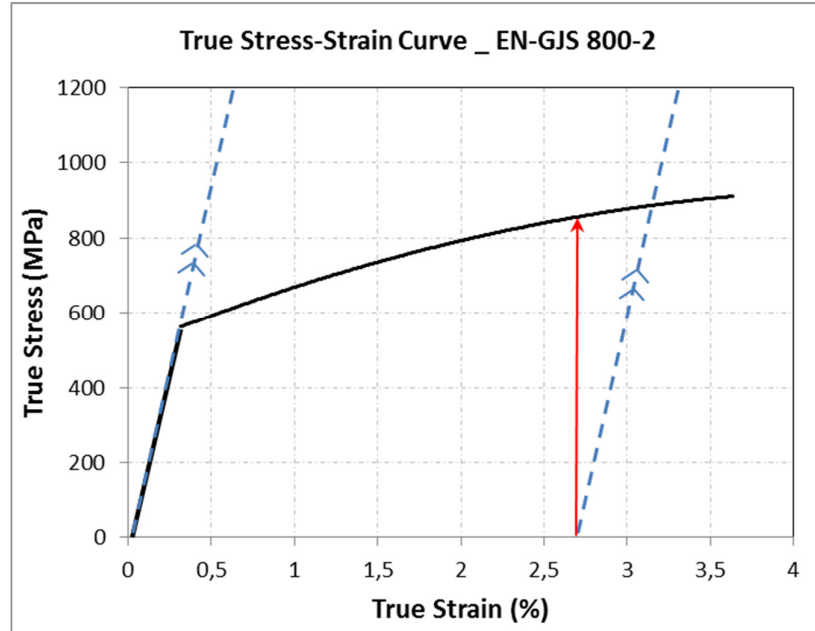


Figure 5.7 Loading-unloading simulation of rolling process on true stress strain curve for EN-GJS 800-2 crankshaft.

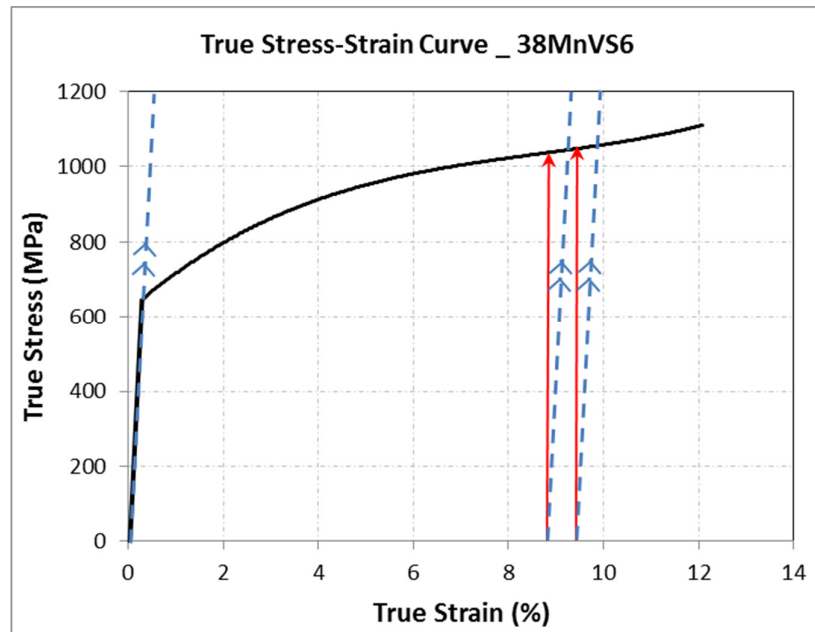


Figure 5.8 Loading-unloading simulation of rolling process on true stress strain curve for 38MnVS6 crankshaft.

5.1.6 Statistical Analyses

This section aims to discuss the outcomes of the curve fitting and fatigue limit calculations by statistical analyses. Analysis results for Dixon-Mood calculations were tabulated on Table 3.20. Results of Normal and Weibull distribution calculations, Modified Basquin Model and Random Fatigue Limit Model by the use of Maximum Likelihood Estimation method were shown on Tables 3.21 to 3.29.

5.1.6.1 Curve Fit Methods

In the frame of this study, two curve fitting methods based on the Maximum Likelihood Estimation were used; namely Modified Basquin and Random Fatigue Limit. Both methods were applied successfully to fit the experimental data and construct the P-S-N curves of the design conditions which are the subjects of this study. In addition to the median curve of 0.5 probability, 0.1, 0.05, 0.01, 0.9, 0.95 and 0.99 probability curves were also plotted on the P-S-N diagrams.

P-S-N curves demonstrated in section 3.4.2.2, show that RFL model provides a better fit in test data in comparison to Modified Basquin Model. However this is an expected result since Modified Basquin model has three independent curve fit parameters whereas RFL model has five. The RFL model successfully captures the curvature of the S-N curve at the transition region. This is also reflected on the Maximum Likelihood values. In all cases, the calculated Maximum Likelihood values are higher for RFL model calculations which describes a higher likelihood of the curve fitting. In addition, as seen from the S-N curves at different probabilities, a narrower S-N band, is present in RFL model fit with respect to Modified Basquin model fit. The same profile of RFL and Modified Basquin model fits was observed on all of the material and design conditions.

Larger P-S-N bands were observed in the 38MnVS6 steel crankshafts, processed at 20 and 24kN rolling loads, with respect to the other conditions. The bands are even larger for 24kN rolling load condition. However, this is an expected result since larger scatter in test data is present for these two design conditions. With the increasing rolling load, probability of surface micro-crack formation increases due to the local plastic deformation at the fillet region which may result in data scatter on the S-N plots. This argument will further be discussed in section 5.2.2.

5.1.6.2 Fatigue Limit Calculations

Results of Dixon-Mood analysis were shown on Table 3.20. Calculated mean endurance limit, standard deviation and lower and upper endurance limits for 90% confidence were listed on this table. Since a lower test stress increment was used, a lower standard deviation was obtained for EN-GJS 800-2 crankshafts rolled at 15kN. Ratio of stress increment to standard deviation for all test conditions are 1.89 which is within the range of 0.5 to 2.0 where Dixon-Mood equations are based on.

It was observed that higher mean fatigue strength values were calculated by Dixon-Mood method compared to values calculated by the other methods in all cases. When these values are compared on the S-N curves constructed by RFL model, which provides a good fit on the test data; it can be derived that fatigue limit calculation by Dixon-Mood method yields in overestimating the fatigue limit.

The fatigue strength distributions were demonstrated on probability density function and cumulative distribution function curves in section 3.4.2.2. From the probability density function curves and tabulated data on Tables 3.21 to 3.27, it can be derived that Normal and Weibull distribution analyses result in obtaining higher mean and median fatigue strengths in comparison to Modified Basquin and RFL analysis. Same type of profiles were observed on all test

conditions except for the 38MnVS6 crankshaft rolled at 20kN where a slightly higher median fatigue limit was calculated by RFL method. In all test conditions, pdf curves are shifted to lower fatigue limits in Modified Basquin model since the curvature of S-N curve could not be properly captured by this method.

Weibull and Normal distributions, in comparison to Basquin and RFL methods, show lower variance around the calculated fatigue limits whose pdf curves are narrower and maximum pdf values are higher. In all test conditions, pdf curves of Weibull distribution assumption is narrower in comparison to Normal distribution; and similarly RFL model gives a better distribution than the Modified Basquin model. The same comparative behavior with narrower cdf curves for Weibull model can also be derived from the cumulative distribution function curves for all cases.

When the standard deviations are compared (Tables 3.21 to 3.27), the general behavior is; values decrease in the order of Modified Basquin, RFL, Dixon-Mood, Normal and Weibull methods. The exceptions are; a higher standard deviation was obtained by Weibull method than by the Normal distribution method in 38MnVS6 crankshaft at unrolled condition and 12.5kN rolling condition; and standard deviation obtained by the RFL method is higher than obtained by the Modified Basquin method for 38MnVS6 crankshaft rolled at 15kN.

As shown on Tables 3.21 to 3.27 and described in section 5.1.6.1, it was observed that higher maximum likelihood values were obtained by RFL method than the Modified Basquin method. Likelihood values of RFL method are, as a general trend, even higher than Normal and Weibull distributions except three cases; EN-GJS 800-2 rolled at 15kN and 38MnVS6 rolled at 20 and 24kN.

As a conclusion of curve fit and fatigue limit calculations by statistical analysis; the RFL model is an effective method for fatigue data analysis since it provides a good curve fit and fatigue strength calculation with higher likelihood with respect to Modified Basquin model. Thus, the median fatigue curves, with 50% probability, obtained by RFL method were selected for usage to compare the fatigue behavior of different crankshaft design conditions in the following sections.

5.2 Discussion of the Effect of Fillet Rolling Process on Fatigue Performance

5.2.1 Comparison of Fatigue Performances of Ductile Cast Iron and Steel Crankshafts

Superposed RFL S-N curves of ductile cast iron and steel crankshafts at the unrolled condition are shown on Figure 5.9. As can be derived from this curve, ductile cast iron crankshaft shows better fatigue performance than the steel crankshaft. Median fatigue limit for ductile cast iron was measured from RFL data is 193.60MPa whereas that of steel crankshaft is 152.70MPa. EN-GJS 800-2 crankshaft shows a 27% higher fatigue strength than 38MnVS6 crankshaft at the unrolled state.

The base material fatigue strengths of EN-GJS 800-2 and 38MnVS6 obtained by standard fatigue tests are listed as typically 304MPa and minimum of 330MPa respectively in literature [62 and 69]. From here, fatigue limit reduction factor of the two materials were calculated as 1.57 and at least 2.16 respectively for the cast iron and steel crankshafts. The reduction of the fatigue strength of materials is directly related with the crankshaft geometry; since a stress concentration is present at the test location which can be defined as a corner. In addition, the machined undercut behaves like a notch as its radius can be regarded as notch radius and its depth as notch depth.

The higher amount of fatigue strength reduction of the steel crankshaft than the ductile cast iron can be well explained with the different notch sensitivities of two materials. It is a well-known fact that notch sensitivity of steel is higher than ductile cast iron; and with the presence of a notch, while under static loading conditions the strength of steel increases, under fatigue loading the strength decreases. Ductile cast iron's static and fatigue strengths are less affected with the presence of a notch due to its low notch sensitivity [70].

It should also be noted from Figure 5.9 that the difference between fatigue curves of two materials becomes narrower at low stress values, i.e high cycle fatigue region.

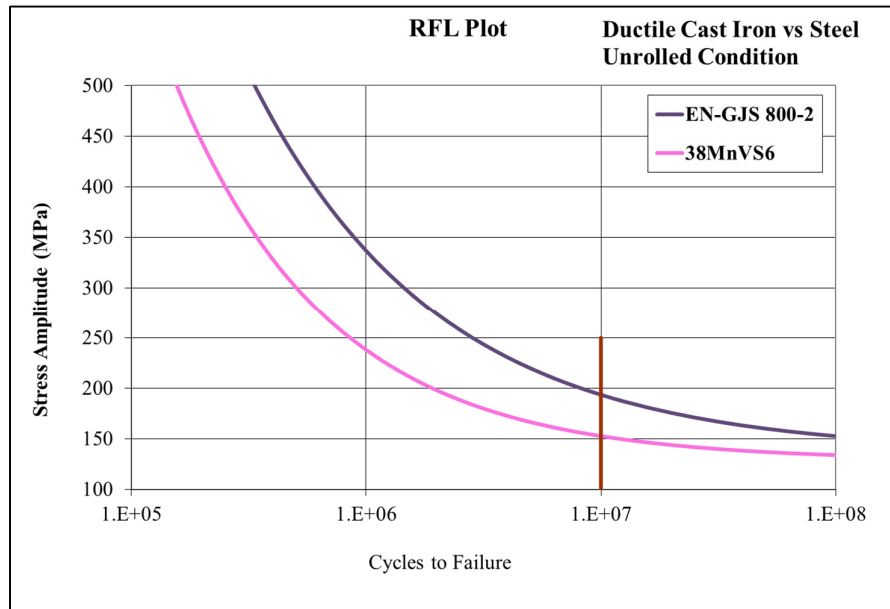


Figure 5.9 S-N curves of EN-GJS 800-2 and 38MnVS6 crankshafts at unrolled condition.

Figure 5.10 shows the S-N curves of crankshaft from two material types, fillet rolled under 15kN rolling load. As seen from these curves, while steel crankshaft fails at higher number of cycles in low cycle region; at high cycle fatigue region, a lower amount of stress is required for failure at the same number of cycles. This behavior is opposite to the behavior observed at the unrolled condition.

Figures 5.11 and 5.12 show the S-N curves at the unrolled condition and 15kN fillet rolled condition for ductile iron and steel crankshafts respectively. The measured median fatigue strengths are 806.74MPa and 793.36MPa respectively for fillet rolled ductile cast iron and steel crankshafts. At same fillet rolling conditions, EN-GJS 800-2 crankshaft showed 1.6% higher fatigue strength than 38MnVS6 crankshaft. The difference in fatigue strength is lower than the difference measured at the unrolled condition. From the data, fatigue strength improvement factors of 4.16 and 5.20 were calculated for ductile cast iron and steel crankshafts respectively when the same fillet rolling load is applied to both material types. This means that a higher amount of improvement is achieved with steel crankshaft with the same rolling conditions. The higher plastic deformation capability of steel is one of the most important reasons to observe this behavior. The higher ductility and strain hardening capacity of the steel was measured by the tensile tests within the frame of this study. This fact is further supported with the comparison of deformation characteristics of two materials in section 5.3. Another primary factor leading to this result is the amount of compressive residual stresses developed on the steel crankshaft fillet region is higher as discussed in section 5.1.5.

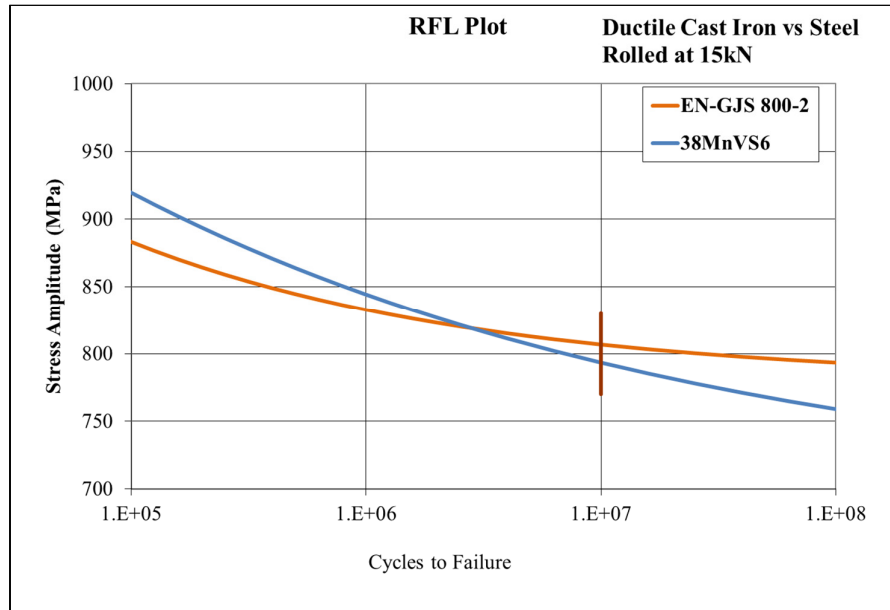


Figure 5.10 S-N curves of EN-GJS 800-2 and 38MnVS6 crankshafts fillet rolled under 15kN rolling load.

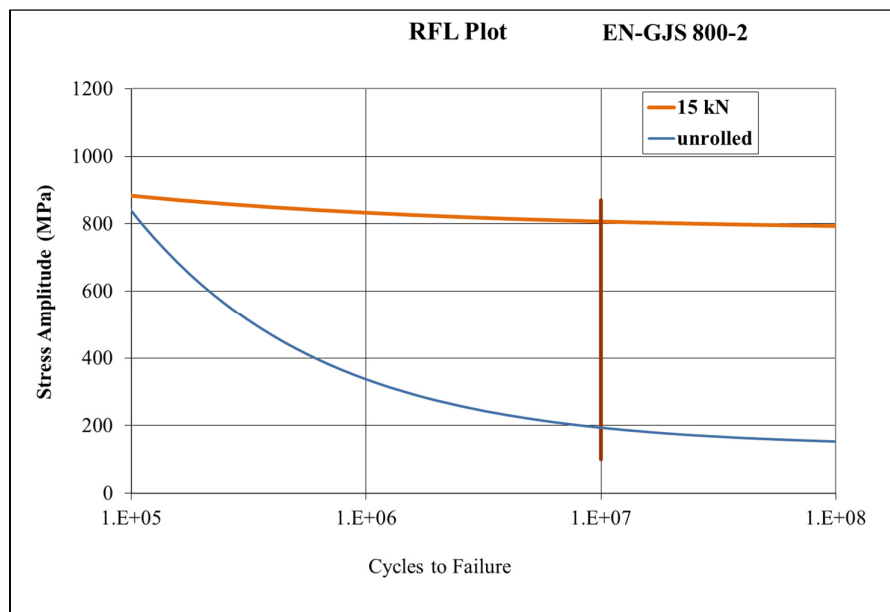


Figure 5.11 S-N curves of EN-GJS 800-2 crankshaft at unrolled condition and fillet rolled under 15kN rolling load.

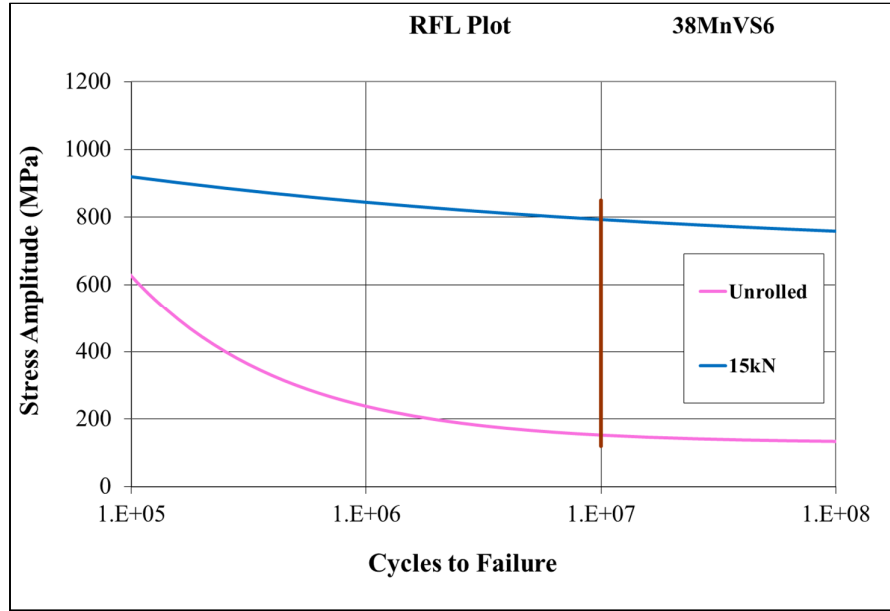


Figure 5.12 S-N curves 38MnVS6 steel crankshaft at unrolled condition and fillet rolled under 15kN rolling load.

5.2.2 Effect of Fillet Rolling Load on Fatigue Behavior of Steel Crankshafts

The median S-N curves of 38MnVS6 crankshafts at different rolling conditions were demonstrated on Figures 5.13 and 5.14. In Figure 5.14 the unrolled condition is excluded to differentiate the effect of rolling load in detail. Table 5.2 summarizes the measured fatigue strengths of each rolling condition and improvement factor calculated for each rolling load with respect to the unrolled condition. Effect of rolling load on fatigue strength was also demonstrated on Figure 5.15. As seen from these data, a significant improvement was obtained by the use of local fillet rolling process and an increase of fatigue strength is observed with the increasing rolling load up to 20kN. On the other hand, 24kN rolling load has resulted in a lower fatigue strength than the 20kN condition.

This result shows that the maximum rolling load that results in maximum achievable fatigue strength lies between 20kN and 24kN rolling load.

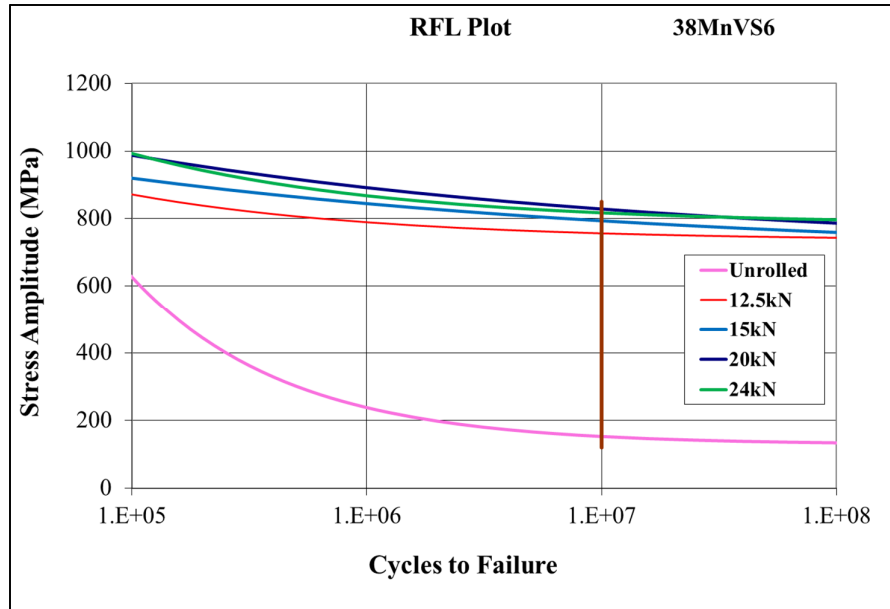


Figure 5.13 S-N curves of 38MnVS6 crankshafts at unrolled condition and fillet rolled under different rolling loads.

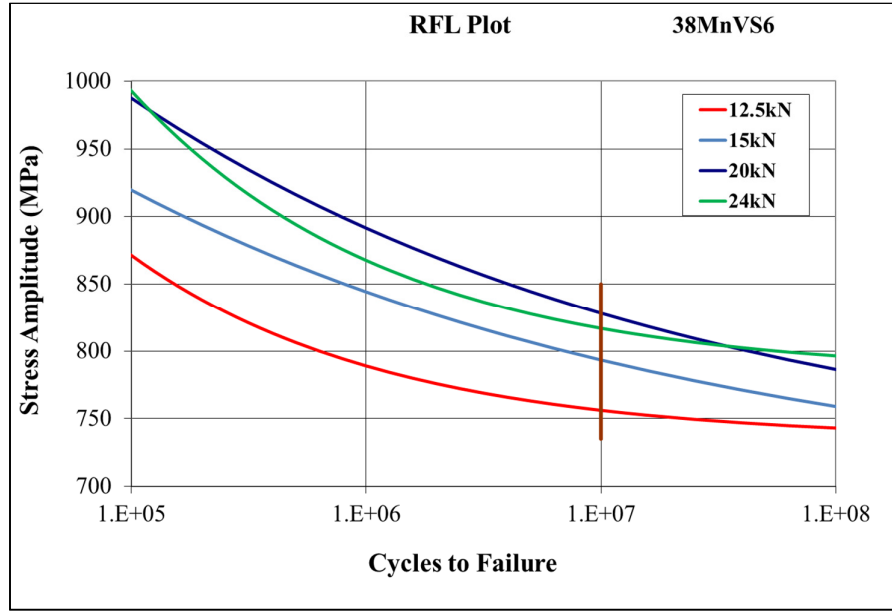


Figure 5.14 S-N curves of 38MnVS6 crankshafts fillet rolled under different rolling loads.

Table 5.2 Summary of fatigue strength data of 38MnVS6 crankshafts at unrolled condition and fillet rolled under different rolling loads.

Rolling Load (kN)	Median Fatigue Strength (MPa)	Improvement Factor
0	152.70	-
12.5	756.14	4.95
15	793.36	5.20
20	828.18	5.42
24	816.93	5.35

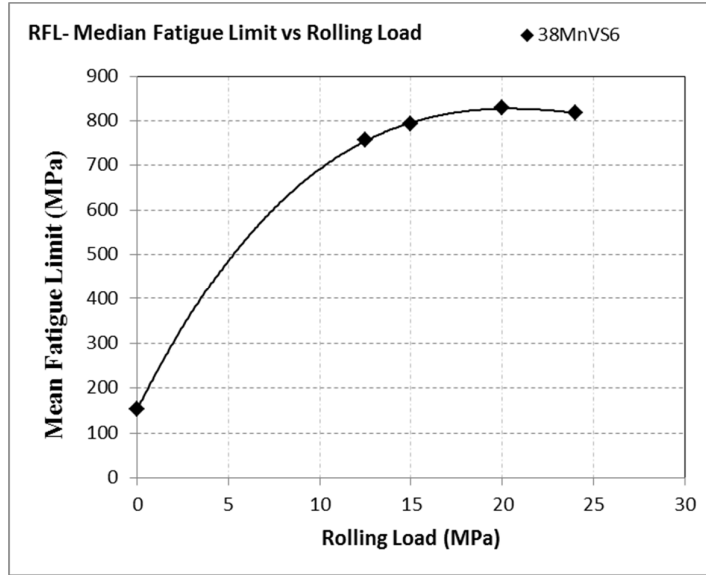


Figure 5.15 Fatigue strength versus rolling load for 38MnVS6 crankshafts.

5.3 Comparison of Deformation Characteristics of EN-GJS 800-2 and 38MnVS6 Materials under Fillet Rolling

As shown in Figures 3.17 to 3.23 in section 3.3.3.1, no apparent change in grain shape and no apparent change in grain thickness in the direction of rolling was observed in ductile cast iron crankshaft (Figures 3.17 and 3.18); while at the same rolling load, reduction in grain thickness in the direction of rolling and elongation in perpendicular direction can easily be differentiated on steel crankshafts (Figures 3.19 and 3.20).

As shown on Table 3.10 in section 3.3.3.2, at the same rolling conditions, an increase of 13.6% undercut depth and 4.0% increase in undercut radius were measured for ductile cast iron crankshaft while changes in the same parameters for steel crankshaft were measured as 27.0% and 6.1% respectively, indicating a higher amount of plastic deformation for steel crankshaft.

According to hardness measurement results summarized in section 3.3.3.3, on Tables 3.11 and 3.12, a hardness increase of 13% and 23% were observed for ductile cast iron and steel crankshafts at a depth of 0.75mm for the same fillet rolling conditions, which indicates a higher amount of strain hardening in steel crankshafts under the same rolling conditions.

The comparison of microstructural effects, undercut profile changes and hardness improvement values show that, as expected, the plastic deformation capability of the 38MnVS6 steel is higher than that of EN-GJS 800-2 ductile cast iron. These results also supports the fact that a higher fatigue strength improvement due to strain hardening is achieved with the steel crankshaft as explained in section 5.2.1.

5.4 Effect of Rolling Load on Deformation Characteristics of 38MnVS6 Steel

In section 3.3.3.1, on Figures 3.19 to 3.23 it was observed on optical micrographs that; increasing amount of applied fillet rolling load results in an increase in the amount of reduction in grain thickness in the direction of rolling and elongation of the grains perpendicular to the direction of rolling for 38MnVS6 steel crankshafts.

By using the data on Table 3.8, undercut depth and radius with respect to fillet rolling load for 38MnVS6 steel crankshafts were shown graphically on Figures 5.16 and 5.17. It can be derived from these figures that with the increasing rolling load, the severity of deformation at the undercut region increases. On the other hand, the rate of change in undercut depth and radius decreases towards the higher rolling loads and the dimensions are nearly stabilized at 24kN. A similar behavior was observed in hardness profile of the fillet region which is demonstrated graphically on Figure 5.18, by using the data on Table 3.12.

These results indicate that the maximum achievable deformation at the fillet region was obtained around 24kN rolling load for 38MnVS6 crankshaft. These results are also consistent with the fatigue strength increase behavior with the rolling load which was shown on Figure 5.15. It was also explained previously that the fatigue strength obtained with 24kN rolling load is lower than with 20kN. Thus, from these findings, it is derived that the workability limit of the material lies in between 20 and 24kN, possibly near to 24kN.

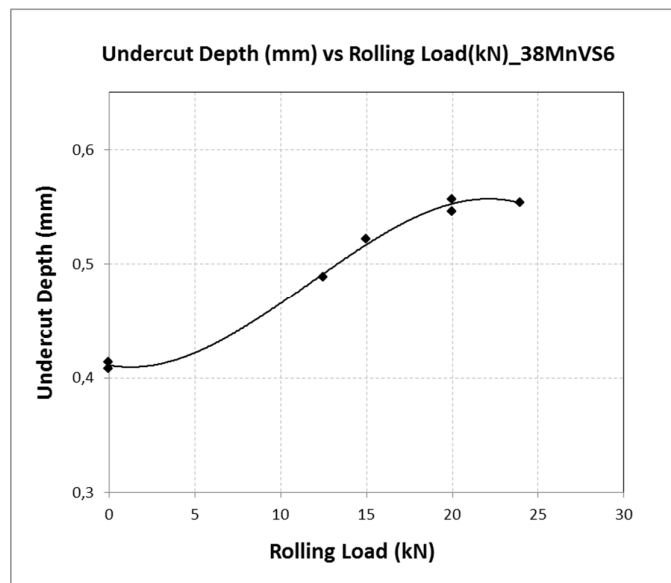


Figure 5.16 Undercut depth versus rolling load for 38MnVS6 crankshafts.

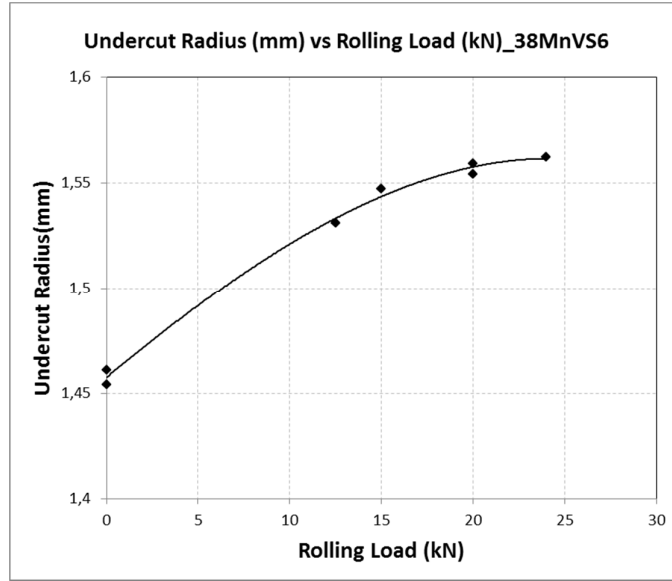


Figure 5.17 Undercut radius versus rolling load for 38MnVS6 crankshafts.

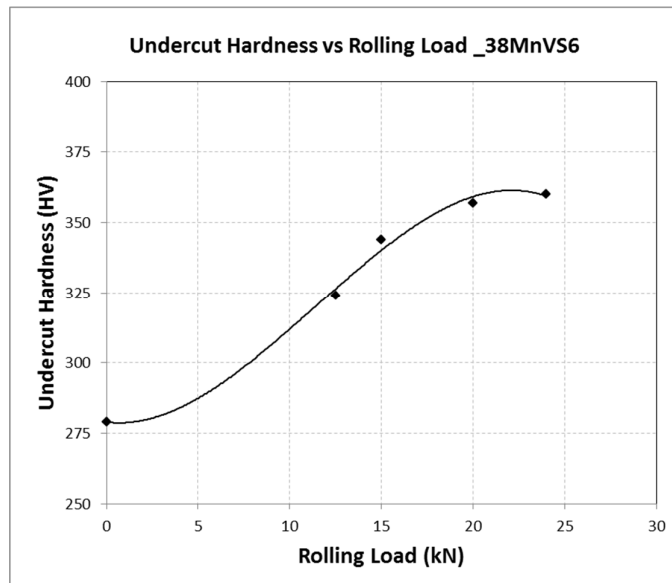


Figure 5.18 Undercut hardness versus rolling load for 38MnVS6 crankshafts.

Workability is defined as the extent to which a material can be deformed in a metalworking process without formation of crack [9]. In this specific metalworking process, fillet rolling, the workability limit of the part can be defined as the load at which surface micro-crack formation starts at the fillet region.

Figure 5.19 shows the fillet surfaces of 38MnVS6 crankshafts rolled at 24kN and 20kN. As seen, there is an obvious difference in surface qualities of the crankshafts. On the crankshaft where a rolling load of 24kN was applied, surface irregularities were observed which can act as crack initiation points and decrease the duration of fatigue crack initiation stage under cyclic loading. These finding explains the lower fatigue strength observed at 24kN rolling load condition with respect to 20kN.

Thus, it can be stated that the optimum rolling load for 38MnVS6 crankshaft with the studied design is between 20 and 24kN. Depending on the findings within the frame of this study, using a rolling load higher than 20kN is not recommended for this crankshaft and fillet design.

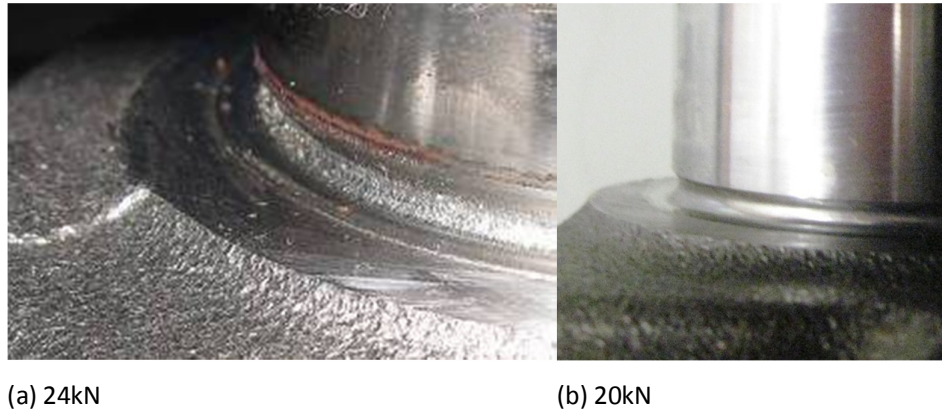


Figure 5.19 Fillet surface qualities of 38MnVS6 crankshafts at 24 and 20kN rolling conditions.

5.5 Discussions on the Mechanisms of Fatigue Strength Improvement by Fillet Rolling Process

In this part, the discussed findings within the frame of this project were explained based on the fundamental metallurgical rules to describe the effect of fillet rolling process on the fatigue performance of crankshafts.

As proved within this study, formation of compressive residual stresses is one of the major outcomes of the fillet rolling process. These compressive residual stresses can compensate the tensile components of the induced stresses during their service and hence improve the fatigue durability. In addition, since the peak residual stresses are induced at a certain depth from the surface, it can also decelerate or even stop the propagation of an initiated crack [61]. A Goodman type relationship of residual stress with fatigue strength is described as [71];

$$\sigma_a = \sigma_D - \frac{\sigma_D}{R_m} (\sigma_m + \sigma_R) \quad (5.1)$$

where σ_a is the fatigue strength with presence of residual stress, σ_D is the purely reversed tensile fatigue limit, σ_m is the mean fatigue stress, σ_R is the residual stress in the direction of applied stress and R_m is the tensile strength. The ratio σ_D/R_m is represented as α and called as endurance ratio, which decreases with increasing tensile strength [71]. From the above relationship, it should be noted that interference of residual stress with the applied stresses depend on the applied mean fatigue stress. Another fact to be taken into account is that an amount of residual stress relief will occur in the first cycles of applied tensile stresses.

The second major effect of fillet rolling process is the strain hardening which occurs by plastic deformation under the applied load. By plastic deformation, the dislocation density increases by dislocation multiplication and formation of

new dislocations. As a result of increased dislocation density, the average distance between dislocations decreases and due to higher dislocation-dislocation interactions, resistance to deformation increases. Thus, higher stresses are required for further deformation; which means that the hardness and strength of the material increases [1, 3, 9]. As a result of increased hardness due to the rolling process, larger stresses are required for crack initiation. Moreover, since plastic deformation is effective through the fillet depth up to at least 1.5mm, increased hardness can also retard the crack propagation step to larger number of cycles. Thus, by the described mechanisms, fillet rolling increases the fatigue strength as a result of strain hardening effect.

As definitely observed on 38MnVS6 steel crankshafts, the grain thickness in the direction of rolling was decreased with the increasing rolling load. By a decreased distance between the grain boundaries, a higher number of grain boundaries will be present at a certain length which act as barriers to both dislocation motion and crack propagation [1]. Decrease in the thickness of the grains, in the direction of rolling at the fillet region, can thus act as a strengthening mechanism against fatigue crack initiation and propagation specifically in the direction of rolling.

An additional positive effect of rolling process was described by Çevik et. al [61] as the increase of the surface quality by leveling the roughness peaks as a result of fillet rolling. On the other hand, in the frame of this work, it was observed that when the workability limit of the material is reached, surface quality decreases resulting in a decrease in fatigue strength. So it should be emphasized that the effect of fillet rolling process on surface quality depends on the applied rolling load.

Another mechanism of fatigue strength improvement by fillet rolling process can be defined as the decreased stress concentration due to the increased undercut radius. On the other hand, undercut depth which is also increased by

fillet rolling may increase the stress concentration. Thus, effect of undercut profile change on fatigue strength of the crankshaft will be a compromise between the effects of changes in undercut radius and depth.

CHAPTER 6

CONCLUSIONS

The following conclusions were drawn from the discussions of the data obtained within the frame of this work.

Ductile cast iron, EN-GJS 800-2, crankshaft showed superior fatigue performance to the micro-alloyed steel, 38MnVS6, crankshaft both at fillet rolled and unrolled conditions. On the other hand, fillet rolling process was found to be more effective on fatigue performance of steel crankshaft.

An increase in fatigue limit was observed with the increasing rolling load up to 20kN for the 38MnVS6 crankshaft. 24kN rolling load yielded in lower fatigue strength than 20kN condition for the steel crankshaft. Thus, the limiting fillet rolling load for fatigue strength improvement for 38MnVS6 crankshaft was stated to be within the range of 20kN to 24kN for this specific material and crankshaft design condition. Deformation characteristics at the fillet region with respect to rolling load and decreased surface quality at 24kN rolling load condition are consistent with this finding.

According to residual stress analysis by finite element method, a higher magnitude of peak residual stress at the fillet region was recorded for steel crankshaft than the ductile cast iron crankshaft at the same rolling condition. On the other hand, effective depth of compressive residual stress was found to be higher on ductile cast iron crankshaft.

Residual stress analysis of steel crankshafts show that; effect of increased rolling load on magnitude of peak residual stress is not significantly high, but the main effect of increased rolling load is the increased effective depth of residual stresses.

By the fatigue tests, compressive residual stress calculations; and the local material characterization at the fillet region, it was proven that the major strengthening mechanisms against fatigue by fillet rolling process are strain hardening and formation of compressive residual stresses.

As a result of using a relatively large frequency limit for the fatigue tests, on the order of 10% of the resonance frequencies, complete S-N curves covering crack initiation, propagation and final fracture stages were obtained.

Staircase test methodology has been found successful for accelerated fatigue testing of engineering components because of its conveniency to apply and valuable data it supplies for statistical analysis with small sample sizes.

The Maximum Likelihood Estimation methodology used in statistical analyses of the test data was found to be effective for life regression and fatigue strength distributions analysis. Random Fatigue Limit model has provided better curve fit capturing the curvature of S-N curve and more approximate fatigue limit calculations with higher likelihood values than Modified Basquin model. Dixon-Mood method was found to be overestimating the fatigue limit and thus is not recommended for fatigue limit calculations.

A new methodology was proposed within the frame of this study simulating the fillet rolling process three dimensionally with the actual rolling conditions. The proposed methodology has enabled to obtain the compressive residual stress profiles at the fillet region with effective resolutions and reliable values.

The proposed procedure for calculation of the maximum bending stresses at the fillet region, by the utilization of fatigue test rig simulation, was effectively used and enabled to construct the S-N curves.

Finally, it can be concluded that obtained results and findings; and developed methodologies within the frame of this work can form a baseline and useful database for crankshaft optimization studies, supplying a know-how on fillet rolling process, evaluation of its effect on fatigue performance and mechanisms leading to fatigue performance improvement.

REFERENCES

1. W.D. Callister, Jr, Materials Science and Engineering, Wiley International, 2003.
2. ASM Handbook, Fatigue and Fracture, Vol 19, ASM International, 1996.
3. R.W. Hertzberg, Deformation and Fracture Mechanics of Engineering Materials, John Wiley and Sons, 1996.
4. A. Wöhler, Versuche ur Ermittlung der auf die Eisenbahnwagen Achsen Einwirkenden Krafte und der Widerstandsfahitgkeit der Wagen Achsen Zeitschrift für Bauwesen Vol. 10, pp584-616,1860.
5. Y. Bai, Marine Structural Design, Elsevier Science Ltd., 2003.
6. D. J. Wulpi, Understanding How Components Fail, American Society for Metals, Materials Park, OH, 1985.
7. V. J. Colangelo and F. A. Heiser, Analysis of Metallurgical Failures, John Wiley & Sons, New York, 1987.
8. S. Suresh, Fatigue of Materials, Cambridge University Press, 1991.
9. G.E. Dieter, Mechanical Metallurgy, McGraw Hill, 1988.
10. D. Walton, and E.G. Ellison, "Fatigue Crack Propagation", ASTM Spec. Tech. Publ., Int. Metall. Rev., Vol 17. 1972, pp100-116.
11. P.C. Paris, F. Erdoğan, A Critical Analysis of Crack Propagation Laws, Journal of Basic Engineering, ASME Transactions, Vol. 85, No.4, p 528, 1963.
12. P. C. Paris, M.P. Gomez, and W.E. Anderson, A Rational Analytic Theory of Fatigue, The Trend in Engineering, Vol 13, No 9, pp 9-14, 1961.
13. H. L. Edwalds and R. J. H. Wanhill, "Fatigue Crack Growth", Fracture Mechanics, pp. 171, 1987.

14. A. Palmgren, "Durability of Ball Bearings", ZDVDI, Vol.68, No14, p.339, 1924.
15. M.A. Miner, "Cumulative Damage in Fatigue", Trans. ASME, J. Applied Mechanics, Vol 67, pA159, 1945.
16. J. Goodman, Mechanics Applied to Engineering, Longmans Green, London, 1899.
17. H. Gerber, Bestimmung der Zulassigen Spannungen in Eisenkonstruktionen. Zeitschrift des Bayerischen Architekten und Ingenieur-Vereins Vol.6, pp 101–10, 1874.
18. C.R. Soderberg, Factor of Safety and Working Stress, Transactions of ASME, Vol. 52, pp13–28, 1939.
19. R.I. Stephens, A. Fatemi, R.R. Stephens, H.O. Fuchs, Metal Fatigue in Engineering, John Wiley and Sons, 2001.
20. R.C. Juivanall and K.M. Marshek, Fundamentals of Machine Components Design, John Wiley and Sons, New York, 1991.
21. R.B. Heywood, Designing against Fatigue of Metals, Reinhold, New York, 1962.
22. W. Weibull, A Statistical Distribution Function of Wide Applicability, Journal of Applied Mechanics, Vol. 73, p293, 1951.
23. W. Weibull, Fatigue Testing and Analysis of Results, Pergamon Press, London, 1961.
24. H.S. Reemsynder, SAEFDE/The University of Iowa Short Course Notes on Fatigue Concepts in Design, 1999.
25. R.D. Pollack, Analysis of Methods for Determining High Cycle Fatigue Strength of a Material with Investigation of Ti-6Al-4V Gigacycle Fatigue Behavior, PhD Dissertation, Air Force Institute of Technology, 2005.
26. Little, R. E. and E. H. Jebe, Statistical Design of Fatigue Experiments, John Wiley & Sons, 1975.
27. J.W. Harris and H. Stocker, Handbook of Mathematics and Computational Science, Springer-Verlag, 1998.
28. Annis, Charles., www.statisticalengineering.com (website), 2012.

29. C. Engler-Pinto Jr., J. V. Lasecki, R. J. Frisch Sr., M. A. De Jack and J. E. Allison, 2005 SAE World Congress, Detroit, Michigan, April 11-14, 2005.
30. Sinclair, G. M. and T. J. Dolan, Effect of Stress Amplitude on Statistical Variability in Fatigue Life of 75S-T6 Aluminum Alloy, Transactions of the American Society of Mechanical Engineers, Vol.75, pp 867-872, 1953.
31. D. J. Finney, Probit Analysis, 3rd Ed., Cambridge University Press, 1971.
32. R. E. Little, Estimating the Median Fatigue Limit for Very Small Up-and-Down Quantal Response Tests and for S-N Data with Runouts, Probabilistic Aspects of Fatigue, American Society for Testing and Materials, STP 511, 1972.
33. M. Prot, Un Nouveau Type de Machine D'Essai des Metaux a la Fatigue par Flexion Rotative, Rev. Metall., Vol. 34, p 440, 1937.
34. R. E. Little, Manual on Statistical Planning and Analysis, American Society for Testing and Testing and Materials, STP 588, 1975.
35. W. J. Dixon, The Up-and-Down Method for Small Samples, Journal of the American Statistical Association, Vol. 60, pp 967-978, 1965.
36. W. J. Dixon and A. M. Mood, A Method for Obtaining and Analyzing Sensitivity Data, Journal of the American Statistical Association, Vol. 43, pp 109-126, 1948.
37. E. J. Ward, R. T. Schwartz, and D. C. Schwartz. An Investigation of the Prot Accelerated Fatigue Test, Proceedings of the American Society for Testing and Materials, Vol. 53, pp 885-891, 1953.
38. J. E. Spindel, and E. Haibach, Some Considerations in the Statistical Determination of the Shape of S-N Curves, Statistical Analysis of Fatigue Data, American Society for Testing and Materials, STP 744, 1981.
39. F.G. Pascual, and W.Q. Meeker, Analysis of Fatigue Data with Runouts Based on a Model with Nonconstant Standard Deviation and a Fatigue

- Limit Parameter, Journal of Testing and Evaluation, Vol. 25, pp 292-301, 1997.
40. F.G. Pascual, and W.Q. Meeker, Estimating Fatigue Curves with the Random Fatigue-Limit Model, Technometrics, Vol. 41, pp 277-289, Nov 1999.
 41. C. Bathias, and J. Ni, Determination of Fatigue Limit Between 105 and 109 Cycles Using an Ultrasonic Fatigue Device, Advances in Fatigue Lifetime Predictive Technique: Second Volume, American Society for Testing and Materials, STP 1211, 1993.
 42. C. Annis, Discussion – Estimating Fatigues Curves with the Random Fatigue-Limit Model, Technometrics, Vol. 41, pp 292-293, 1999.
 43. J.T. Ransom, and R.F. Mehl, The Statistical Nature of the Endurance Limit, Metals Trans, Vol. 185, pp. 364–365, 1949.
 44. W.Q. Meeker, and L. A. Escobar, Statistical Methods for Reliability Data, John Wiley & Sons, 1998.
 45. Verlag Modern Industrie, “Motor Vehicle Crankshafts”, Krupp Gerlach, 2001.
 46. T. K. Garret, K. Newton, W. Steeds, The Motor Vehicle, Butterworth-Heinemann, 2001.
 47. M. Zoroufi and A. Fatemi, A Literature Review on Durability Evaluation of Crankshafts Including Comparisons of Competing Manufacturing Processes and Cost Analysis, 26th Forging Industry Technical Conference, Chicago, IL, November 2005.
 48. F.H. Montazersadgh and A. Fatemi, Stress Analysis and Optimization of Crankshafts Subject to Dynamic Loading, A Final Project Report Submitted to the Forging Industry Educational Research Foundation and American Iron and Steel Institute , The University of Toledo, 2007
 49. M. C. Cevik, An Efficient Methodology for Borderline Design of Crankshafts, Dissertation, RWTH Aachen, 2011.
 50. Y.S. Ko, J.W. Park, H.O. Bhan, H. Park, and J.D. Lim, Fatigue Strength and Residual Stress Analysis of Deep Rolled Crankshafts, 2005 SAE

World Congress, Detroit, Michigan, United States, 2005-01-0988, 2005.

51. G. Cevik, Z. Tuncali, E.T. Duran, A Study on the Diesel Engine Crankshaft Fatigue Performance Optimization, 2009 SAE World Congress, Detroit, Michigan, United States, 2009-01-0261, 2009.
52. M.N. Regul'skii, A.D. Pogrebnyak and O.B. Balakowski, Procedure and Results of Investigation into Fatigue Strength Characteristics of Motorcycle Engine Crankshafts, *Strength of Materials*, Vol. 34(6), 2002.
53. M. Feng, M. Li, Development of a Computerized Electrodynamic Resonant Fatigue Test Machine and Its Applications to Automotive Components. SAE Technical Paper 2003-01-0951, 2003.
54. T. Watmough, M.J. Malatesta, Strengthening of Ductile Iron for Crankshaft Applications, *Proceedings of Expendable Pattern Casting: Managing the Technology*, AFS; p 83–99, 1993.
55. V. Yu, W.Y. Chien, K. Choi, J. Pan and D. Close, Testing and Modeling of Resonant Shifts in Resonance Bending Fatigue Tests of Notched Crankshaft Sections. SAE Technical Paper, 2004-01-1501, 2004
56. R.J. Love, and D.N. Waistall, The Improvement in the Bending Fatigue Strength of Production Crankshafts by Cold Rolling, M.I.R.A., Report No. 1954/1, pp 1-8, 1954.
57. W.Y. Chien, J.Pan, D. Close, S. Ho, Crankshaft Fatigue Crack Propagation Analysis with Consideration of Residual Stresses, *International Journal of Fatigue*, Vol. 27, 1–19, 2005.
58. P. Spiteri, S. Ho, Y.L. Lee, Assessment of Bending Fatigue Limit for Crankshaft Sections with Inclusion of Residual Stresses, *International Journal of Fatigue*, Vol. 29, p 318–329, 2007.
59. K.S. Choi, J. Pan, Simulations of Stress Distributions in Crankshaft Sections Under Fillet Rolling and Bending Fatigue Tests, *International Journal of Fatigue*, Vol. 31, pp 544-557, 2009.

60. K.S. Choi, J. Pan, A Generalized Anisotropic Hardening Rule Based on the Mroz Multi-Yield-Surface Model for Pressure Insensitive and Sensitive Materials, *International Journal of Plasticity*, Vol. 25(7), pp 1325-1358, 2009.
61. M.C. Cevik, H. Hochbein, M. Rebbert, Potentials of Crankshaft Rolling Process, SAE International, 2012-01-0755, 2012.
62. Spheroidal Graphite Cast Irons, EN 1563: 1997-A1: 2002, p 20, 2003.
63. Standard Test Methods for Tension Testing of Metallic Materials, ASTM E8/E8M-09, 2009.
64. Standard Test Methods for Brinell Hardness of Metallic Materials, ASTM E10-10, 2010.
65. X. Zhou, X. Yu, Fatigue Crack Growth Rate Testing Using a Frequency Sweep Method, *Journal of Zhejiang University, Science A*, Volume 9 (3), pp 346-350, 2008.
66. J.P. Den Hartog, *Strength of Materials*, Mc Graw Hill, 1977.
67. Calculation of Crankshafts for Diesel Engines, Det Norkse Veritas, Norway, 2002.
68. S. Ho, Y.L. Lee, H.T., Kang, C.J. Wang, Optimization of Crankshaft Rolling Process for Durability, *International Journal of Fatigue*, Vol 31, pp 799-808, 2009.
69. Internal Standard, WSS-M1A340-A1/A2/A3, Ford Motor Company, 1999.
70. Yen, C. S., Dolan, D. J, A Critical Review of the Criteria for Notch-Sensitivity in Fatigue of Materials, *University of Illinois Bulletin*, V49, No.53, Illinois, 1952.
71. Handbook of Residual Stress and Deformation of Steel, ASM International, 2002.

CURRICULUM VITAE

PERSONAL INFORMATION

Name: Gül Çevik
Date and Place of Birth: 18.01.1979, Ankara
Place of Birth: Ankara
Marital Status: Single
Nationality: T.C.

EDUCATION

2012: Ph.D - Metallurgical and Materials Engineering, Middle East Technical University, Ankara, Türkiye

2004: M.Sc. - Metallurgical and Materials Engineering, Middle East Technical University, Ankara, Türkiye

2001: B.Sc. - Metallurgical and Materials Engineering, Middle East Technical University, Ankara, Türkiye

1997: Ankara Atatürk Anatolian High School, Ankara, Türkiye

WORK EXPERIENCE

March 2007 – (Present): Product Development and Design Engineer - Ford Otomotiv Sanayi A.Ş., Kocaeli, Türkiye

December 2001 – March 2007: Research Assistant - Department of Metallurgical and Materials Engineering, Middle East Technical University, Ankara, Türkiye

LANGUAGE SKILLS

Advanced English, Basic German, Basic Russian

PUBLICATIONS

- 1) “Evaluation of Fatigue Performance of a Fillet Rolled Diesel Engine Crankshaft”, Gül Çevik, Rıza Gürbüz, Engineering Failure Analysis, Available online, 6 September 2012.
- 2) “A Study on the Diesel Engine Crankshaft Fatigue Performance Optimization”, SAE Paper, International Conference, 2009-01-0261, Gül Çevik, Zafer Tuncalı, Tolga Duran, 2009.
- 3) “Study on the Stress Corrosion Cracking Behavior of 7050-T73651 Aluminum Alloy in Three Different Orientations”, Gül Çevik, Mustafa Doruk, Rıza Gürbüz, 7. International Fracture Conference, Kocaeli, 2005.
- 4) “Effect of Heat Treatment on the Stress Corrosion Cracking Susceptibility of 7050 Aluminum Alloy”, Gül Çevik, Mustafa Doruk, Rıza Gürbüz, 12. International Metallurgical and Materials Conference, İstanbul, 2005.
- 5) “Investigation of the Effect of Orientation and Heat Treatment on the Stress Corrosion Cracking Susceptibility of 7050 Aluminum Alloy”, Gül Çevik, M.Sc. Thesis, Middle East Technical University, Ankara, 2004.